Modelling of Compressional Alfvén Eigenmodes in Axisymmetric Toroidal Fusion Plasmas

by

Jack Callum Bradshaw

Submitted to the University of Warwick

for the degree of

Doctor of Philosophy

Department of Physics

December 2020

Contents

List of Figures

Acknowledgement

I would first like to thank my supervisor, Dr Erwin Verwichte, without whom this work would not have been possible. It was your initial project idea that I took and worked on, and without your patient guidance, insight, and reassurance, I do not know whether I would have made it to the end. The "motivation curve" that you drew at the start of the project was invariably correct and was a useful reminder, in my low moments, that things would pick up again. I also very much enjoyed our discussions about teaching, which I will bear in mind as I start out my career as a professional teacher.

I would also like to thank my fiancée Simran whom I met at the start of this postdoctoral journey. You have broadened my horizons whilst at the same time grounding me and helping me stay sane during intense periods of working, the isolation of COVID-19, and everything else that has been challenging in the past 5 years. Thank you darling for putting up with my hectic work schedule. I'm very much looking forward to our life together.

I am grateful to my family who emphasised to me, throughout my life, the value of education not as a means to an end but as an end in itself. They were always there for me whenever I needed them. Thank you Mum for speaking frankly when required but always with my best interest at heart. Thank you Dad for successfully distracting me whenever I felt stressed out. Thank you Sam for being understanding in a way that others sometimes weren't, as you were engaged in your own similar endeavour. A hearty thanks also to Rob and my grandparents.

To all the friends and colleagues I have met along the way, particularly those who I had the joy of sharing an office with at any point, it's been a pleasure.

Thanks SJ for being a good emotional support when I was feeling overwhelmed, and for bearing the brunt of my mostly frivolous questions. And thanks Sanket, my conference buddy - I very much enjoyed learning from you with every conversation we had.

I would also like to add a special thanks to Dr Simon Carson for showing me that physics can be far more interesting than the UK school curriculum would have you believe.

Declarations

The work presented in this thesis is that of the author, except where stated otherwise, and was carried out at the University of Warwick under the supervision of Dr Erwin Verwichte. This work has not been submitted for any other degree.

Abstract

Compressional Alfvén eigenmodes (CAEs) have been linked to electromagnetic emission detected in tokamaks in the frequency range around harmonics of the ion cyclotron frequency, and more recently to sub-ion cyclotron frequency emission in spherical tokamak experiments. This has sparked interest in using CAEs as a diagnostic for fast-ion distributions in fusion devices. This thesis presents a linear stability code, Whales2, that solves for CAEs using the linearised cold ideal Hall-MHD equations. Whales2 is a mixed finite elements spectral code that operates in a 2-dimensional axisymmetric toroidal geometry to solve for the frequency and spatial structure of CAEs in a given ideal-MHD equilibrium.

In this thesis we present how the Whales2 code is designed to calculate CAEs whilst avoiding the physical coupling of CAEs to the slow-magnetoacoustic and shear Alfvén eigenmodes. We demonstrate that Whales2 is free from spectral pollution and that the self-adjointness of the ideal-MHD equations is preserved in the numerical methods employed by Whales2. We show that Whales2 well reproduces analytical and qualitative predictions of CAE theory in a range of test cases in cylindrical and toroidal geometries. We also use output from Whales2 to establish the behaviour of CAEs with respect to including the Hall term in the MHD equations, particularly in the lifting of the positive/negative frequency degeneracy that is present in ideal-MHD. Results from Whales2 show the impact that the Hall term can have on the spatial localisation of CAEs. Whales2 manipulates the MHD equations based on the method detailed in [3] to avoid CAE coupling to the shear Alfvén continuum - the effectiveness of this method is demonstrated clearly for the first time, to the author's knowledge.

Chapter 1

Introduction

1.1 Fusion Power Overview

Nuclear fusion refers to the fusing of two atomic nuclei into a single larger nucleus whilst nuclear fission is the opposite process of a large nucleus dividing into smaller nuclei. The idea of harnessing these nuclear processes to produce energy in laboratories manifested in the first half of the 20th century when nuclear physics was being explored. Nuclear reactions produce significantly more energy per unit of fuel than their chemical counterparts, making research into commercial nuclear power plants attractive. The first fission reactors started supplying electricity commercially in the 1950s and since then nuclear fission has become an integral part of the energy landscape. Nuclear fusion is still yet to be realised as a means of commercial electricity production due to its many complexities. Interest in nuclear fusion has been growing at least in part due to an increasing awareness of the contribution of fossil fuel burning energy sources to the global greenhouse effect and the benefits and feasibility of fusion power have been widely analysed [1, 4–7].

The energy released in nuclear reactions, both fission and fusion, comes from the difference in the summed binding energies of the reactant particles against the sum of the products' binding energies. The binding energy is, roughly, the work required to separate all of the protons and neutrons from the particle nucleus to the point at which they are no longer held together. Fig. 1.1 shows the binding energies (per nucleon) against nucleon number for isotopes of each element, revealing that the most stable elements are those with isotopes comprised of about 56 nucleons (particularly Fe^{56}). There are clearly two routes to exploiting this difference in binding energies to extract energy: fission primarily exploits the 'right hand side' of Fig. 1.1 whereas fusion predominately outputs energy when fusing the lowest

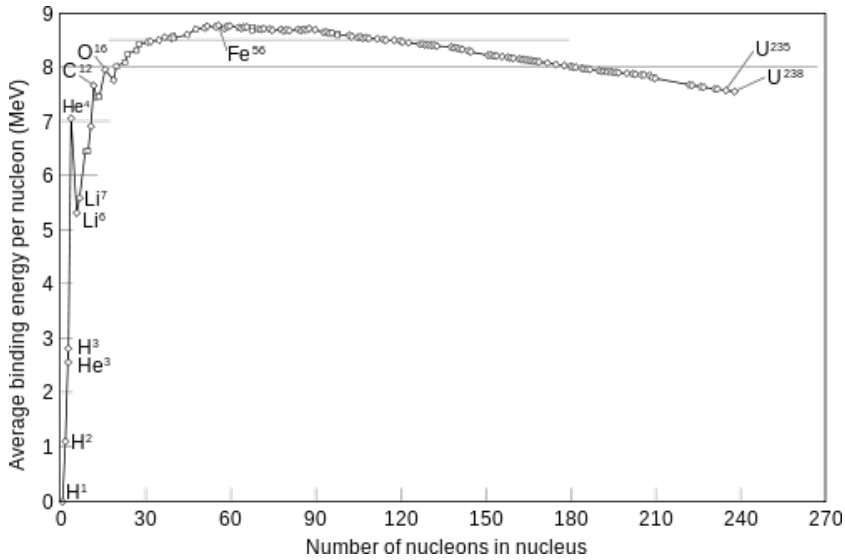

Figure 1.1: Diagram showing binding energy per nucleon for each element against their nucleon number. Image courtesy of *Wikimedia Commons*.

nucleon number elements.

Nuclear fusion occurs when two atomic nuclei collide with sufficient energy to overcome their mutual coulombic repulsion, the so-called *coulombic barrier*, so that the strong force can act to bind the nuclei together. Classically this gives a high minimum energy requirement for a successful fusion collision. However, quantum tunneling allows particles to 'tunnel' through the potential barrier, thus giving a non-zero fusion probability for particle collisions at lower energies. The probability of a collision leading to a fusion reaction is expressed through the cross-section σ, which is a function of particle velocities at the point of collision. Temperature in fusion literature is often given in units of energy (usually keV) using the conversion $E = k_B T$ so that 1 eV = 11605 K . There are many different fusion reactions to be considered but most of them require too high a temperature or density to be considered worthwhile. The most feasibly achievable reactions in a lab are given below:

$$ {}^{2}_{1}D \; + \; {}^{3}_{1}T \; \rightarrow \; {}^{4}_{2}He \; + \; {}^{1}_{0}n \; + \; 17.6 \text{ MeV} \; , \tag{1.1} $$

$$ {}^{2}_{1}D \; + \; {}^{2}_{1}D \; \rightarrow \; {}^{3}_{2}He \; + \; {}^{1}_{0}n \; + \; 3.27 \text{ MeV} \; , \tag{1.2} $$

$$ {}^{2}_{1}D \; + \; {}^{2}_{1}D \; \rightarrow \; {}^{3}_{1}T \; + \; {}^{1}_{1}H \; + \; 4.03 \text{ MeV} \; , \tag{1.3} $$

$$ {}^{2}_{1}D \; + \; {}^{3}_{2}He \; \rightarrow \; {}^{4}_{2}He \; + \; {}^{1}_{1}H \; + \; 18.3 \text{ MeV} \; , \tag{1.4} $$

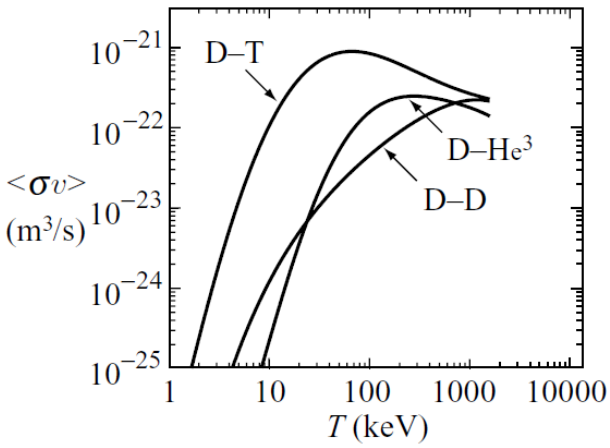

Figure 1.2: A plot of the velocity averaged cross-section for the D-T, D-D and D-He reactions. This clearly indicates that D-T reactions have the highest cross-section peak at the lowest temperatures and so is therefore the most feasible fusion reaction. Image reproduced from [1].

and a plot of their velocity averaged (over a Maxwellian distribution at given temperature) cross-sections against temperature is given in Fig. 1.2. It is desirable for a reaction to have a large cross-section at low temperatures and a large energy output. Of the four reactions (1.1)-(1.4) the D-T reaction, Eq. (1.1), best satisfies these requirements.

The basic power balance for a fusion reactor was calculated by J.D. Lawson in 1957 [8]. There are two major milestones by which to measure the power output of successive fusion reactor designs: *breakeven* and *ignition*. Breakeven is defined as the point at which the total heating power is equal to the power output from the fusion reactions when the reactor is operating at steady-state (i.e. the total heating power balances the power losses). Ignition is a more stringent condition that is achieved when the reactor is operating at steady-state but there is no external heating, so the plasma is being heated purely by the fusion reactions. Considering the case of a plasma consisting of a 50-50 (by number density) mixture of deuterium and tritium in a fusion device then Eq. (1) of [8] tells us that the total fusion power per unit volume is:

$$P_{\text{fus}} = \frac{1}{4} n^2 < \sigma v > \mathcal{E} \ , \tag{1.5}$$

where n is the total ion number density, $< \sigma v >$ is the velocity averaged cross-section and $\mathcal{E}$ is the energy output from each reaction. In the D-T reaction the produced neutrons gain $\sim 80\%$ of the kinetic energy output in each reaction and the α-particles only $\sim 20\%$. If we assume that the α-particles can redistribute their

energy perfectly back to the reactants then this is a source of internal heating for the plasma. The neutrons, however, have a mean-free-path that is much larger than any practical reactor design and so these cannot be considered in plasma heating. Following in the style of [9] we can write the power balance:

$$P_{\mathrm{H}} \; + \; \frac{1}{4} n^2 < \sigma v > \mathcal{E}_\alpha \; = \; \frac{3nT}{\tau_{\mathrm{E}}} \; , \tag{1.6}$$

where P_H is the externally applied heating power (per unit volume), $\mathcal{E}_\alpha = \frac{\mathcal{E}}{5}$ is the energy per reaction carried by the α-particles and the right hand side represents the power loss from the reactor where τ_{E} is defined as the *energy confinement time* - the characteristic timescale of energy loss from the reactor.

For breakeven the LHS of Eq. (1.9) is equal to the fusion power given in Eq. (1.5). Therefore can be written as a condition on the number density and energy confinement time:

$$n\tau_{\mathrm{E}} > \frac{12T}{< \sigma v > \mathcal{E}} \; . \tag{1.7}$$

In the temperature range of interest for fusion reactors of $10-20$ keV then $< \sigma v > \approx 1.1 \times 10^{-24} \mathrm{T}^2 \; \mathrm{m}^3\mathrm{s}^{-1}$ with T in keV [9]. The output energy from a single reaction is $\mathcal{E} = 17.6$ MeV so then breakeven is written as a condition on the triple product:

$$nT\tau_E > 6.2 \times 10^{20} \; \mathrm{m}^{-3}\mathrm{keVs} \; . \tag{1.8}$$

The analysis proceeds similarly for the ignition case. Without an external heat source ($P_H = 0$) the condition becomes:

$$nT\tau_E > 3.1 \times 10^{21} \; \mathrm{m}^{-3}\mathrm{keVs} \; . \tag{1.9}$$

There are a few potential routes to fusion energy though most can be broadly categorised into one of two philosophies. Magnetic confinement fusion (MCF) aims to confine the charged particles via a strong magnetic field and therefore increase the energy confinement time. Inertial confinement fusion (ICF) is based around increasing the achievable plasma density. These are broad descriptions and both branches have a plethora of ways to achieve the goal of net fusion energy output. Within this thesis we will be concentrating on a particular MCF approach that uses a confinement device called a Tokamak [1, 5, 9].

1.2 Tokamak Design

Some of the earliest approaches to MCF were based on the concept of a plasma pinch. In a pinch a large directional current induces a strong magnetic field that compresses the conducting material [10]. The earliest pinch reactor designs came from the so-called θ-pinch and Z-pinch, where the prefix refers to the direction of the current in a conducting cylinder. Each of these suffers from a particular drawback. The θ-pinch suffers from end losses with particles streaming out of the cylinder caps. Some manipulation of the magnetic fields may be used to try and mitigate this, as in a magnetic mirror device, but ultimately the end losses are too great. The Z-pinch suffers from disruptive instabilities (collective motion that pushes the plasma away from an equilibrium state), particularly the kink instability, that lead to loss of equilibrium and loss of plasma to the device wall. The screw-pinch is a hybrid of these concepts that allows for a helical current and therefore a helical magnetic field. This stabilises the Z-pinch. End losses can then be eliminated by connecting the screw-pinch ends into a torus thereby creating the Tokamak concept.

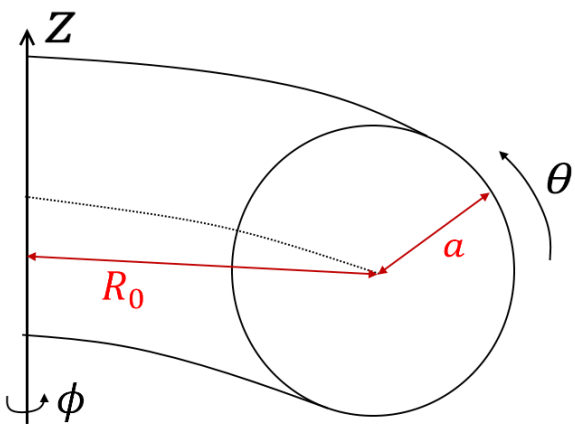

Figure 1.3: A sketch to illustrate the main sizes in a torus, and the directions of increasing poloidal, θ, and toroidal, ϕ, angle.

The main features of a tokamak geometry can be characterised by a few parameters. The *major radius*, R_0, is defined as the distance from the Z-axis to the toroidal axis. The *minor radius*, a, is the distance from the geometric centre of the plasma to the outer wall. The plasma cross-section is usually highly shaped but its

main characteristics are described by the following parameters:

$$\epsilon = \frac{a}{R_0} \quad \text{- inverse aspect ratio,} \tag{1.10}$$

$$\kappa = \frac{Z_{max}}{a} \quad \text{- elongation or ellipticity,} \tag{1.11}$$

$$\tau = \frac{R_{max} - R_0}{a} \quad \text{- triangularity,} \tag{1.12}$$

where R_{max} is the value of the major radius at the point of maximum height of the plasma, Z_{max}. We refer here only to up-down symmetric plasma equilibria. For the avoidance of any ambiguity, we follow the definitions for each quantity (and the extension to asymmetric plasma shapes) given by Luce [11]. The angular directions of a tokamak are defined with the poloidal, θ, direction going the "short way around" and toroidal, ϕ, the "long way around" - see Fig. 1.3.

The primary magnetic field in a tokamak is toroidal, generated by using poloidally shaped rings through which current is passed. A poloidal field can then be generated by using the plasma itself as a secondary transformer winding. A current is passed through a core on the tokamak central axis which induces a toroidal current in the plasma, thereby creating a poloidal field. Poloidal field coils (toroidally shaped rings) may also be used for additional plasma shaping. The plasma shape can be described by *magnetic flux surfaces* - surfaces through which there is no magnetic flux at any point. These surfaces typically form a set of closed, nested surfaces concentric on the magnetic axis, though there may be magnetic islands and reconnection points. In particular, most tokamaks now employ plasma shaping in order to form an X-point so that plasma material can be directed towards the *divertor* which is specially designed to handle a high heat flux. The boundary between the open and closed magnetic field regions is called the *last closed flux surface* (LCFS) or the *separatrix* [9].

Magnetic flux surfaces and the poloidal flux function, ψ, will be covered in Section 1.5. However, for now it is sufficient to say that ψ can be used as a proxy radial co-ordinate and so we use the co-ordinate convention (ψ, ϕ, ϑ) which produces a right-handed co-ordinate system consistent with Fig. 1.3. ϕ is the ignorable toroidal co-ordinate. We use the notation ϑ when referring to a general poloidal angle and θ to specifically refer to the circular polar angle.

Tokamaks that have an aspect ratio of around $R_0/a > 2$ (the definition is not precise) are considered to be *conventional tokamaks*. There are many conventional tokamak experiments currently in existence with the largest conventional tokamak to date, ITER, currently under construction. The main goals of ITER are to test the

components required for a future fusion reactor and to demonstrate a long duration steady state plasma burn with a high ratio of output to input power [12]. The current record for this ratio, denoted Q, was made in 1997 in JET (Joint European Torus) with $Q \simeq 0.67$ [13]. Breakeven occurs at $Q = 1$ and ITER is designed to exceed this by several times, and is hoped to reach ignition [12]. ITER is designed as a D-shaped plasma, with the following basic shape parameters [14]:

$$a = 2.0m \ , \tag{1.13}$$

$$R_0 = 6.2m \ , \tag{1.14}$$

$$\kappa_{95} = 1.70 \ , \tag{1.15}$$

$$\tau_{95} = 0.33 \ , \tag{1.16}$$

where the subscript indicates values that are applicable at 95% of the distance to the outer surface from the magnetic axis.

Another class of tokamak is categorised as having an aspect ratio of around $R_0/a < 2$. These are called *spherical tokamaks* (ST). The main advantage of an ST over a conventional tokamak is that the compact design allows for greater values of a quantity called the plasma-β [1]. Plasma-β is a ratio of the kinetic pressure in the plasma to the magnetic pressure:

$$\beta = \frac{2\mu_0 p}{B^2} \ . \tag{1.17}$$

However, the higher plasma-β values does not usually imply a higher kinetic pressure value but instead a lower magnetic field value for a given kinetic pressure when compared to a conventional tokamak. A particular example of the ST design is MAST-U (Mega-Ampère Spherical Tokamak - Upgrade) that has the following shaping parameters [15]:

$$a = 0.65m \ , \tag{1.18}$$

$$R_0 = 0.85m \ , \tag{1.19}$$

$$\kappa = 2.50 \ , \tag{1.20}$$

$$\tau = 0.3 - 0.8 \ , \tag{1.21}$$

1.3 Basic Plasma Physics

At temperatures where it can efficiently fuse, the D-T fuel will be a plasma. Colloquially a plasma is often described as an ionised gas but this does not capture

the full range of behaviour that a true plasma exhibits. Chen [5] gives a qualitative definition: "A plasma is a quasineutral gas of charged and neutral particles which exhibits collective behavior". Friedberg also states that a plasma should have "very high electrical conductivity" [1]. In a quantitative sense there are three conditions that a plasma should satisfy, out of which the above properties will follow. We need to define three quantities, the *Debye length* (λ_{D}), *Debye sphere* (Λ_{D}) and *plasma frequency* (ω_{p}), to show this.

The Debye length is essentially a measure of the plasma conductivity - it defines the characteristic lengthscale over which a DC electric field would be shielded by the plasma. It is given by the expression [16]:

$$\lambda_D = \left(\frac{\epsilon_0 T}{e^2 n}\right)^{\frac{1}{2}} , \tag{1.22}$$

for a single fluid plasma. When considering a two-fluid plasma one can define a Debye length for both the positively and negatively charged fluids. If the Debye length is small compared to the overall plasma size this implies high electrical conductivity - DC electric fields will be effectively shielded.

The Debye sphere is a measure of the number of particles within a volume element of side length λ_D (we could use a sphere but the numerical factor is irrelevant):

$$\Lambda_D = n\lambda_D^3 = \frac{\epsilon_0^{\frac{3}{2}} T^{\frac{3}{2}}}{e^3 n^{\frac{1}{2}}} . \tag{1.23}$$

This is a measure of the strength of the long-range collective behaviour of the particles against the short-range collisional behaviour. We know that electric fields are shielded over a distance of the Debye radius and so a more densely populated Debye sphere implies that more particles feel the electromagnetic effects of a given particle in the sphere, therefore a larger Debye sphere implies stronger collective behaviour [16]. Thus a plasma should have a Debye sphere such that $\Lambda_D \gg 1$.

We also consider the shielding of AC electric fields. An oscillating electric field causes the charged particles to accelerate back and forth in order to try to cancel out the field. For the fusion plasmas that we are considering, the positive ion species (hydrogen or similar) is much more massive than the negative ions (electrons), so the electrons will have a much more rapid response to any applied AC electric field. Therefore, the plasma frequency is equivalent to the electron frequency, defined by the maximum frequency of AC field that the electrons in the plasma can shield. This is given by [16]:

$$\omega_p \equiv \omega_{pe} = \left(\frac{e^2 n}{\epsilon_0 m_e}\right)^{\frac{1}{2}} . \tag{1.24}$$

So, for example, any EM wave that oscillates above this frequency will be able to freely travel in the plasma but below this frequency and it will be attenuated. These reactive motions should be much faster than the thermal motions of the particles in order to provide effective AC shielding.

Now we can write the three quantitative conditions as follows:

$$\lambda_D \ll L \ , \tag{1.25}$$

$$\Lambda_D \gg 1 \ , \tag{1.26}$$

$$\omega_{pe} \gg \frac{v_{Te}}{L} \ , \tag{1.27}$$

where L is the macroscopic size of the plasma.

A typical plasma in a tokamak will have values of temperature and number density on the order of $T \sim 10\text{keV}$ and $n \sim 10^{20}\text{m}^{-3}$. This gives the following values for the key plasma parameters:

$$\lambda_D \simeq 7.4 \times 10^{-5}\,\text{m} \ , \tag{1.28}$$

$$\Lambda_D \simeq 4.1 \times 10^{7} \ , \tag{1.29}$$

$$\omega_{pe} \simeq 5.6 \times 10^{11}\,\text{s}^{-1} \ , \tag{1.30}$$

Even if we imagine an extreme scenario where the macroscopic scale of the tokamak is on the order of decimeters, $L \sim 0.1\,\text{m}$, and the thermal motion of the particles is on the order of the speed of light, $v_T \sim 10^8\,\text{ms}^{-1}$, then the values (1.28) - (1.30) still comfortably satisfy conditions (1.25) - (1.27). Regular tokamak operation will be on larger macroscopic scales and lower thermal speeds, so we are justified in using plasma theory to model the ionised hydrogen gas.

1.4 Single Particle Motion

The most fundamental description of plasma behaviour happens at the particle level and all plasma phenomena can be reproduced using a sufficiently accurate simulation of all the plasma particles and their basic interactions. Therefore understanding the basic motion of particles in electromagnetic fields underpins the understanding of many interesting processes in a tokamak plasma including wave-particle interactions.

In the following discussion we will only consider electric and magnetic fields ($\mathbf{E}$ and $\mathbf{B}$) that are externally imposed and assume any induced fields from the particle motion are negligible in magnitude compared to the external fields. The

equation of motion for a single particle is given by the Lorentz force:

$$m \frac{d\mathbf{v}}{dt} = q \left(\mathbf{E} + \mathbf{v} \times \mathbf{B}\right) . \tag{1.31}$$

The simplest situation is that of a constant, uniform, straight magnetic field. It is convenient to separate the velocity into a sum of components parallel and perpendicular to the magnetic field. Defining $\mathbf{b} = \mathbf{B}/B$ where $B = |\mathbf{B}|$ then we can further define:

$$\mathbf{v}_{\parallel} = (\mathbf{v} \cdot \mathbf{b})\mathbf{b} , \tag{1.32}$$

$$\mathbf{v}_{\perp} = \mathbf{v} - \mathbf{v}_{\parallel} . \tag{1.33}$$

Substituting Eqs. (1.32)-(1.33) into Eq. (1.31) gives two independent equations of motion

$$\frac{d\mathbf{v}_{\parallel}}{dt} = \mathbf{0} , \tag{1.34}$$

$$\frac{d\mathbf{v}_{\perp}}{dt} = \left(\frac{q}{m}\right) \mathbf{v}_{\perp} \times \mathbf{B} , \tag{1.35}$$

from which we can see that the particle's parallel velocity is simply a constant. To find the perpendicular velocity we take the vector-product of the perpendicular equation of motion with the magnetic field. We use the vector triple product $\mathbf{A} \times (\mathbf{B} \times \mathbf{C}) = (\mathbf{A} \cdot \mathbf{C})\mathbf{B} - (\mathbf{B} \cdot \mathbf{C})\mathbf{A}$ with $\mathbf{v}_{\perp} \cdot \mathbf{B} = \mathbf{0}$ to give:

$$\frac{d(\mathbf{v}_{\perp} \times \mathbf{B})}{dt} = -\frac{qB^2}{m} \mathbf{v}_{\perp} . \tag{1.36}$$

We then rearrange Eq. (1.35) for $\mathbf{v}_{\perp} \times \mathbf{B}$ and substitute into Eq. (1.36):

$$\frac{d^2\mathbf{v}_{\perp}}{dt^2} = -\omega_c^2 \mathbf{v}_{\perp} , \tag{1.37}$$

where $\omega_c = \frac{qB}{m}$. This equation has oscillatory solutions. It is easy to see that the motion of $\mathbf{v}_{\perp}$ is a gyration of the particle around the magnetic field lines with the *cyclotron frequency*, ω_c. The radius at which the particles gyrate is called the *Larmor radius*, given by:

$$r_L = \frac{|\mathbf{v}_{\perp}|}{\omega_c} = \frac{mv_{\perp}}{qB} . \tag{1.38}$$

Positively charged particles rotate in a left-handed sense and negatively charged particles a right-handed one.

We consider an external force $\mathbf{F}$ in addition to the magnetic field and so

rewrite the equations of motion as:

$$m\frac{d\mathbf{v}_\parallel}{dt} = \mathbf{F}_\parallel \ , \tag{1.39}$$

$$m\frac{d\mathbf{v}_\perp}{dt} = \mathbf{F}_\perp + q\mathbf{v}_\perp \times \mathbf{B} \ . \tag{1.40}$$

The parallel velocity equation gives an obvious acceleration. The perpendicular is a first order linear ODE in $\mathbf{v}_\perp$ for which we have a solution to the homogeneous case. A particular solution for the inhomogeneous case can be found by assuming a constant velocity solution (labelled $\mathbf{v}_D$)

$$\mathbf{0} = \mathbf{F}_\perp + q\mathbf{v}_D \times \mathbf{B} \ , \tag{1.41}$$

$$\Rightarrow \mathbf{v}_D = \frac{\mathbf{F}_\perp \times \mathbf{B}}{qB^2} = \frac{\mathbf{F} \times \mathbf{B}}{qB^2} \ . \tag{1.42}$$

The overall velocity is the sum of the parallel motion, the gyration around the magnetic field lines and a constant drift velocity that is perpendicular both to the magnetic field lines and the applied force. A particular example of this applied force is that from an external electric field which leads to the so-called '$E \times B$' ("ee-cross-bee") drift. A particular property of this drift is that since $\mathbf{F} = q\mathbf{E}$ then $\mathbf{v}_{E\times B} = (\mathbf{E} \times \mathbf{B})/B^2$ the drift doesn't depend on the charge of the particles involved. Therefore there is no electric field set up by the charge separation that acts to counter the drift, unlike in charge-dependent drifts. This can have a serious effect on tokamak confinement.

Other particle drifts can be found by relaxing the condition that the magnetic field is homogeneous. Note that a charged particle gyrating around an electric field is effectively a current loop with magnetic dipole moment $\mu = mv_\perp^2/(2B)$ which is a constant of the system. It can also be seen from taking the scalar-product of Eq (1.31) (when $\mathbf{E} = \mathbf{0}$) with $\mathbf{v}$ that $d_t\left(v^2\right) = 0$, i.e. the magnetic field does no work on a particle, so cannot cause an overall acceleration. A changing magnetic field causes a particle's perpendicular velocity to change, since the magnetic moment is invariant, and so the parallel velocity of the particle must change accordingly to satisfy the no-work condition. This is the mechanism behind the *magnetic mirror force* which is given by the expression [1]:

$$\mathbf{F} = -\mu\nabla B \ . \tag{1.43}$$

We can now substitute this into the general expression for the drift velocities,

Eq. (1.42), to determine the 'grad-B' drift

$$\mathbf{v}_{\nabla B} = \pm \frac{v_\perp^2}{2\omega_c} \frac{\mathbf{B} \times \nabla B}{B^2} \ , \tag{1.44}$$

where the "$\pm$" refers to the sign of charge of the particle being considered. This drift leads to charge separation, unlike the $\mathbf{E} \times \mathbf{B}$ drift.

Now consider that the magnetic field lines are not necessarily straight. Here we apply an assumption that the Larmor radius of the particle is small compared to the length-scales over which the magnetic field varies in the perpendicular direction. This allows us to consider the drift for the particle's guiding centre separately from the gyro-motion. Moving into a reference frame that rotates with the guiding centre of the particle then we see that there is a centrifugal force acting on the particle [9]

$$\mathbf{F}_c = \frac{m v_\parallel^2}{R_c^2} \mathbf{R}_c \ , \tag{1.45}$$

where $\mathbf{R}_c$ is the curvature vector of the field lines. Note that all quantities are evaluated at the guiding centre path. The associated *curvature drift* is given by substituting Eq. (1.45) into Eq. (1.42).

1.5 MHD Theory

1.5.1 MHD equations

In a realistic fusion reactor environment the number of particles involved means that calculating for each individual trajectory and updating the electromagnetic fields self-consistently quickly becomes an intractable problem. One possible approach to build a self-consistent model is to consider particle distributions, as initially considered by Vlasov, the so-called kinetic approach. However, to sufficiently resolve a statistically significant amount of particles over a reasonably resolved phase space is computationally expensive and so the six dimensional phase space must be restricted to fewer dimensions [17].

Gyrokinetics is particular form of this approach that seperates the particle motion into the *guiding center motion* of the particle and the rotation of the particle about the magnetic field lines. Gyrokinetics averages over the rotation angle and so just considers the guiding center motion of each particle. This reduces the number of dimensions in phase space by one. Gyrokinetics is valid at frequencies that are small compared to the ion cyclotron frequency and is usually used for studying turbulent plasma behaviour [18].

Particle-In-Cell (PIC) simulations aim to overcome the computational expense by grouping large numbers of particles together as a single "macroparticle" which holds information about its position and velocity in a continuous space. The magnetic and electric fields values are held at the spatial grid nodes where the field equations are solved and then interpolated to the macroparticle position to update the macroparticle's information [17]. The fields are then self-consistently updated according to the new macroparticle information.

The approach we take here is considering the ionised gas as a fluid under the influence of electromagnetic fields, the magnetohydrodynamic (MHD) approach. There are various MHD approaches depending on the assumptions made in producing the model. In the work presented from here we will either be considering ideal-MHD or Hall-MHD. Both are non-relativistic models. It should be noted that we use the term Hall-MHD, for brevity, to refer to ideal Hall-MHD - that is to say that we consider resistivity to be negligible. We proceed with the more general Hall-MHD derivation and then relate that back to ideal-MHD.

The fluid equations for each charged particle species are:

$$\frac{\partial n_j}{\partial t} + \boldsymbol{\nabla} \cdot (n_j \mathbf{u}_j) = 0 \ , \tag{1.46}$$

$$m_j n_j \left(\frac{\partial}{\partial t} + \mathbf{u}_j \cdot \boldsymbol{\nabla} \right) \mathbf{u}_j = \mathbf{F}_j \ , \tag{1.47}$$

$$\left(\frac{\partial}{\partial t} + \mathbf{u}_j \cdot \boldsymbol{\nabla} \right) \frac{p_j}{\rho_j^{\gamma}} = 0 \ . \tag{1.48}$$

These represent conservation of mass, momentum and energy respectively. The index j corresponds to the charge carrier species. Any application of MHD in this thesis refers to a two-species plasma with a more massive ionic species (atomic nuclei) than the negative charge carriers (electrons). Therefore we can restrict $j \in \{i, e\}$ with $m_i \gg m_e$.

The mass equations assume that the total number of particles in each species remains constant. This negates any loss or gain processes of which there can be many in a fusion plasma; however, these can be added as source or sink terms if necessary. These processes are not important to our considerations.

The term F_j in the momentum equation refers to any forces acting on that fluid species. It consists of the Lorentz force and kinetic pressure gradient:

$$F_j = Z_j e n_j (\mathbf{E} + \mathbf{u}_j \times \mathbf{B}) - \nabla p_j \ . \tag{1.49}$$

More generally we should consider the pressure tensor $\mathbf{P}$ rather than the scalar

pressure. However, if we assume an isotropic pressure then $\boldsymbol{\nabla} \cdot \mathbf{P} = \nabla p$ [5]. This is equivalent to the assumption that the collisional timescale of the plasma is short compared to the fluid, i.e. MHD, timescale [19].

The energy equation represents an adiabat for an ideal gas. We have ignored heating/cooling terms on the right hand side as most of these processes do not happen on MHD timescales [1]. One term that is conspicuously missing is energy transfer (through collisions) to the other species - this implies Ohmic heating of the plasma species. This term is considered negligible in the ideal-MHD regime as the plasma is assumed to be perfectly conducting, i.e. zero resistivity.

Now we require Maxwell's equations to close our fluid equations:

$$\boldsymbol{\nabla} \times \mathbf{E} = -\frac{\partial \mathbf{B}}{\partial t} \ , \tag{1.50}$$

$$\boldsymbol{\nabla} \times \mathbf{B} = \mu_0 \left(\mathbf{J} + \epsilon_0 \frac{\partial \mathbf{E}}{\partial t} \right) \ , \tag{1.51}$$

$$\boldsymbol{\nabla} \cdot \mathbf{E} = \frac{\rho_c}{\epsilon_0} \ , \tag{1.52}$$

$$\boldsymbol{\nabla} \cdot \mathbf{B} = 0 \ . \tag{1.53}$$

Note that ρ_c is the charge density, not to be confused with ρ, which we use in general to denote the mass density. MHD describes the macroscopic stability of the plasma and therefore the characteristic MHD lengthscale, L, is comparable to the overall plasma size. Similarly we say that the characteristic velocity of the MHD model is the ion thermal speed V_{Ti}, from which we can define a characteristic timescale $\tau \sim a/V_{Ti}$ or frequency $\omega = \tau^{-1}$. Then our MHD assumptions follow:

$$L \gg r_{Li} \gg r_{Le} \ , \tag{1.54}$$

$$\omega_{ce} \gg \omega_H \gg \bar{\nu}_{ei} \quad || \quad \omega_{ce} \gg \omega_{ci} \gg \omega_I \gg \bar{\nu}_{ei} \ , \tag{1.55}$$

$$V_{Ti} \ll V_{Te} \ll c \ , \tag{1.56}$$

where ω_H and ω_I refer to Hall- and ideal-MHD respectively. $\bar{\nu}_{ei}$ is the electron-ion collision frequency.

The electric charge density in Gauss' law $\rho_c = Z_i e n_i - e n_e$ is assumed to be negligible by the quasineutrality of the plasma. Therefore $\boldsymbol{\nabla} \cdot \mathbf{E} \ll e n_e$ and $n \equiv Z_i n_i \approx n_e$. The frequency assumption (1.55) implies that we don't have to consider collisionality and that MHD events are much slower than the electron response. Therefore the electron inertia term is negligible. Finally Eq. (1.56) implies that the displacement current term in Maxwell's equations is negligible.

By multiplying the mass-conservation equation by the respective particle

mass and summing we get the single fluid equation:

$$\frac{\partial \rho}{\partial t} + \boldsymbol{\nabla} \cdot (\rho \mathbf{v}) = 0 \ , \tag{1.57}$$

where $\rho \equiv m_i n_i + m_e n_e \approx m_i n_i$ and $\rho \mathbf{v} \equiv m_i n_i \mathbf{u}_i + m_e n_e \mathbf{u}_e$.

By summing the momentum equations and noting that $\mathbf{J} = Z_i e n_i \mathbf{u}_i - e n_e \mathbf{u}_e$ then we obtain:

$$\rho \left(\frac{\partial}{\partial t} + \mathbf{v} \cdot \boldsymbol{\nabla} \right) \mathbf{v} + \frac{m_i m_e n_i}{Z \rho e^2} (Z m_e - m_i) \mathbf{J} \cdot \boldsymbol{\nabla} \left(\frac{1}{\rho} \mathbf{J} \right) = \mathbf{J} \times \mathbf{B} - \nabla p \ , \tag{1.58}$$

where p is the sum of the two species' pressures. A quick comparison of terms shows that the $\mathbf{J} \cdot \boldsymbol{\nabla} \left(\frac{1}{\rho} \mathbf{J} \right)$ term is negligible.

Multiplying each momentum equation by the species charge over mass we obtain an Ohm's law:

$$\begin{aligned} &\frac{\partial \mathbf{J}}{\partial t} + \mathbf{J} \cdot \boldsymbol{\nabla} \mathbf{v} + (m_e n_e \mathbf{u}_i + m_i n_i \mathbf{u}_e) \cdot \boldsymbol{\nabla} \left(\frac{1}{\rho} \mathbf{J} \right) = \\ &\frac{Z e^2 \rho}{m_i m_e} (\mathbf{E} + \mathbf{v} \times \mathbf{B}) + \frac{e (Z n_e m_e^2 - n_i m_i^2)}{m_i m_e \rho} \mathbf{J} \times \mathbf{B} - \frac{Ze}{m_i} \nabla p_i - \frac{e}{m_e} \nabla p_e \ . \end{aligned} \tag{1.59}$$

Using the assumptions about particle mass, $m_i \gg m_e$, and frequency, Eq. (1.55) we come to the following form of Ohm's law:

$$\mathbf{E} = -\mathbf{v} \times \mathbf{B} + \frac{1}{en} \mathbf{J} \times \mathbf{B} - \frac{1}{en} \nabla p_e \ . \tag{1.60}$$

The last two terms are called the Hall and Battery terms respectively. Both terms are only considerable for MHD frequencies $\omega \sim \omega_{ci}$; we neglect both of them in ideal MHD. Then the strength of the Battery relative to the Hall term is proportional to

the plasma-β. This gives the full equation set of Hall-MHD:

$$\frac{\partial \rho}{\partial t} + \boldsymbol{\nabla} \cdot (\rho \mathbf{v}) = 0 \ , \tag{1.61}$$

$$\rho \left(\frac{\partial}{\partial t} + \mathbf{v} \cdot \boldsymbol{\nabla} \right) \mathbf{v} = \mathbf{J} \times \mathbf{B} - \nabla p \ , \tag{1.62}$$

$$\left(\frac{\partial}{\partial t} + \mathbf{v} \cdot \boldsymbol{\nabla} \right) \frac{p}{\rho^{\gamma}} = 0 \ , \tag{1.63}$$

$$\boldsymbol{\nabla} \times \mathbf{E} = -\frac{\partial \mathbf{B}}{\partial t} \ , \tag{1.64}$$

$$\mathbf{E} = -\mathbf{v} \times \mathbf{B} + \frac{1}{en} \mathbf{J} \times \mathbf{B} - \frac{1}{en} \nabla p_e \ , \tag{1.65}$$

$$\boldsymbol{\nabla} \times \mathbf{B} = \mu_0 \mathbf{J} \ , \tag{1.66}$$

$$\boldsymbol{\nabla} \cdot \mathbf{B} = 0 \ . \tag{1.67}$$

It should be noted that the MHD description does not capture the full range of plasma phenomena, even at low frequencies within the model's assumed ordering. When approaching the ion-cyclotron frequency, the MHD description predicts a resonance for the Shear Alfvén wave (one of the MHD waves described in Section 1.6). As the wave frequency approaches the resonance the wavenumber tends to infinity, $k \to \infty$, and the group velocity tends to zero [20]. This leads to plasma waves with non-physical energies and so clearly insufficient physics is captured in the MHD description to correctly describe this situation. Kinetic theory is required to describe the mode conversion and dissipation of energy when these waves encounter a frequency match with the ion cyclotron frequency at some point within the plasma domain. However, the MHD description is sufficient within the remit of this thesis as MHD includes the essential physics required for predicting the frequency and wave structure of the class of wavemodes that we will study.

1.5.2 Linearised MHD Equations

We linearise the MHD equations in order to remove some of the complexity of the equation and make it easier to solve. The trade-off is that the solutions have limited validity. We make the assumption that there is a full solution to the equations that can be written as $\mathbf{x} = \mathbf{x}_0 + \epsilon \mathbf{x}_1 + \epsilon^2 \mathbf{x}_2 + ...$ where $\epsilon \ll 1$. To linearise we substitute $\mathbf{x}$ into the equations and negate any terms of order ϵ^2 or higher. We choose $\mathbf{x}_0$ to be a known equilibrium solution to the MHD equations. This means $\mathbf{x}_0$ solves the original equations and so terms that only involve equilibrium terms disappear from the linearised form, leaving only terms with exactly one linear contribution. For brevity we absorb the ϵ^n prefactor into each $\mathbf{x}_n$ term when presenting the work. We

also pre-empt the assumption of equilibria free from bulk flows (i.e. $\mathbf{v}_0 = 0$) though this is not required in general. The linearised equations are:

$$\frac{\partial \rho_1}{\partial t} + \boldsymbol{\nabla} \cdot (\rho_0 \mathbf{v}_1) = 0 \ , \tag{1.68}$$

$$\rho_0 \frac{\partial \mathbf{v}_1}{\partial t} = \mathbf{J}_0 \times \mathbf{B}_1 + \mathbf{J}_1 \times \mathbf{B}_0 - \nabla p_1 \ , \tag{1.69}$$

$$\frac{\partial}{\partial t}\left(\frac{p_1}{\rho_0^\gamma} - \frac{\gamma p_0}{\rho_0^{\gamma+1}}\rho_1\right) + \mathbf{v}_1 \cdot \boldsymbol{\nabla} \frac{p_0}{\rho_0^\gamma} = 0 \ , \tag{1.70}$$

$$\boldsymbol{\nabla} \times \mathbf{E}_1 = -\frac{\partial \mathbf{B}_1}{\partial t} \ , \tag{1.71}$$

$$\begin{aligned} \mathbf{E}_1 = -\mathbf{v}_1 \times \mathbf{B}_0 + \frac{1}{en_0}\mathbf{J}_1 \times \mathbf{B}_0 + \frac{1}{en_0}\mathbf{J}_0 \times \mathbf{B}_1 \\ -\frac{n_1}{en_0^2}\mathbf{J}_0 \times \mathbf{B}_0 - \frac{1}{en_0}\nabla p_{e1} + \frac{n_1}{en_0^2}\nabla p_{e0} \ , \end{aligned} \tag{1.72}$$

$$\boldsymbol{\nabla} \times \mathbf{B}_1 = \mu_0 \mathbf{J}_1 \ , \tag{1.73}$$

$$\boldsymbol{\nabla} \cdot \mathbf{B}_1 = 0 \ . \tag{1.74}$$

1.5.3 MHD Equilibrium

The study of MHD equilibria goes naturally alongside that of plasma stability. The equilibrium equation is generally difficult to solve for plasmas that have a higher dimensionality than 1. We make the following assumptions to find an equation for MHD equilibrium in a 2-dimensional 'tokamak-like' geometry, with ignorable co-ordinate ϕ. We assume that the plasma is stationary, $\frac{\partial}{\partial t} \equiv 0$, and that the plasma has no bulk flows, $\mathbf{v} = \mathbf{0}$. In actuality, spherical tokamaks may have considerable toroidal plasma rotation due to the *neutral beam injection* (NBI) heating, where beams of neutral particles are injected tangentially into the plasma at high velocity. However, the main effect of this is to cause a Doppler shift to the frequency of plasma waves which is typically small for waves in the frequency range we are concerned about.

We start from the force-balance equation:

$$\mathbf{J} \times \mathbf{B} = \nabla p \ , \tag{1.75}$$

which must be satisfied in the tokamak. This represents the balance struck by the plasma (kinetic) pressure, *magnetic pressure* and *magnetic tension* forces. To explicitly express the magnetic pressure and tension forces we separate out the left

hand side of the above equation:

$$(\boldsymbol{\nabla} \times \mathbf{B}_0) \times \mathbf{B}_0 = \mathbf{B}_0 \cdot \boldsymbol{\nabla}\mathbf{B}_0 - B_0 \boldsymbol{\nabla} B_0 \ . \tag{1.76}$$

The first term of the right hand side refers to the magnetic tension force which acts against magnetic field line bending. The second term is the magnetic pressure force, which acts against the accumulation of magnetic flux. The components of these forces in the direction of the magnetic field must cancel, so using the notation $\boldsymbol{\nabla}_\parallel$ to refer to the gradient in the magnetic field direction we define $\boldsymbol{\nabla}_\perp = \boldsymbol{\nabla} - \boldsymbol{\nabla}_\parallel$. Then we can rewrite (1.76) as:

$$(\boldsymbol{\nabla} \times \mathbf{B}_0) \times \mathbf{B}_0 = (\mathbf{B}_0 \cdot \boldsymbol{\nabla}\mathbf{B}_0)_\perp - B_0 \boldsymbol{\nabla}_\perp B_0 \ . \tag{1.77}$$

It clearly follows from (1.75) by taking scalar-products that

$$\mathbf{B} \cdot \nabla p = \mathbf{J} \cdot \nabla p = \mathbf{0} \ . \tag{1.78}$$

Therefore magnetic field lines and lines of current both lie on surfaces of constant pressure.

The solenoidal condition written in cylindrical coordinates with an ignorable angle reads:

$$\nabla \cdot \mathbf{B} = \frac{1}{R}\frac{\partial}{\partial R}(RB_R) + \frac{\partial B_z}{\partial z} = 0 \ . \tag{1.79}$$

Like incompressible fluid flow we can take a stream function, ψ, so that:

$$B_R = -\frac{1}{R}\frac{\partial \psi}{\partial z} \ , \tag{1.80}$$

$$B_z = \frac{1}{R}\frac{\partial \psi}{\partial R} \ . \tag{1.81}$$

The surfaces of constant ψ are the boundaries of streamtubes and so there is no magnetic flux through these surfaces. For our axisymmetric setup these surfaces form a set of nested tori [9]. Using $\nabla\phi = \frac{1}{R}\hat{\phi}$ we can rewrite the equilibrium magnetic field [21]:

$$\mathbf{B} = RB_\phi \nabla\phi + \nabla\psi \times \nabla\phi \ . \tag{1.82}$$

Considering the magnetic vector potential

$$\mathbf{B} = \nabla \times \mathbf{A} = -\frac{\partial A_\phi}{\partial z}\hat{R} + \left(\frac{\partial A_R}{\partial z} - \frac{\partial A_z}{\partial R}\right)\hat{\phi} + \frac{1}{R}\frac{\partial}{\partial R}(RA_\phi)\hat{z} \ , \tag{1.83}$$

we see that $\psi = RA_\phi$ (up to an additive constant). Ampère's law is analogous to

the above equation and $\nabla \cdot \mathbf{J} = 0$ so we can introduce a stream function for the current, say f, such that:

$$f = RB_\phi \ , \tag{1.84}$$

$$J_R = -\frac{1}{\mu_0 R}\frac{\partial f}{\partial z} \ , \tag{1.85}$$

$$J_z = \frac{1}{\mu_0 R}\frac{\partial f}{\partial R} \ . \tag{1.86}$$

The magnetic field lines and current lines lie in the same surfaces of constant pressure and so these must be the surfaces of constant value for the stream functions ψ and f. Therefore we can choose to write $f = f(\psi)$ and $p = p(\psi)$, and Eq. (1.82) becomes:

$$\mathbf{B} = f(\psi)\nabla\phi + \nabla\psi \times \nabla\phi \ . \tag{1.87}$$

Now, omitting the derivation, we can come to the Grad-Shafranov equation describing the static equilibrium of axisymmetric toroidal plasmas in ideal MHD without bulk flows [9, 21]

$$R\frac{\partial}{\partial R}\left(\frac{1}{R}\frac{\partial\psi}{\partial R}\right) + \frac{\partial^2\psi}{\partial z^2} = -\mu_0 R^2 p'(\psi) - f(\psi)f'(\psi) \ . \tag{1.88}$$

The quantity ψ is constant on a given flux surface and so can be used to label flux surfaces provided that it is an injective function to the flux surfaces. We take ψ to be our "radial" coordinate where radial now describes the direction that has its axis at the magnetic axis and moves outwards over the flux surfaces. The toroidal direction remains the same. To generalise to non-circular tori we define the "poloidal" direction to mean the angular direction around the magnetic axis that follows the flux surface boundary and is orthogonal to the toroidal direction.

To relate to ψ physically we take the poloidal magnetic flux given by

$$\psi_p = \int_A \mathbf{B}_p \cdot d\mathbf{A} \ , \tag{1.89}$$

where A is the ribbon-shaped area formed by taking the line from the magnetic axis to a particular flux surface and then rotating 2π toroidally around the z-axis [19]. Without loss of generality we assume that the ribbon extends from the magnetic axis to higher major radius so that $\mathbf{B}_p$ and $\mathbf{A}$ are in the $\hat{z}$-direction. Recalling Eq. (1.81):

$$\psi_p = \int_0^{2\pi} d\phi \int_{R_m}^{R} B_z R' dR = 2\pi(\psi(R) - \psi(0)) \ . \tag{1.90}$$

So ψ is the poloidal magnetic flux per radian, barring an additive constant. For brevity we will refer to ψ simply as the poloidal flux function where there is no ambiguity.

Solovev Equilibrium

Solovev [22] proposed an analytical solution to the above form of the Grad-Shafranov equation by assuming the form of the two free functions $f(\psi)$ and $p(\psi)$. Solovev originally looked for solutions by expanding ψ around the magnetic axis, noticing that exact solutions can be found if one assumes $\mu_0 p'(\psi) = -F$ and $f(\psi)f'(\psi) = -E$ where E, F are constants. With these profiles the Grad-Shafranov equation, Eq. (1.88), becomes:

$$R\frac{\partial}{\partial R}\left(\frac{1}{R}\frac{\partial \psi}{\partial R}\right) + \frac{\partial^2 \psi}{\partial z^2} = E + FR^2 \ . \tag{1.91}$$

So Solovev equilibria refer to solutions of the Grad-Shafranov equations that have free functions of the form:

$$f(\psi) = \sqrt{R_0^2 B_0^2 - 2E\psi} \ , \tag{1.92}$$

$$\mu_0 p(\psi) = \mu_0 p_0 - F\psi \ . \tag{1.93}$$

However, specifying E, F is not enough to fix a unique solution. We detail two possible solution methods that are implemented in Whales2.

The first implementation of a Solovev equilibrium is based on [22, 23]. The equilibrium is found by Taylor expanding the poloidal magnetic flux, ψ, in the spatial variables R, Z around the magnetic axis. Terms up to 4th order are kept such that ψ solves the Grad-Shafranov equation exactly. These can be split into a particular solution of Eq. (1.91) and a homogeneous solution for the left hand side of that equation:

$$\psi_p = \frac{1}{2}\left(E + FR^2\right) Z^2 \ , \tag{1.94}$$

$$\psi_{h0} = 1 \ , \tag{1.95}$$

$$\psi_{h1} = R^2 \ , \tag{1.96}$$

$$\psi_{h2} = R^4 - 4R^2 Z^2 \ . \tag{1.97}$$

Then ψ can be written as a linear combination of these functions. When the problem

is normalised such that:

$$\psi(R,Z) \to \hat{\psi}(x,y) = \Psi_0 \psi \ , \tag{1.98}$$

$$R \to x = \frac{R - R_0}{a} \ , \tag{1.99}$$

$$Z \to y = \frac{Z}{a} \ , \tag{1.100}$$

then Eq. (1.91) becomes:

$$\frac{\partial^2 \hat{\psi}}{\partial x^2} + \frac{\partial^2 \hat{\psi}}{\partial y^2} - \frac{\epsilon}{1+\epsilon}\frac{\partial \hat{\psi}}{\partial x} = A + Bx\left(1 + \frac{\epsilon}{2}x\right) \ . \tag{1.101}$$

The particular solution (1.94) is normalised:

$$\hat{\psi}_p = \frac{1}{2}\left(A + Bx\left(1 + \frac{\epsilon}{2}x\right)\right) y^2 \ , \tag{1.102}$$

but the homogeneous solutions are scale independent and so can remain unchanged. We write $\hat{\psi}$ as the linear combination:

$$\hat{\psi} = \hat{\psi}_p + \sigma_0 \psi_{h0} + \sigma_1 \psi_{h1} + \sigma_2 \psi_{h2} \ . \tag{1.103}$$

There are 5 free parameters to the scaled problem $A, B, \sigma_0, \sigma_1, \sigma_2$ and we impose conditions to fix these parameters. We fix the gauge by imposing that $\hat{\psi}(d,0) = 0$ and the regularity condition $\frac{\partial \psi}{\partial x}(d,0) = 0$, where $x = d$ is the magnetic axis. The solution is up-down symmetric and so automatically satisfies $\frac{\partial \psi}{\partial y}(x,0) = 0$. These conditions imply that:

$$\sigma_0 = R_m^4 \sigma_2 \ , \tag{1.104}$$

$$\sigma_1 = -2R_m^2 \sigma_2 \ , \tag{1.105}$$

$$R_m = R_0 + ad \ . \tag{1.106}$$

Now we specify points on the outer flux surface. $\hat{\psi}(1,0) = 1$ and $\hat{\psi}(-1,0) = 1$ together give the value of x at the magnetic axis and σ_2:

$$d = \frac{1}{\epsilon}\left(\sqrt{1+\epsilon^2} - 1\right) \ , \tag{1.107}$$

$$\sigma_2 = \frac{1}{4R_0^2 a^2}. \tag{1.108}$$

Finally, instead of specifying the free parameters A, B (equivalent to specifying E, F) we specify the elongation of the outer flux surface on the line $x = 0$, κ_0, and the

triangularity of the outer surface, τ. Note that this definition of elongation may not be the same as the elongation quoted for tokamak geometries, which is usually the one we defined in Section 1.2. We apply these conditions to give the values for A, B:

$$A = 2\left(1 + \frac{1 - \frac{1}{4}\epsilon^2}{\kappa_0^2}\right) , \tag{1.109}$$

$$B = 4\epsilon\left(1 + \tau\frac{1 - \frac{1}{4}\epsilon^2}{\kappa_0^2}\right) , \tag{1.110}$$

and so the magnetic flux function is:

$$\hat{\psi} = \left(x - \frac{\epsilon}{2}(1 - x^2)\right)^2 + \left(1 - \frac{\epsilon^2}{4}\right)(1 + \epsilon\tau x(2 + \epsilon x))\left(\frac{y}{\kappa_0}\right)^2 \tag{1.111}$$

We then transform back to the original problem with an additional free parameter that specifies the magnitude of the magnetic flux. The inputs that Whales2 takes for this Solovev implementation are:

$$B_0(0) \text{ - equilibrium magnetic field at the magnetic axis ,} \tag{1.112}$$

$$a \text{ - minor radius of the plasma ,} \tag{1.113}$$

$$R_0 \text{ - major radius of the magnetic axis ,} \tag{1.114}$$

$$\kappa_0 \text{ - elongation of the plasma surface at the geometric centre ,} \tag{1.115}$$

$$\tau \text{ - triangularity of the plasma surface ,} \tag{1.116}$$

$$\alpha \text{ - parameter related to the total poloidal magnetic flux .} \tag{1.117}$$

These inputs are used to calculate the following quantities of the Solovev solution:

$$\Psi_0 = \frac{a^2 B_0}{\alpha} \ , \tag{1.118}$$

$$A = 2\left(1 + \frac{1 - \frac{1}{4}\epsilon^2}{\kappa_0^2}\right) \ , \tag{1.119}$$

$$B = 4\epsilon\left(1 + \tau\frac{1 - \frac{1}{4}\epsilon^2}{\kappa_0^2}\right) \ , \tag{1.120}$$

$$E = \Psi_0 \frac{R_0}{a^3}(\epsilon A - \frac{1}{2}B) \ , \tag{1.121}$$

$$F = \frac{\Psi_0 B}{2R_0 a^3} \ , \tag{1.122}$$

$$x = \frac{1}{\epsilon}\left(\left(1 + 2\epsilon\sqrt{\hat{\psi}}\cos\theta + \epsilon^2\right)^{\frac{1}{2}} - 1\right) \ , \tag{1.123}$$

$$y = \frac{\kappa\sqrt{\hat{\psi}}\sin\theta}{\left(\left(1 - \frac{1}{4}\epsilon^2\right)\left(1 + 2\epsilon\tau\sqrt{\hat{\psi}}\cos\theta + \epsilon^2\tau\right)\right)^{\frac{1}{2}}} \ , \tag{1.124}$$

The functions that specify the equilibrium then follow as:

$$R = R_0 + ax \tag{1.125}$$

$$Z = ay \tag{1.126}$$

$$\psi = \Psi_0\hat{\psi} \tag{1.127}$$

$$\mu_0 p(\psi) = \frac{\beta_0 B_0^2}{2} - F\psi \tag{1.128}$$

$$f(\psi) = \sqrt{R_0^2 B_0^2 - 2E\psi} \tag{1.129}$$

where the value of β_0 is set by the boundary condition for the pressure (in this case that the pressure is zero at the outer plasma boundary - see Section 2.5.2). This condition implies that:

$$\beta_0 = \frac{B\epsilon}{\alpha^2} \ . \tag{1.130}$$

There is also a condition on α to ensure that $f(\psi)$ is always a real quantity. The condition reads:

$$\alpha^2 > (1 - \tau)\frac{(4 - \epsilon^2)\epsilon^2}{\kappa^2} \qquad \text{if} \quad \tau < 1 \ . \tag{1.131}$$

It is useful to know the approximate magnitudes of the poloidal and toroidal com-

ponents of the equilibrium magnetic field, which can be seen as:

$$B_t = |f(\psi)\boldsymbol{\nabla}\phi| \sim B_0 \ , \tag{1.132}$$

$$B_p = |\boldsymbol{\nabla}\psi \times \boldsymbol{\nabla}\phi| \sim \frac{\epsilon B_0}{\alpha} \ . \tag{1.133}$$

The second implementation of the Solovev equilibrium follows [19, 24]. The derivation is much the same as for the previous case, except terms of a higher order are kept in the Taylor expansion of ψ around the magnetic axis. Keeping terms up to 6th order in R, Z still allows an exact solution to be found, but now there are extra free parameters. Some definitions differ from the first implementation, i.e.:

$$R = R_0 x \ , \tag{1.134}$$

$$Z = R_0 y \ . \tag{1.135}$$

The scaled Grad-Shafranov equation is:

$$x\frac{\partial}{\partial x}\left(\frac{1}{x}\frac{\partial\hat{\psi}}{\partial x}\right) + \frac{\partial^2\hat{\psi}}{\partial y^2} = A + (1-A)x^2 \ , \tag{1.136}$$

$$A = \frac{E}{E + FR_0^2} \ . \tag{1.137}$$

So now the particular and homogeneous solutions are:

$$\hat{\psi}_p = \frac{x^4}{8} + A\left(\frac{x^2}{2}\ln x - \frac{x^4}{8}\right) \ , \tag{1.138}$$

$$\psi_{h0} = 1 \ , \tag{1.139}$$

$$\psi_{h1} = x^2 \ , \tag{1.140}$$

$$\psi_{h2} = y^2 - x^2 \ln x \ , \tag{1.141}$$

$$\psi_{h3} = x^4 - 4x^2y^2 \ , \tag{1.142}$$

$$\psi_{h4} = 2y^4 - 9y^2x^2 + 3x^4\ln x - 12x^2y^2\ln x \ , \tag{1.143}$$

$$\psi_{h5} = x^6 - 12x^4y^2 + 8x^2y^4 \ , \tag{1.144}$$

$$\psi_{h6} = 8y^6 - 140y^4x^2 + 75y^2x^4 - 15(x^6 - 12x^4y^2 + 8x^2y^4)\ln x \ . \tag{1.145}$$

Again, $\hat{\psi}$ is a linear combination of these functions and the coefficients are determined by specifying points of the outer surface shape so that they match those

points given by the parametric equations:

$$R = R_0 + a\cos(\vartheta + \delta \sin\vartheta) \ , \tag{1.146}$$

$$Z = a\kappa \sin\vartheta \ , \tag{1.147}$$

where $\sin\delta = \tau$. This sets up a set of seven linear equations that can then be solved numerically to give the coefficients of the linear combination of homogeneous solutions. The inputs for this implementation of a Solovev solution are then:

$$B_0(0) \text{ - equilibrium magnetic field at the magnetic axis} \ , \tag{1.148}$$

$$a \text{ - minor radius of the plasma} \ , \tag{1.149}$$

$$R_0 \text{ - major radius of the magnetic axis} \ , \tag{1.150}$$

$$\kappa \text{ - elongation of the plasma surface} \ , \tag{1.151}$$

$$\tau \text{ - triangularity of the plasma surface} \ , \tag{1.152}$$

$$E \text{ - 'gradient of the current flux function'} \ , \tag{1.153}$$

$$F \text{ - 'gradient of the pressure function'} \ . \tag{1.154}$$

More precisely, $E = -f(\psi)f'(\psi)$ and $F = -\mu_0 p'(\psi)$ as in the first equilibrium outlined. In general we will use this second implementation of the Solovev equilibrium, unless stated otherwise, as it gives greater control of the plasma shape.

1.6 MHD Waves

There are three distinct wave types that are supported in an MHD uniform plasma setup. Rearranging the linearised Hall-MHD equations for low plasma-β plasmas gives the following wave equations:

$$\left(\frac{\partial^4}{\partial t^4} - (C_s^2 + V_A^2)\frac{\partial^2}{\partial t^2}\boldsymbol{\nabla}^2 + C_s^2 V_A^2 \nabla_\parallel^2 \nabla^2\right) p_T^{'} = -\frac{V_A^2}{\omega_{c_i}}(\mathbf{B}_0 \cdot \boldsymbol{\nabla})\frac{\partial^3 \mathbf{J}_\parallel^{'}}{\partial t^3} \ , \tag{1.155}$$

$$\left(\frac{\partial^2}{\partial t^2} - V_A^2 \nabla_\parallel^2\right)\frac{\partial \mathbf{J}_\parallel^{'}}{\partial t} = \frac{V_A^2}{\omega_{c_i} B_0}\nabla_\parallel^2 \nabla^2 \left(\frac{\partial^2}{\partial t^2} - C_s^2 \nabla^2\right) p_T^{'} \ . \tag{1.156}$$

Here p_T is the total pressure perturbation (the sum of plasma and magnetic pressure perturbations), $C_s^2 = \gamma p_0/\rho_0$ is the sound speed in the plasma, and $V_A^2 = B_0^2/(\rho_0\mu_0)$ is the *Alfvén speed*. Eq. (1.155) is called the *magnetoacoustic equation* and Eq. (1.156) is the Alfvén equation. These are coupled by the Hall term. To learn qualitatively about the waves at low frequencies, we neglect the Hall term. We

assume a uniform plasma and so postulate plane-wave solutions where the perturbed quantities $\sim e^{i(\mathbf{k}\cdot\mathbf{x}-\omega t)}$. This leads to the dispersion relations:

$$\omega^2 = \frac{1}{2}(C_s^2 + V_A^2)k^2\Big(1 \pm \sqrt{1 - 4\frac{C_T^2}{C_s^2 + V_A^2}\frac{k_\parallel^2}{k^2}}\Big) \ , \tag{1.157}$$

$$\omega^2 = V_A^2 k_\parallel^2 \ , \tag{1.158}$$

where $C_T^2 = C_s^2 V_A^2/(C_s^2+V_A^2)$ is the *tube speed*. The $\pm$ solutions of Eq. (1.157) refer to the *fast-magnetoacoustic* (or *Compressional Alfvén*) wave and *slow-magnetoacoustic* wave respectively. Eq. (1.158) is the dispersion relation for the *shear Alfvén wave*.

The shear Alfvén wave perturbs the magnetic field lines transversely both to the direction of wave propagation and the equilibrium magnetic field direction. Thus the restoring force for the wave is the magnetic tension, analagous to the restoring force in a plucked string. This wave is incompressible, with zero density and pressure perturbations. The shear Alfvén wave is anisotropic and does not propagate transversely to the equilibrium magnetic field - this is obvious from inspecting the dispersion relation (1.158). The fast- and slow-magnetoacoustic waves are both compressible with the magnetic and plasma pressures as their restoring forces. The magnetic pressure resists the bunching of magnetic field lines, similarly to kinetic pressure acting on a particle system. Both waves have longitudinal and transverse components. The slow wave is similarly anisotropic as the shear Alfvén wave and only flows along equilibrium magnetic field lines. The fast wave flows almost isotropically, with a slight preference to travel perpendicular to the equilibrium magnetic field. All three wave types, as derived here in a uniform medium, are non-dispersive but this does not hold generally.

It is possible to derive the dispersion relations for these waves in Hall-MHD. Omitting the derivation we have:

$$(\omega^2 - V_A^2 k^2 \cos^2\theta)(\omega^4 - (C_s^2 + V_A^2)k^2\omega^2 + C_s^2 V_A^2 k^4 \cos^2\theta) = \frac{V_A^4}{\omega_{ci}^2} k^4 \cos^2\theta \ \omega^2(\omega^2 - C_s^2 k^2) \ , \tag{1.159}$$

where θ is the angle between $\mathbf{k}$ and the equilibrium magnetic field. For the case of perpendicular propagation ($\theta = \frac{\pi}{2}$) then the slow and shear waves vanish and the fast wave travels with phase velocity $\omega/k = \sqrt{C_s^2 + V_A^2}$. This exactly replicates the ideal MHD case. For parallel propagation ($\theta = 0$) the slow wave decouples from the

other two wave types and the dispersion relations become:

$$\text{Slow} : \omega^2 = C_s^2 k^2 \ , \tag{1.160}$$

$$\text{Fast/Alfvén} : \omega^2 = \frac{V_A^2 k^2}{2}\left(2 + \frac{V_A^2 k^2}{\omega_{ci}^2} \pm \frac{V_A k}{\omega_{ci}}\sqrt{4 + \frac{V_A^2 k^2}{\omega_{ci}^2}}\right) \ . \tag{1.161}$$

If we solve Eq. (1.161) for $V_A^2 k^2$ instead the two wave solutions are represented more clearly:

$$\text{Fast} : V_A^2 k^2 = \frac{\omega^2}{1 + \frac{\omega}{\omega_{ci}}} \ , \tag{1.162}$$

$$\text{Alfvén} : V_A^2 k^2 = \frac{\omega^2}{1 - \frac{\omega}{\omega_{ci}}} \ , \tag{1.163}$$

from which we see that the Alfvén wave has a resonance as $\omega \to \omega_{ci}$, the ion-cyclotron frequency. As the frequency approaches the ion-cylotron frequency, the wave number tends to infinity. At short-wavelengths dissipative and kinetic effects will become important, so the MHD description is not sufficient. Note that this is different to the wave-particle resonances described later. For waves with significantly higher frequencies it is necessary to retain more terms in the MHD model but we will not describe them here as they are not of interest to this thesis.

Plasma normal modes

In geometries relevant to fusion devices, i.e. plasma cylinders and tori, the plasmas are bounded, meaning the plane-wave solutions are now *normal modes* of the plasma. We consider a plasma cylinder, described by ideal-MHD, with azimuthal and axial symmetry, and axial periodicity. For the cylindrical co-ordinates (r, θ, z), the product of the wavenumber and position vector is written:

$$\mathbf{k} \cdot \mathbf{x} = k_r r + m\theta + kz \ . \tag{1.164}$$

The periodicity condition implies that $m \in \mathbb{Z}$ and $(2\pi k/L_z) \in \mathbb{Z}$. It is common to set $L_z = 2\pi R_0$, the so-called *straight tokamak* approximation. The three types of MHD-wave that we have established now exist in the cylinder as discrete or continuous spectra. In the homogeneous plasma case the slow-magnetoacoustic modes and the shear Alfvén modes each form an infinitely degenerate spectrum at a particular frequency, say ω_S and ω_A respectively [25]. The introduction of radial inhomogeniety extends these infinitely degenerate points into continua, $\omega_S(r)$ and $\omega_A(r)$. Both the

slow and the Alfvén modes may also have two associated discrete spectra located either side of their respective continua in frequency-space, which may form a *cluster point* at an extremum of the continua for certain plasma equilibria [26]. The fast-magnetoacoustic modes form a discrete spectrum of modes with a cluster point at $\omega = \infty$. Since we are now dealing with normal modes of the fast wave we change our terminology and refer to them as *Compressional Alfvén Eigenmodes* (CAEs). Modes in the slow and shear Alfvén continua are localised to a particular magnetic flux surface with which their frequency is matched, their so-called *resonant surface*. Discrete modes of all three Alfvén wave branches, however, are global modes that can exist across the plasma domain.

Consider a toroidal geometry described by (s, ϕ, ϑ), with s a proxy radial co-ordinate, ϕ the toroidal angle, and ϑ the poloidal angle. Eq. (1.164) is now written:

$$\mathbf{k} \cdot \mathbf{x} = k_r r + n\phi + m\theta \ . \tag{1.165}$$

The periodicity condition applies to the toroidal and poloidal directions, implying $m, n \in \mathbb{Z}$. The toroidal mode number n is related to the axial wavenumber k in the straight tokamak description via $n = R_0 k$. For ideal-MHD in a torus we still expect to find a slow and an Alfvén continuum, with spatially localised modes, as well as a discrete spectrum of CAEs with a cluster point at infinity [23, 25]. The main difference of concern for this thesis is that a new class of discrete shear Alfvén modes appears, the so-called *gap modes*. These modes exist in 'gaps' in the continuum that are opened up by the interaction of Alfvén continuum modes with different poloidal wavenumbers. In particular, Alfvén continuum modes follow the dispersion relation (1.158) and in a torus the parallel wavenumber is approximately:

$$k_\parallel = \frac{1}{R}\left(n + \frac{m}{q}\right) \ . \tag{1.166}$$

Therefore, there may exist in a tokamak two counter-propagating continuum mode with different poloidal mode numbers, say $\omega_m = k_{\parallel,m} V_A$ and $\omega_{m+1} = -k_{\parallel,m+1} V_A$. If there exists a point in the plasma such that $q = -(m + \frac{1}{2})/n$ then the counter-propagating waves will interfere destructively to produce a frequency gap in the continuum around that spatial location. A discrete shear Alfvén mode may then exist with a frequency that is constrained by the frequency gap. The reason that gap modes are present in a torus but not in a cylinder is that, unlike in a cylinder which is poloidally symmetric, there exists a mechanism in a torus for modes with different poloidal mode numbers to interact. Toroidicity allows a coupling between m and $m \pm 1$ modes. Shaping effects such as ellipticity and triangularity, and properties

of the equilibrium such as finite plasma-β all facilitate particular poloidal mode couplings and each have a type of gap mode named after them. Heidbrink [27] provides a good overview of the main types of gap mode.

1.7 CAEs in Tokamaks

In order to observe Compressional Alfvén eigenmodes, and other normal modes of the plasma, they must be driven by a source of free-energy in the plasma. In the case of CAEs the source of free-energy is a fast-ion population with a positive velocity gradient, such as fusion born alpha-particles or NBI ions. These fast-ions exchange energy with CAEs via the *ion cyclotron resonance* - see Section 1.8. The resonance condition can be written [28, 29]:

$$\omega = l\omega_{ci} + k_{\parallel}v_{\parallel} + k_{\perp}v_D \ , \tag{1.167}$$

where l is an integer. This condition is only expected to be satisfied by waves with frequencies on the order of the ion cyclotron frequency, ω_{ci}. CAEs are predicted to exist with frequencies on the order of ω_{ci} unlike the slow-magnetoacoustic and shear Alfvén modes which are generally predicted to have much lower frequencies. Therefore, CAEs are central to the current interpretation of electromagnetic emission in the ion cyclotron frequency range, *ion cyclotron emission* (ICE), that has been observed from a range of conventional tokamak devices [30–33]. Another candidate for ICE is the *Global Alfvén eigenmode* (GAE), a type of discrete shear Alfvén mode.

CAEs have also been observed directly in spherical tokamak devices such as MAST [2] and NSTX [28]. CAEs are easily excited by fast-ions in ST devices as they typically have a lower equilibrium magnetic field strength than a conventional tokamak, meaning a lower ion cyclotron frequency. MAST and NSTX both have NBI heating capable of accelerating a beam of particles to a velocity higher than the Alfvén velocity of the bulk plasma - this provides a fast-ion source for driving the CAEs. The CAEs are measured using an array of magnetic pickup coils that measure magnetic fluctuations above the surface of the bulk plasma. The magnetic activity is identified as CAEs by comparison with CAE theory, in particular the expected spatial structure of CAEs and the spectral structure. For example, the frequency difference between bands of CAE activity matches that expected for eigenmodes of different modes numbers, with three scales of frequency difference for the radial, poloidal and toroidal mode numbers. Fig. 1.4 shows an example of CAE modes identified during a MAST pulse. Modes are labelled with their toroidal mode number, which can be determined as there are several magnetic pickup coils located

at different toroidal angles on the outboard side of the tokamak [2, 34]. Modes with consecutive toroidal mode numbers are separated by a frequency gap on the order of $\sim$ 10 kHz, with two clear bands of mode activity separated by a frequency gap around 150 MHz. Since modes with the same n appear in each band it is predicted that the two bands contain modes with different poloidal mode numbers, say m and $m+1$. This is supported by predictions of the frequency gap for modes with consecutive poloidal mode numbers from CAE analytical and numerical models. The poloidal and radial mode numbers of the CAEs cannot be measured on MAST as the current configuration of magnetic pickup coils cannot measure in different poloidal or radial positions.

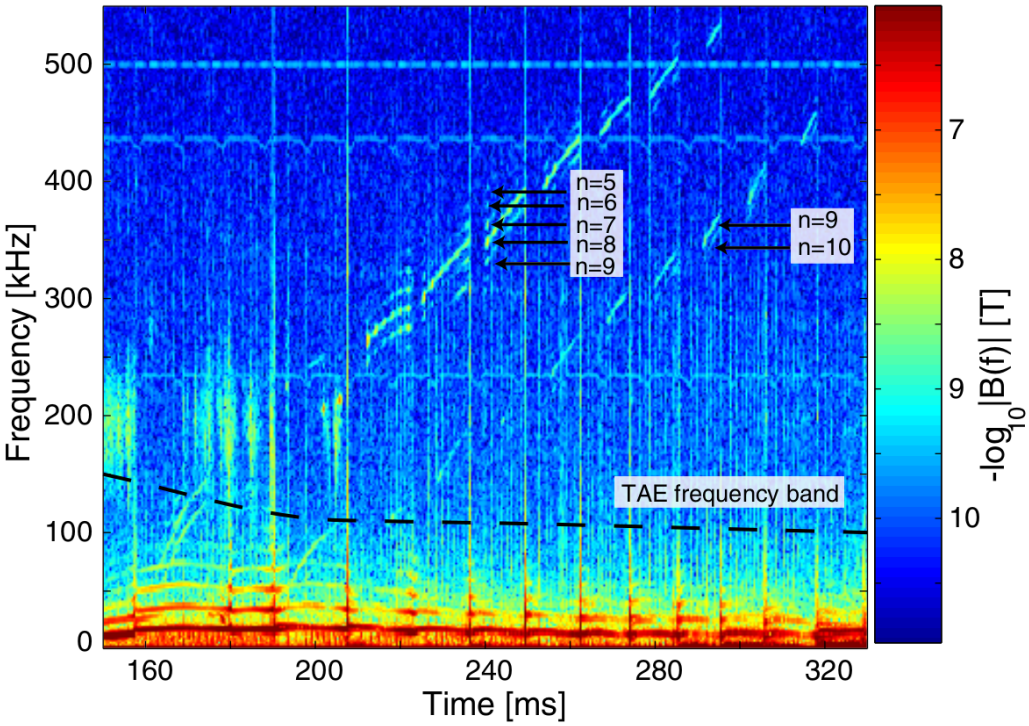

Figure 1.4: CAEs measured during a MAST pulse. There are two visible bands of CAEs and the toroidal mode number of each mode is labelled. Image reproduced from [2].

1.8 Anomalous Transport

Particle transport is an important area of research for fusion power plant operation as the energy confinement time, τ_E, forms part of the triple product, Eq. (1.9), and so it is important to understand the transport processes that influence it. *Classi-*

cal transport theory offers a first estimate by describing the particle transport due to Coulomb collisions in a plasma cylinder. *Neoclassical transport* extends this to include the more complex magnetic geometries of a plasma torus, which allows for particle drifts such as the ∇B-drift. Neoclassical transport makes predictions that are significantly closer to the measured values of particle transport than those of classical transport theory. However neoclassical theory is still limited in its applicability, leading to measurements that are up to two orders of magnitudes larger than the neoclassical prediction [1, 9]. The difference between the measured values and the predictions of neoclassical theory is termed *anomalous transport*. A major contributor to anomalous transport are *plasma instabilities*, in which a perturbation of the plasma equilibrium grows and pushes the plasma away from its equilibrium state.

In this thesis we are concerned with a wave-particle resonance, the *ion cyclotron instability*, which can affect shear Alfvén eigenmodes and CAEs. Discrete shear Alfvén modes, specifically *toroidal Alfvén eigenmodes* (TAEs), have been observed scattering fast-ions from NBI onto the vacuum vessel wall which can lead to structural damage and remove heat from the plasma which degrades the tokamak efficiency [35]. Conversely, the prospect of *alpha channeling* provides hope that plasma phenomena can be harnessed to enhance efficiency [36]. Alpha channeling refers to waves that are deliberately excited in the plasma via an antenna in order to harness a specific resonance with the fast-ions which redistributes their energy to the core of the bulk plasma.

Ion cyclotron resonance

Electric fields accelerate charged particles via the Lorentz force, exchanging energy with the particles. This happens most effectively when particles are in resonance with the electric field. Consider an electric plane-wave with the form $\mathbf{E} = E_y \cos(kx - \omega t + \phi)\hat{y}$ where ϕ is the phase of the wave relative to (x, t). Taking (x, t) to be the position of the particle, the particle experiences the largest sustained electric field when the relative phase is stationary in time and is an integer multiple of π. This results in maximal energy transfer. This is *Landau resonance* and the resonance condition is that the particle is in phase with the wave initially and travels with the phase velocity $v = \omega/k$ in the direction of the wave propagation, i.e. $\hat{x}$.

In a magnetised plasma charged particles travel helically around the magnetic field lines, gyrating at their cyclotron frequency. A resonance occurs with circularly polarised waves when the particle is in phase with the wave crest. We let the particles

have velocity $\boldsymbol{v}$ and $\boldsymbol{k}$ is the wavevector. The resonance condition is then:

$$\omega - k_{\parallel} v_{\parallel} - l\omega_c = 0 \ , \tag{1.168}$$

where $l = \pm 1$ refers to the *Doppler shifted cyclotron resonance* and *anomalous Doppler shifted cyclotron resonance* respectively. The case $l = 0$ is the Landau resonance described above. Suppose the particle and wave are co-propagating in the parallel direction so that $k_{\parallel} v_{\parallel} > 0$. The $k_{\parallel} v_{\parallel}$ term Doppler shifts the wave's frequency, so that $\omega - k_{\parallel} v_{\parallel}$ is the wave frequency from the particle's guiding centre frame of reference. Therefore this frequency should match the gyration frequency of the particle, with a sign modification depending on whether the handedness of the wave is the same or opposite to the particle. For $|l| > 1$ it is necessary for wave's electric field to vary in space, particularly on the spatial scale of the particle's Larmor radius [37, 38]. These resonances are usually weaker than the fundamental resonance. It is clear that Eq. (1.168) is a necessary condition for the wave-particle cyclotron resonance to occur, but it is not sufficient - we also need information about the polarisation of the wave and the particle, as well as direction of travel. Therefore, to model the resonance one must have detailed spatial information about the wave and the particle orbit.

We note that Eq. (1.168) assumes all of the perpendicular motion of the resonant particle to the magnetic field is cyclotron motion. A modified resonance condition incorporates the particles' drift velocities:

$$\omega - k_{\parallel} v_{\parallel} - \mathbf{k}_{\perp} \cdot \mathbf{v}_D - l\omega_c = 0 \ . \tag{1.169}$$

Of course, further corrections can be incorporated to account for more detailed particle motion.

1.9 Chapter Summary

In this chapter we have set out the case for studying the MHD compressional Alfvén eigenmodes as a means to further understanding one aspect of particle and energy transport in a plasma. We have established that we need to solve the linearised ideal Hall-MHD equations for both the eigenfrequency and eigenfunction, which gives the spatial structure of the CAE. We have established that Hall-MHD theory gives valid description of plasma waves for the frequency regime in which we are interested. We have also given an overview of the cylindrical and toroidal geometries in which we are interested, and introduced the equations that determine the equilibrium state

of the background plasma under certain conditions. The remainder of this thesis demonstrates how we built and tested the MHD linear stability code Whales2 and is arranged as follows.

Chapter 2 shows the rearrangement of the linearised Hall-MHD equations into a form suitable for the application of numerical methods, describes the particular geometry and co-ordinate system employed in Whales2, and derives the boundary conditions for a plasma cylinder/torus surrounded by a solid wall. Chapter 3 describes the numerical methods of Whales2 used to discetise the linearised Hall-MHD equations, the schemes employed to suppress unwanted physical and numerical behaviours, and demonstrates the self-adjointness of the discretised linear ideal-MHD equations in Whales2. Chapters 4 & 5 compare the numerical output of Whales2 against analytical and qualitative behaviour expected from CAE theory in cylindrical and toroidal geometries respectively.

Chapter 2

Theory

2.1 Linearized MHD Equations

To move the MHD equations into the final form to be solved, we start from the linearised Hall-MHD equations (1.68) - (1.74). We combine the linearised Faraday's law (1.71) with Ohm's law (1.73) to give the *induction equation*, and also rearrange the energy equation (1.70) using the mass equation (1.68). This produces the following set of linear equations:

$$\frac{\partial \rho_1}{\partial t} + \boldsymbol{\nabla} \cdot (\rho_0 \mathbf{v}_1) = 0 \ , \tag{2.1}$$

$$\rho_0 \frac{\partial \mathbf{v}_1}{\partial t} = \mathbf{J}_0 \times \mathbf{B}_1 + \mathbf{J}_1 \times \mathbf{B}_0 - \nabla p_1 \ , \tag{2.2}$$

$$\frac{\partial p_1}{\partial t} + \mathbf{v}_1 \cdot \boldsymbol{\nabla} p_0 + \gamma p_0 \boldsymbol{\nabla} \cdot \mathbf{v}_1 = 0 \ , \tag{2.3}$$

$$\begin{aligned} \frac{\partial \mathbf{B}_1}{\partial t} = \boldsymbol{\nabla} \times \Bigg[& \mathbf{v}_1 \times \mathbf{B}_0 + \frac{1}{en_0} \mathbf{J}_1 \times \mathbf{B}_0 + \frac{1}{en_0} \mathbf{J}_0 \times \mathbf{B}_1 \\ & - \frac{n_1}{en_0^2} \mathbf{J}_0 \times \mathbf{B}_0 - \frac{1}{en_0} \nabla p_{e1} + \frac{n_1}{en_0^2} \nabla p_{e0} \Bigg] \ , \end{aligned} \tag{2.4}$$

$$\boldsymbol{\nabla} \times \mathbf{B}_1 = \mu_0 \mathbf{J}_1 \ , \tag{2.5}$$

$$\boldsymbol{\nabla} \cdot \mathbf{B}_1 = 0 \ . \tag{2.6}$$

We then treat the Hall and battery terms as negligible to obtain the linearised ideal-MHD equations. We also substitute Ampère's law (2.5) into (2.2), giving:

$$\frac{\partial \rho_1}{\partial t} + \boldsymbol{\nabla} \cdot (\rho_0 \mathbf{v}_1) = 0 \ , \tag{2.7}$$

$$\mu_0 \rho_0 \frac{\partial \mathbf{v}_1}{\partial t} = (\boldsymbol{\nabla} \times \mathbf{B}_0) \times \mathbf{B}_1 + (\boldsymbol{\nabla} \times \mathbf{B}_1) \times \mathbf{B}_0 - \mu_0 \nabla p_1 \ , \tag{2.8}$$

$$\frac{\partial \mathbf{B}_1}{\partial t} = \boldsymbol{\nabla} \times (\mathbf{v}_1 \times \mathbf{B}_0) \ , \tag{2.9}$$

$$\frac{\partial p_1}{\partial t} + \mathbf{v}_1 \cdot \boldsymbol{\nabla} p_0 + \gamma p_0 \boldsymbol{\nabla} \cdot \mathbf{v}_1 = 0 \ , \tag{2.10}$$

$$\boldsymbol{\nabla} \cdot \mathbf{B}_1 = 0 \ . \tag{2.11}$$

It can be seen that in the absence of a steady flow, gravity or dissipative terms, the evolution of the density perturbation is described solely by the mass equation and so may be solved for after the other variables are determined. In order to eliminate some time derivatives we change variables $\mathbf{v} \to \boldsymbol{\xi}$ where $\boldsymbol{\xi}$ is the *plasma displacement*, i.e. the distance of a fluid element between its current position and the equilibrium position. The plasma velocity is then the Lagrangian derivative [26] $\mathbf{v} = \frac{\partial \boldsymbol{\xi}}{\partial t} + \mathbf{v} \cdot \boldsymbol{\nabla} \boldsymbol{\xi}$. The linearisation is carried out about an equilibrium position that is assumed static and flow-free (Section 1.5.3), therefore $\mathbf{v}_1 = \frac{\partial \boldsymbol{\xi}_1}{\partial t}$. For brevity we denote $\boldsymbol{\xi}_1 = \boldsymbol{\xi}$. The linearised ideal-MHD equations are thus:

$$\rho_1 + \boldsymbol{\nabla} \cdot (\rho_0 \boldsymbol{\xi}) = 0 \ , \tag{2.12}$$

$$\mu_0 \rho_0 \frac{\partial^2 \boldsymbol{\xi}}{\partial t^2} = (\boldsymbol{\nabla} \times \mathbf{B}_0) \times \mathbf{B}_1 + (\boldsymbol{\nabla} \times \mathbf{B}_1) \times \mathbf{B}_0 - \mu_0 \nabla p_1 \ , \tag{2.13}$$

$$\mathbf{B}_1 = \boldsymbol{\nabla} \times (\boldsymbol{\xi} \times \mathbf{B}_0) \ , \tag{2.14}$$

$$p_1 + \boldsymbol{\xi} \cdot \boldsymbol{\nabla} p_0 + \gamma p_0 \boldsymbol{\nabla} \cdot \boldsymbol{\xi} = 0 \ . \tag{2.15}$$

The condition $\boldsymbol{\nabla} \cdot \mathbf{B}_1 = 0$ is unnecessary as Eq. (2.14) implies the condition is satisfied. We transform these equations to a form to solve for $\boldsymbol{\xi}$ by substituting the induction and energy equations into the linearised momentum equation. This produces an equation of the form:

$$\mu_0 \rho_0 \frac{\partial^2 \boldsymbol{\xi}}{\partial t^2} = F(\boldsymbol{\xi}) \ , \tag{2.16}$$

which is analogous to Newton's second law. We broadly follow the work in [39] to achieve this rearrangement. We employ projections for $\boldsymbol{\xi}$ and $\mathbf{B}_1$ following the vectors:

$$\boldsymbol{\nabla} \psi \quad , \quad \mathbf{B}_0 \quad , \quad \mathbf{T} = \frac{\mathbf{B}_0 \times \boldsymbol{\nabla} \boldsymbol{\psi}}{|\boldsymbol{\nabla} \boldsymbol{\psi}|^2} \ . \tag{2.17}$$

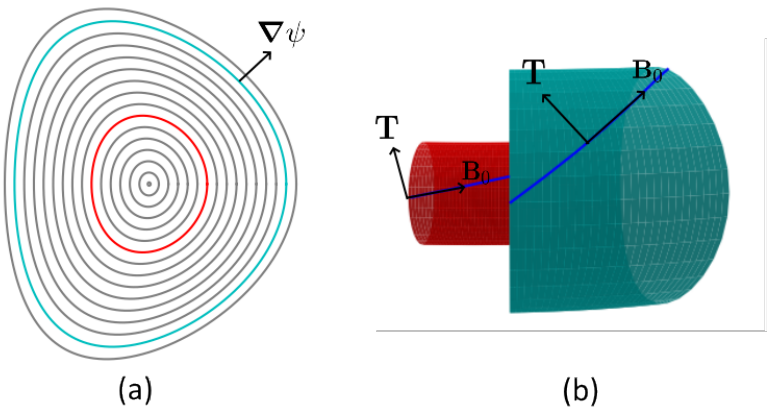

Figure 2.1: The left figure, (a), shows a poloidal cross-section of a typical tokamak geometry showing the nested flux surfaces concentric on the magnetic axis. The radial direction is given by the gradient of the flux function, which is illustrated for one point on an example surface. The right figure, (b), extends two example surfaces in the toroidal direction and gives a side-on view. An example equilibrium magnetic field line is depicted by a solid line in the surface. The directions given by the equilibrium magnetic field and the binormal are then highlighted at one point on each surface. Note that these directions change depending both on the position on a particular flux surface, as well as the particular flux surface.

These vectors are the gradient of the flux function (i.e. the normal to the flux surfaces), the equilibrium magnetic field direction, and the so-called *binormal* respectively, examples of which are shown in Fig. 2.1. Projecting the displacement and perturbed magnetic field onto these vectors gives:

$$\boldsymbol{\xi} = \xi_\perp \frac{\boldsymbol{\nabla\psi}}{|\boldsymbol{\nabla\psi}|^2} + \xi_\wedge \frac{\mathbf{B}_0 \times \boldsymbol{\nabla\psi}}{B_0^2} + \xi_\parallel \frac{\mathbf{B}_0}{B_0^2} \ , \tag{2.18}$$

$$\boldsymbol{B}_1 = b_\perp \frac{\boldsymbol{\nabla\psi}}{|\boldsymbol{\nabla\psi}|^2} + b_\wedge \frac{\mathbf{B}_0 \times \boldsymbol{\nabla\psi}}{|\boldsymbol{\nabla\psi}|^2} + b_\parallel \frac{\mathbf{B}_0}{B_0^2} \ . \tag{2.19}$$

This projection, which may be called the "Stix frame" [40,41], naturally follows some important directions in the plasma. $\boldsymbol{\nabla}\psi$ defines the most natural radial co-ordinate from the magnetic axis to the outer wall, following the direction normal to the magnetic surfaces. The equilibrium magnetic field introduces a preferential direction for the shear Alfvén and slow waves to propagate along. The binormal describes a direction that is within each particular flux surface but orthogonal to the local equilibrium magnetic field. It should be noted that these perturbed components don't have the dimensions of either displacement or magnetic field respectively, but are affected by the dimension of the direction vectors which are themselves not dimensionless. $\boldsymbol{\nabla}\psi$ has the dimension $[\boldsymbol{\nabla}\psi] = BL$ where B denotes the dimension of magnetic field and L the dimension of length, and so $\xi_\perp$ and $b_\perp$ have the dimensions BL^2 and B^2L respectively. Similarly, $\xi_\parallel$ and $b_\parallel$ have dimensions BL and B^2 while

$b_\wedge$ has dimension BL and $\xi_\wedge$ is dimensionless. Therefore, when calculating these components of the displacement it must be remembered that they do not have the dimensions of displacement (i.e. length) and must be appropriately normalised to recover the physical displacement. Also, directional derivatives in the directions of the vectors (2.17) do not simply have dimension L^{-1}.

We define the *linearised total pressure perturbation* (or just 'total pressure' when this is unambiguous) to be the sum of the linear parts of the kinetic pressure and the magnetic pressure perturbations:

$$p_T = p_1 + \frac{\mathbf{B}_0 \cdot \mathbf{B}_1}{\mu_0} \ . \tag{2.20}$$

We also express some geometric quantities :

$$S = \mathbf{T} \cdot \boldsymbol{\nabla} \times \mathbf{T} \ , \tag{2.21}$$

$$\boldsymbol{\kappa} = (\mathbf{b}_0 \cdot \boldsymbol{\nabla})\mathbf{b}_0 = (\boldsymbol{\nabla} \times \mathbf{b}_0) \times \mathbf{b}_0 \quad , \quad \mathbf{b}_0 = \frac{\mathbf{B}_0}{B_0} \ . \tag{2.22}$$

The quantity S is the *negative local shear* which measures the differential torsion of the magnetic field [42]. In an axisymmetric geometry the torsion must be constant toroidally and so the shear describes how the magnetic field differentially twists when looking over the radial direction. This shear is therefore related to the radial derivative of the safety function.

$\boldsymbol{\kappa}$ is the curvature of the magnetic field lines. This is inversely related to the radius of curvature and defined to be in the opposite direction, so that if $\boldsymbol{R}_c$ is the radius of curvature then:

$$\boldsymbol{\kappa} = -\frac{\boldsymbol{R}_c}{R_c^2} \ . \tag{2.23}$$

The component of the curvature in the radial direction is called the *normal curvature*, whilst the component in the binormal direction is the *geodesic curvature* [42]. One would expect that the curvature is proportional to the magnetic tension force, which acts to resist the bending of the magnetic field lines, and this can be seen by analysing the equilibrium Lorentz force.

$$\begin{aligned}(\boldsymbol{\nabla} \times \mathbf{B}_0) \times \mathbf{B}_0 =& B_0(\boldsymbol{\nabla} B_0 \times \mathbf{b}_0) \times \mathbf{b}_0 + B_0^2(\boldsymbol{\nabla} \times \mathbf{b}_0) \times \mathbf{b}_0 \\ =& B_0(\boldsymbol{\nabla} B_0 \cdot \mathbf{b}_0)\mathbf{b}_0 - B_0 \boldsymbol{\nabla} B_0 + B_0^2 \boldsymbol{\kappa} \\ =& B_0^2 \boldsymbol{\kappa} - B_0 \boldsymbol{\nabla}_\perp B_0 \ .\end{aligned} \tag{2.24}$$

If we compare this with Eq. (1.77) $(\boldsymbol{\nabla} \times \mathbf{B}_0) \times \mathbf{B}_0 = (\mathbf{B}_0 \cdot \boldsymbol{\nabla}\mathbf{B}_0)_\perp - B_0 \boldsymbol{\nabla}_\perp B_0$ then the connection between magnetic tension and curvature is clear.

We also have the radial derivative of the equilibrium pressure (since pressure is a flux function it only varies in this direction):

$$p_0' = \frac{\boldsymbol{\nabla\psi}\cdot\boldsymbol{\nabla}p_0}{|\boldsymbol{\nabla\psi}|^2} \ . \tag{2.25}$$

We start from the momentum equation and rewrite in terms of the total pressure:

$$\mu_0\rho_0\frac{\partial^2\boldsymbol{\xi}}{\partial t^2} \ = \ -\mu_0\boldsymbol{\nabla}p_T + \boldsymbol{\nabla}b_\parallel + (\boldsymbol{\nabla}\times\boldsymbol{B}_1)\times\boldsymbol{B}_0 + (\boldsymbol{\nabla}\times\boldsymbol{B}_0)\times\boldsymbol{B}_1 \ . \tag{2.26}$$

To resolve the cross-products we use the relations:

$$\boldsymbol{\nabla}\times\left(\frac{\boldsymbol{B}_0}{B_0^2}\right)\times\boldsymbol{B}_0 + (\boldsymbol{\nabla}\times\boldsymbol{B}_0)\times\left(\frac{\boldsymbol{B}_0}{B_0^2}\right) \ = \ 2\boldsymbol{\kappa} \ , \tag{2.27}$$

$$\boldsymbol{\nabla}b_\parallel + \left[\boldsymbol{\nabla}b_\parallel\times\left(\frac{\boldsymbol{B}_0}{B_0^2}\right)\right]\times\boldsymbol{B}_0 \ = \ \frac{\boldsymbol{B}_0}{B_0^2}\,(\boldsymbol{B}_0\cdot\boldsymbol{\nabla})b_\parallel \ , \tag{2.28}$$

$$\left[\boldsymbol{\nabla}\left(\frac{b_\perp}{|\boldsymbol{\nabla}\psi|^2}\right)\times\boldsymbol{\nabla}\psi\right]\times\boldsymbol{B}_0 \ = \ (\boldsymbol{B}_0\cdot\boldsymbol{\nabla})\left(\frac{b_\perp}{|\boldsymbol{\nabla}\psi|^2}\right)\boldsymbol{\nabla}\psi \ , \tag{2.29}$$

$$[\boldsymbol{\nabla}b_\wedge\times\boldsymbol{T}]\times\boldsymbol{B}_0 \ = \ \boldsymbol{T}\,(\boldsymbol{B}_0\cdot\boldsymbol{\nabla})b_\wedge \ , \tag{2.30}$$

which gives

$$\begin{aligned}\mu_0\rho_0\frac{\partial^2\boldsymbol{\xi}}{\partial t^2} = &-\mu_0\boldsymbol{\nabla}p_T \\ &+ (\boldsymbol{B}_0\cdot\boldsymbol{\nabla})\left(\frac{b_\perp}{|\boldsymbol{\nabla}\psi|^2}\right)\boldsymbol{\nabla}\psi + \mu_0(\boldsymbol{J}_0\times\boldsymbol{\nabla}\psi)\,\frac{b_\perp}{|\boldsymbol{\nabla}\psi|^2} \\ &+ \boldsymbol{T}\,(\boldsymbol{B}_0\cdot\boldsymbol{\nabla})b_\wedge + (\boldsymbol{\nabla}\times\boldsymbol{T})\times\boldsymbol{B}_0\,b_\wedge + \mu_0(\boldsymbol{J}_0\times\boldsymbol{T})\,b_\wedge \\ &+ \frac{\boldsymbol{B}_0}{B_0^2}\,(\boldsymbol{B}_0\cdot\boldsymbol{\nabla})b_\parallel + 2\boldsymbol{\kappa}\,b_\parallel \ .\end{aligned} \tag{2.31}$$

We now examine the individual components of the momentum equations. We start with the perpendicular component by projecting Eq. (2.31) on $\boldsymbol{\nabla}\psi$:

$$\begin{aligned}\mu_0\rho_0\frac{\partial^2\xi_\perp}{\partial t^2} \ = &-\mu_0\boldsymbol{\nabla}\psi\cdot\boldsymbol{\nabla}p_T + |\boldsymbol{\nabla}\psi|^2\,(\boldsymbol{B}_0.\boldsymbol{\nabla})\left(\frac{b_\perp}{|\boldsymbol{\nabla}\psi|^2}\right) \\ &+ \left(|\boldsymbol{\nabla}\psi|^2 S - \mu_0\boldsymbol{J}_0\cdot\boldsymbol{B}_0\right)\,b_\wedge + (2\boldsymbol{\nabla}\psi\cdot\boldsymbol{\kappa})\,b_\parallel \ ,\end{aligned} \tag{2.32}$$

where we used

$$[(\boldsymbol{\nabla}\times\boldsymbol{T})\times\boldsymbol{B}_0]\cdot\boldsymbol{\nabla}\psi \ = \ |\boldsymbol{\nabla}\psi|^2 S \ , \tag{2.33}$$

$$(\boldsymbol{J}_0\times\boldsymbol{T})\cdot\boldsymbol{\nabla}\psi \ = \ -\boldsymbol{J}_0\cdot\boldsymbol{B}_0 \ . \tag{2.34}$$

To obtain the wedge component of the momentum equation, we further establish the relation:

$$[(\boldsymbol{\nabla} \times \boldsymbol{T}) \times \boldsymbol{B}_0] \cdot \boldsymbol{T} \;=\; -\frac{B_0^2}{|\boldsymbol{\nabla}\psi|^2}\,\boldsymbol{\nabla}\psi \cdot (\boldsymbol{\nabla} \times \boldsymbol{T}) \;=\; 0 \quad , \tag{2.35}$$

and explicitly write out the geodesic curvature in terms of the equilibrium magnetic field and flux:

$$\begin{aligned}\boldsymbol{\kappa}.\boldsymbol{T} &= -\frac{B_0}{|\boldsymbol{\nabla}\psi|^2}\boldsymbol{\nabla}\psi \cdot (\boldsymbol{\nabla} \times \boldsymbol{b}_0) \;=\; -\frac{B_0}{|\boldsymbol{\nabla}\psi|^2}\boldsymbol{\nabla}\psi \cdot \left(\boldsymbol{\nabla} B_0^{-1} \times \boldsymbol{B}_0\right) \\ &= -\frac{B_0^2}{2|\boldsymbol{\nabla}\psi|^2}\boldsymbol{\nabla}\psi \cdot \left(\boldsymbol{\nabla} B_0^{-2} \times \boldsymbol{B}_0\right) \;=\; -\frac{B_0^2}{2|\boldsymbol{\nabla}\psi|^2}\,\boldsymbol{\nabla} \cdot \left(\frac{\boldsymbol{B}_0 \times \boldsymbol{\nabla}\psi}{B_0^2}\right) \quad .\end{aligned} \tag{2.36}$$

This gives the wedge component as:

$$\begin{aligned}\mu_0\rho_0\frac{\partial^2\xi_\wedge}{\partial t^2} \;&=\; -\,\mu_0\boldsymbol{T}\cdot\boldsymbol{\nabla}p_T + \mu_0\frac{\boldsymbol{J}_0\cdot\boldsymbol{B}_0}{|\boldsymbol{\nabla}\psi|^2}\,b_\perp + \frac{B_0^2}{|\boldsymbol{\nabla}\psi|^2}(\boldsymbol{B}_0\cdot\boldsymbol{\nabla})b_\wedge \\ &\quad - \frac{B_0^2}{|\boldsymbol{\nabla}\psi|^2}\,\boldsymbol{\nabla}\cdot\left(\frac{\boldsymbol{B}_0\times\boldsymbol{\nabla}\psi}{B_0^2}\right)\,b_\parallel \;.\end{aligned} \tag{2.37}$$

For the parallel component of the momentum equation we look back to Eq. (2.13) to determine:

$$\mu_0\rho_0\frac{\partial^2\xi_\parallel}{\partial t^2} \;=\; -\mu_0\boldsymbol{B}_0\cdot\boldsymbol{\nabla}p_1 - \mu_0(\boldsymbol{J}_0\times\boldsymbol{B}_0)\cdot\boldsymbol{B}_1 \;. \tag{2.38}$$

Recalling that in our equilibrium $\boldsymbol{J}_0 \times \boldsymbol{B}_0 = \boldsymbol{\nabla}p_0$ and that p_0 is a flux function, so $\boldsymbol{\nabla}p_0 \sim \boldsymbol{\nabla}\psi$ then we have:

$$\mu_0\rho_0\frac{\partial^2\xi_\parallel}{\partial t^2} \;=\; -(\boldsymbol{B}_0\cdot\boldsymbol{\nabla})\mu_0 p_1 - \mu_0 p_0' b_\perp \;. \tag{2.39}$$

We don't write this equation in terms of the total pressure as we will be solving the wave equations in the zero plasma-β limit, where the parallel displacement will be shown to be absent.

We eliminate the magnetic field perturbation in favour of the displacement by examining the linearised induction equation Eq. (2.14). The three components

of $\boldsymbol{B}_1$ can be written as follows, starting with the perpendicular component:

$$\begin{aligned} b_\perp &= \boldsymbol{B}_1 \cdot \boldsymbol{\nabla}\psi \\ &= [\boldsymbol{\nabla} \times (\boldsymbol{\xi}_\perp \times \boldsymbol{B}_0)] \cdot \boldsymbol{\nabla}\psi \\ &= \boldsymbol{\nabla} \cdot [(\boldsymbol{\xi}_\perp \times \boldsymbol{B}_0) \times \boldsymbol{\nabla}\psi] \\ &= \boldsymbol{\nabla} \cdot (\xi_\perp \boldsymbol{B}_0) \\ &= (\boldsymbol{B}_0 \cdot \boldsymbol{\nabla})\, \xi_\perp \ . \end{aligned} \tag{2.40}$$

The wedge component is:

$$\begin{aligned} b_\wedge &= \boldsymbol{B}_1 \cdot \frac{\boldsymbol{B}_0 \times \boldsymbol{\nabla}\psi}{B_0^2} \\ &= \frac{|\boldsymbol{\nabla}\psi|^2}{B_0^2}\, [\boldsymbol{\nabla} \times (\boldsymbol{\xi}_\perp \times \boldsymbol{B}_0)] \cdot \boldsymbol{T} \\ &= \frac{|\boldsymbol{\nabla}\psi|^2}{B_0^2}\, \{\boldsymbol{\nabla} \cdot [(\boldsymbol{\xi}_\perp \times \boldsymbol{B}_0) \times \boldsymbol{T}] + (\boldsymbol{\xi}_\perp \times \boldsymbol{B}_0) \cdot \boldsymbol{\nabla} \times \boldsymbol{T}\} \\ &= \frac{|\boldsymbol{\nabla}\psi|^2}{B_0^2}\, \{\boldsymbol{\nabla} \cdot [(\boldsymbol{\xi}_\perp \cdot \boldsymbol{T})\boldsymbol{B}_0] - \xi_\perp \boldsymbol{T} \cdot \boldsymbol{\nabla} \times \boldsymbol{T} + \xi_\wedge \boldsymbol{\nabla}\psi \cdot \boldsymbol{\nabla} \times \boldsymbol{T}\} \\ &= \frac{|\boldsymbol{\nabla}\psi|^2}{B_0^2}\, [(\boldsymbol{B}_0 \cdot \boldsymbol{\nabla})\, \xi_\wedge - S\xi_\perp] \ . \end{aligned} \tag{2.41}$$

Finally, the parallel component:

$$\begin{aligned} b_\parallel &= \boldsymbol{B}_1 \cdot \boldsymbol{B}_0 \\ &= [\boldsymbol{\nabla} \times (\boldsymbol{\xi}_\perp \times \boldsymbol{B}_0)] \cdot \boldsymbol{B}_0 \\ &= \boldsymbol{\nabla} \cdot [(\boldsymbol{\xi}_\perp \times \boldsymbol{B}_0) \times \boldsymbol{B}_0] + (\boldsymbol{\xi}_\perp \times \boldsymbol{B}_0) \cdot \boldsymbol{\nabla} \times \boldsymbol{B}_0 \\ &= -\boldsymbol{\nabla} \cdot (\boldsymbol{\xi}_\perp B_0^2) - \mu_0 (\boldsymbol{J}_0 \times \boldsymbol{B}_0) \cdot \boldsymbol{\xi}_\perp \\ &= -B_0^2 (\boldsymbol{\nabla} \cdot \boldsymbol{\xi}_\perp) - \left[\boldsymbol{\nabla} B_0^2 + \mu_0 (\boldsymbol{J}_0 \times \boldsymbol{B}_0)\right] \cdot \boldsymbol{\xi}_\perp \ . \end{aligned} \tag{2.42}$$

The final bracketed term of the parallel equation is a sum of the kinetic and magnetic pressures and so we expand out the Lorentz force term in terms of curvature as per (2.24). We can safely write $\boldsymbol{\nabla} B_0^2 \to \boldsymbol{\nabla}_\perp B_0^2$ as the subsequent scalar product is with the directions perpendicular to the equilibrium magnetic field direction. Therefore:

$$\boldsymbol{\nabla}_\perp B_0^2 + \mu_0 (\boldsymbol{J}_0 \times \boldsymbol{B}_0) = B_0 \boldsymbol{\nabla}_\perp B_0 + B_0^2 \boldsymbol{\kappa} \ . \tag{2.43}$$

Finally we use the energy equation to study p_T. Looking to Eq. (2.15) it is easy to

see

$$\mu_0 p_T = \mu_0 p_1 + b_\parallel = -\mu_0 \gamma p_0 \boldsymbol{\nabla} \cdot \boldsymbol{\xi} - \mu_0 p_0' \xi_\perp + b_\parallel \ . \tag{2.44}$$

Now we substitute in the components of $\boldsymbol{B}_1$ to leave the equations in terms of $\boldsymbol{\xi}$ and p_T. We start with the total pressure:

$$\begin{aligned}\mu_0 p_T = &- B_0^2 \left[\boldsymbol{\nabla} \cdot \left(\frac{\boldsymbol{\nabla}\psi}{|\boldsymbol{\nabla}\psi|^2} \xi_\perp \right) + \frac{(2\boldsymbol{\nabla}\psi \cdot \boldsymbol{\kappa})}{|\boldsymbol{\nabla}\psi|^2} \xi_\perp \right] \\ &- B_0^2 \left[\frac{\mathbf{B}_0 \times \boldsymbol{\nabla}\psi}{B_0^2} \cdot \frac{\boldsymbol{\nabla} B_0^2}{B_0^2} \xi_\wedge + \boldsymbol{\nabla} \cdot \left(\frac{\mathbf{B}_0 \times \boldsymbol{\nabla}\psi}{B_0^2} \xi_\wedge \right) \right] \\ &- \mu_0 \gamma p_0 \boldsymbol{\nabla} \cdot \boldsymbol{\xi} \ .\end{aligned} \tag{2.45}$$

Using another identity will put this expression in a form that can be understood physically. We start from $\mathbf{T} \cdot \boldsymbol{\nabla} p_0 = 0$ and we have from Eq. (2.24) that: $B_0^2 \mathbf{T} \cdot \boldsymbol{\kappa} = \mathbf{T} \cdot \boldsymbol{\nabla} B_0^2$. So the above becomes:

$$\begin{aligned}\mu_0 p_T = &- B_0^2 \left[\boldsymbol{\nabla} \cdot \left(\frac{\boldsymbol{\nabla}\psi}{|\boldsymbol{\nabla}\psi|^2} \xi_\perp \right) + 2\boldsymbol{\kappa} \cdot \frac{\boldsymbol{\nabla}\psi}{|\boldsymbol{\nabla}\psi|^2} \xi_\perp \right] \\ &- B_0^2 \left[\boldsymbol{\nabla} \cdot \left(\frac{\mathbf{B}_0 \times \boldsymbol{\nabla}\psi}{B_0^2} \xi_\wedge \right) + 2\boldsymbol{\kappa} \cdot \frac{\mathbf{B}_0 \times \boldsymbol{\nabla}\psi}{B_0^2} \xi_\wedge \right] \\ &- \mu_0 \gamma p_0 \boldsymbol{\nabla} \cdot \boldsymbol{\xi} \ .\end{aligned} \tag{2.46}$$

These terms are similar to those in common formulations of the *energy principle*, in which the MHD equations are cast as a perturbed potential energy to analyse the stability of a configuration. $|\mu_0 \gamma p_0 \boldsymbol{\nabla} \cdot \boldsymbol{\xi}|^2$ corresponds to the energy required to compress the plasma and so is associated with the Slow magnetoacoustic wave [19]. The first two lines of the total pressure expression above are analogous to $B_0^2 |\boldsymbol{\nabla} \cdot \boldsymbol{\xi}_\perp + 2\boldsymbol{\xi}_\perp \cdot \boldsymbol{\kappa}|^2$, which is the energy required to compress the magnetic field and so is associated with CAEs [19]. These terms mostly correspond to the contribution to the total pressure from the parallel component of the perturbed magnetic field, and this is expected as $b_\parallel$ is the dominant perturbed magnetic field component for CAEs [43]. Thus, as expected, the total pressure is important to both the Slow waves and CAEs but not the Shear Alfvén waves which have the restoring force of magnetic tension. Following the energy principle analogy, the Shear waves are associated with the two perpendicular components of the perturbed magnetic field as $|b_\perp + b_\wedge|^2$ is the energy required to bend magnetic field lines. The correspondence of each of these terms to the respective wave only holds strictly in the case of a homogeneous magnetic field, but the intuition gained from thinking of these correspondences is still useful in more complicated plasma setups.

Now writing the components of the plasma displacement:

$$\begin{aligned}\mu_0\rho_0\frac{\partial^2\xi_\perp}{\partial t^2} =& -\mu_0\boldsymbol{\nabla}\psi\cdot\boldsymbol{\nabla}p_T + (2\boldsymbol{\nabla}\psi\cdot\boldsymbol{\kappa})(\mu_0 p_T + \mu_0\gamma p_0\boldsymbol{\nabla}\cdot\boldsymbol{\xi}) \\ &+ \mu_0 p_0^{'}(2\boldsymbol{\nabla}\psi\cdot\boldsymbol{\kappa})\xi_\perp \\ &+ |\boldsymbol{\nabla}\psi|^2(\mathbf{B_0}\cdot\boldsymbol{\nabla})\left(\frac{(\boldsymbol{B_0}\cdot\boldsymbol{\nabla})\xi_\perp}{|\boldsymbol{\nabla}\psi|^2}\right) - \frac{|\boldsymbol{\nabla}\psi|^2}{B_0^2}(|\boldsymbol{\nabla}\psi|^2 S - \mu_0(\mathbf{J}_0\cdot\mathbf{B}_0))S\xi_\perp \\ &+ \frac{|\boldsymbol{\nabla}\psi|^2}{B_0^2}(|\boldsymbol{\nabla}\psi|^2 S - \mu_0(\mathbf{J}_0\cdot\mathbf{B}_0))(\mathbf{B_0}\cdot\boldsymbol{\nabla})\xi_\wedge\ , \end{aligned} \tag{2.47}$$

$$\begin{aligned}\mu_0\rho_0\frac{\partial^2\xi_\wedge}{\partial t^2} =& -\mu_0\boldsymbol{T}\cdot\boldsymbol{\nabla}p_T - \frac{B_0^2}{|\boldsymbol{\nabla}\psi|^2}\boldsymbol{\nabla}\cdot\left(\frac{\mathbf{B}_0\times\boldsymbol{\nabla}\psi}{B_0^2}\right)(\mu_0 p_T + \mu_0\gamma p_0\boldsymbol{\nabla}\cdot\boldsymbol{\xi}) \\ &- \frac{B_0^2}{|\boldsymbol{\nabla}\psi|^2}\boldsymbol{\nabla}\cdot\left(\frac{\mathbf{B}_0\times\boldsymbol{\nabla}\psi}{B_0^2}\right)\mu_0 p_0^{'}\xi_\perp \\ &- \frac{B_0^2}{|\boldsymbol{\nabla}\psi|^2}(\mathbf{B}_0\cdot\boldsymbol{\nabla})\left[\frac{|\boldsymbol{\nabla}\psi|^2}{B_0^2}S\xi_\perp\right] + \frac{\mu_0\mathbf{J}_0\cdot\mathbf{B}_0}{|\boldsymbol{\nabla}\psi|^2}(\mathbf{B_0}\cdot\boldsymbol{\nabla})\xi_\perp \\ &+ \frac{B_0^2}{|\boldsymbol{\nabla}\psi|^2}(\mathbf{B_0}\cdot\boldsymbol{\nabla})\left[\frac{|\boldsymbol{\nabla}\psi|^2}{B_0^2}(\mathbf{B_0}\cdot\boldsymbol{\nabla})\xi_\wedge\right]\ , \end{aligned} \tag{2.48}$$

$$\mu_0\rho_0\frac{\partial^2\xi_\parallel}{\partial t^2} = \mu_0\gamma p_0(\mathbf{B_0}\cdot\boldsymbol{\nabla})\boldsymbol{\nabla}\cdot\boldsymbol{\xi}\ . \tag{2.49}$$

So for the two perpendicular components of the displacement, the first three terms of the right hand side are primarily associated with magnetic field line and plasma compression, i.e. the terms involving p_0' and p_T. The last three terms, involving S and $(\mathbf{B_0}\cdot\boldsymbol{\nabla})$, describe field line bending.

The parallel displacement is correlated with the plasma pressure and so is an important displacement component for both the CAEs and slow waves. However, the CAEs are driven primarily by the magnetic pressure unlike the slow waves which are primarily driven by plasma pressure, and so to eliminate the slow waves from the MHD wave equation we assume that the plasma-β is negligible. This assumption of $\beta = 2\mu_0 p_0/B_0^2 \ll 1$ is equivalent to $\mu_0 p_0 \ll B_0^2$ so the plasma pressure is considered negligible in comparison to the magnetic terms. In the limit of zero plasma-β then it follows that $p_0 = 0$ and this is applied to the MHD wave equation. Clearly this forces $\xi_\parallel = 0$ and so we neglect the parallel displacement component.

2.2 Axisymmetric toroidal geometry

We apply an axisymmetric toroidal geometry to the equations. The geometry can be summarised as (ψ, ϕ, ϑ) where ψ is our 'radial' co-ordinate and ϑ is any poloidal angle, provided it creates a left-handed co-ordinate system. These two are orthogonal to the toroidal angle ϕ but not necessarily to each other. This is similar to the 'PEST co-ordinate system' (named after the early linear stability code) [44].

The metric tensor is:

$$\begin{bmatrix} g^{\psi\psi} & g^{\psi\phi} & g^{\psi\vartheta} \\ g^{\phi\psi} & g^{\phi\phi} & g^{\phi\vartheta} \\ g^{\vartheta\psi} & g^{\vartheta\phi} & g^{\vartheta\vartheta} \end{bmatrix} = \begin{bmatrix} \boldsymbol{\nabla}\psi \cdot \boldsymbol{\nabla}\psi & 0 & \boldsymbol{\nabla}\psi \cdot \boldsymbol{\nabla}\vartheta \\ 0 & \boldsymbol{\nabla}\phi \cdot \boldsymbol{\nabla}\phi & 0 \\ \boldsymbol{\nabla}\vartheta \cdot \boldsymbol{\nabla}\psi & 0 & \boldsymbol{\nabla}\vartheta \cdot \boldsymbol{\nabla}\vartheta \end{bmatrix} \tag{2.50}$$

The choice to implement this co-ordinate system on the equations, rather than the Stix frame that was used for the projection of the displacement and the magnetic field perturbation, was made to fully take advantage of the axisymmetry. Derivatives of equilibrium functions in one direction vanish automatically and four metric elements also vanish. The Jacobian, $\mathcal{J}$, can be expressed as [45] :

$$\mathcal{J} = \frac{1}{\boldsymbol{\nabla}\psi \cdot (\boldsymbol{\nabla}\phi \times \boldsymbol{\nabla}\vartheta)} = \frac{1}{\sqrt{(g^{\psi\psi} g^{\vartheta\vartheta} - g^{\psi\vartheta} g^{\vartheta\psi}) g^{\phi\phi}}} \ . \tag{2.51}$$

We denote the contravariant basis $(\boldsymbol{\nabla}\psi, \boldsymbol{\nabla}\phi, \boldsymbol{\nabla}\vartheta)$ and the covariant basis $(\boldsymbol{e}_\psi, \boldsymbol{e}_\phi, \boldsymbol{e}_\vartheta)$. We now demonstrate that the terms in Eq. (2.63) reading

$$\begin{aligned} &- \frac{B_0^2}{|\boldsymbol{\nabla}\psi|^2} \boldsymbol{\nabla} \cdot \left(\frac{\mathbf{B}_0 \times \boldsymbol{\nabla}\psi}{B_0^2} \right) \mu_0 p_0' \xi_\perp - \frac{B_0^2}{|\boldsymbol{\nabla}\psi|^2} (\mathbf{B}_0 \cdot \boldsymbol{\nabla}) \left[\frac{|\boldsymbol{\nabla}\psi|^2}{B_0^2} S \xi_\perp \right] \\ &+ \frac{\mu_0 \mathbf{J}_0 \cdot \mathbf{B}_0}{|\boldsymbol{\nabla}\psi|^2} (\mathbf{B_0} \cdot \boldsymbol{\nabla}) \xi_\perp \ , \end{aligned} \tag{2.52}$$

are equivalent to the expression

$$- \frac{B_0^2}{|\boldsymbol{\nabla}\psi|^2} (\mathbf{B}_0 \cdot \boldsymbol{\nabla}) \left[\frac{|\boldsymbol{\nabla}\psi|^2 S - \mu_0 \mathbf{J}_0 \cdot \mathbf{B}_0}{B_0^2} \xi_\perp \right] \ , \tag{2.53}$$

by showing that:

$$-\boldsymbol{\nabla} \cdot \left(\frac{\mathbf{B}_0 \times \boldsymbol{\nabla}\psi}{B_0^2} \right) p_0' = (\mathbf{B}_0 \cdot \boldsymbol{\nabla}) \frac{\mathbf{J}_0 \cdot \mathbf{B}_0}{B_0^2} \ . \tag{2.54}$$

To start we use the expression for the equilibrium magnetic field given in (1.82) in

the cross-product:

$$\begin{aligned}\mathbf{B}_0 \times \boldsymbol{\nabla}\psi &= f(\psi)\boldsymbol{\nabla}\phi \times \boldsymbol{\nabla}\psi + (\boldsymbol{\nabla}\psi \times \boldsymbol{\nabla}\phi) \times \boldsymbol{\nabla}\phi \\ &= f(\psi)\boldsymbol{\nabla}\phi \times \boldsymbol{\nabla}\psi + g^{\psi\psi}\boldsymbol{\nabla}\phi \ . \end{aligned} \tag{2.55}$$

Remembering the axisymmetry of the equilibrium, i.e. $\partial_\phi A_0 = 0$, we have:

$$\boldsymbol{\nabla} \cdot \left(\frac{\mathbf{B}_0 \times \boldsymbol{\nabla}\psi}{B_0^2} \right) = \frac{1}{\mathcal{J}} \partial_\vartheta \left(\frac{\boldsymbol{\nabla}\vartheta \cdot (\boldsymbol{\nabla}\phi \times \boldsymbol{\nabla}\psi)}{B_0^2} \mathcal{J} f(\psi) \right) = -\frac{f(\psi)}{\mathcal{J}} \partial_\vartheta \left(\frac{1}{B_0^2} \right) \ . \tag{2.56}$$

Because $(\mathbf{B}_0 \cdot \boldsymbol{\nabla}) = f(\psi) g^{\phi\phi} \partial_\phi + \frac{1}{\mathcal{J}} \partial_\vartheta$ and the axisymmetry of equilibrium quantities, Eq.(2.54) can be rewritten as:

$$\partial_\vartheta \left(\frac{\mathbf{J}_0 \cdot \mathbf{B}_0 - f(\psi) p_0'}{B_0^2} \right) = 0 \ . \tag{2.57}$$

We make use of Eqs. (1.75) and (2.25):

$$\begin{aligned} f(\psi) p_0' &= \frac{f(\psi)}{g^{\psi\psi}} \boldsymbol{\nabla}\psi \cdot (\mathbf{J}_0 \times \mathbf{B}_0) \\ &= \frac{f(\psi)}{g^{\psi\psi}} \mathbf{J}_0 \cdot (\mathbf{B}_0 \times \boldsymbol{\nabla}\psi) \\ &= \mathbf{J}_0 \cdot \left(f(\psi) \boldsymbol{\nabla}\phi + \frac{f^2(\psi)}{g^{\psi\psi}} \boldsymbol{\nabla}\phi \times \boldsymbol{\nabla}\psi \right) \ , \end{aligned} \tag{2.58}$$

to eliminate the plasma pressure gradient from Eq. (2.57). We also use the following relations:

$$(\boldsymbol{\nabla} \times \mathbf{B}_0) \cdot \boldsymbol{\nabla}\psi = \frac{1}{\mathcal{J}} (\partial_\phi B_\vartheta - \partial_\vartheta B_\phi) = 0 \ , \tag{2.59}$$

$$\begin{aligned} g_{\vartheta\vartheta} &= e_\vartheta \cdot e_\vartheta \\ &= \mathcal{J}^2 (\boldsymbol{\nabla}\psi \times \boldsymbol{\nabla}\phi) \cdot (\boldsymbol{\nabla}\psi \times \boldsymbol{\nabla}\phi) \\ &= \mathcal{J}^2 ((\boldsymbol{\nabla}\psi \cdot \boldsymbol{\nabla}\psi)(\boldsymbol{\nabla}\phi \cdot \boldsymbol{\nabla}\phi) - (\boldsymbol{\nabla}\psi \cdot \boldsymbol{\nabla}\phi)(\boldsymbol{\nabla}\phi \cdot \boldsymbol{\nabla}\psi)) \\ &= \mathcal{J}^2 g^{\psi\psi} g^{\phi\phi} \ , \end{aligned} \tag{2.60}$$

to rewrite the numerator of Eq. (2.57):

$$\begin{aligned}
\mathbf{J}_0 \cdot \mathbf{B}_0 - f(\psi)p_0' &= \mathbf{J}_0 \cdot (\boldsymbol{\nabla}\psi \times \boldsymbol{\nabla}\phi)\left(\frac{g^{\psi\psi} + f^2(\psi)}{g^{\psi\psi}}\right) \\
&= J_{0\vartheta}\boldsymbol{\nabla}\vartheta \cdot (\boldsymbol{\nabla}\psi \times \boldsymbol{\nabla}\phi)\frac{B_0^2}{g^{\psi\psi}g^{\phi\phi}} \\
&= J_{0\vartheta}\frac{B_0^2}{\mathcal{J}g^{\psi\psi}g^{\phi\phi}} \\
&= (\boldsymbol{\nabla} \times \mathbf{B}_0) \cdot \boldsymbol{e}_\vartheta \frac{B_0^2}{\mu_0\mathcal{J}g^{\psi\psi}g^{\phi\phi}} \\
&= (\boldsymbol{\nabla} \times \mathbf{B}_0) \cdot (g_{\vartheta\vartheta}\boldsymbol{\nabla}\vartheta + g_{\vartheta\psi}\boldsymbol{\nabla}\psi)\frac{B_0^2}{\mu_0\mathcal{J}g^{\psi\psi}g^{\phi\phi}} \\
&= \frac{g_{\vartheta\vartheta}}{\mathcal{J}}\partial_\psi f(\psi)\frac{B_0^2}{\mu_0\mathcal{J}g^{\psi\psi}g^{\phi\phi}} \\
&= \frac{B_0^2}{\mu_0}\partial_\psi f(\psi) \ . \qquad (2.61)
\end{aligned}$$

So finally we come to:

$$\partial_\vartheta\left(\frac{\mathbf{J}_0 \cdot \mathbf{B}_0 - f(\psi)p_0'}{B_0^2}\right) = \frac{1}{\mu_0}\partial_\vartheta\left(\partial_\psi f(\psi)\right) = 0 \ . \qquad (2.62)$$

Therefore since Eq. (2.57) is true then the original assertion, Eq. (2.54), is correct and so we rewrite our equation for $\xi_\wedge$:

$$\begin{aligned}
\mu_0\rho_0\frac{\partial^2\xi_\wedge}{\partial t^2} =& -\mu_0\boldsymbol{T} \cdot \boldsymbol{\nabla}p_T - \frac{B_0^2}{|\boldsymbol{\nabla}\psi|^2}\boldsymbol{\nabla} \cdot \left(\frac{\mathbf{B}_0 \times \boldsymbol{\nabla}\psi}{B_0^2}\right)(\mu_0 p_T + \mu_0\gamma p_0\boldsymbol{\nabla} \cdot \boldsymbol{\xi}) \\
&- \frac{B_0^2}{|\boldsymbol{\nabla}\psi|^2}(\mathbf{B_0} \cdot \boldsymbol{\nabla})\left[\frac{|\boldsymbol{\nabla}\psi|^2 S - \mu_0\mathbf{J}_0 \cdot \mathbf{B}_0}{B_0^2}\xi_\perp\right] \\
&+ \frac{B_0^2}{|\boldsymbol{\nabla}\psi|^2}(\mathbf{B_0} \cdot \boldsymbol{\nabla})\left[\frac{|\boldsymbol{\nabla}\psi|^2}{B_0^2}(\mathbf{B_0} \cdot \boldsymbol{\nabla})\xi_\wedge\right] \ . \qquad (2.63)
\end{aligned}$$

We now apply the geometry to obtain a final form of the linearised ideal MHD equations. For this, we make use of the following changes of variable:

$$\xi_\perp \to \tilde{\xi}_\perp = \mathcal{J}\xi_\perp \ , \qquad (2.64)$$

$$\xi_\wedge \to \tilde{\xi}_\wedge = \frac{|\boldsymbol{\nabla}\psi|}{B_0}\xi_\wedge \ . \qquad (2.65)$$

The first change of variable is made for convenience as factors of $\mathcal{J}\xi_\perp$ will appear inside radial derivatives. The second facilitates simpler boundary conditions (see Section 2.5). We apply these substitutions in the zero plasma-β limit to Eq. (2.46)

for the total pressure perturbation:

$$\mu_0 p_T = -\frac{B_0^2}{\mathcal{J}}\partial_\psi \tilde{\xi}_\perp - \frac{B_0^2}{\mathcal{J}}\partial_\vartheta\left(\frac{g^{\psi\vartheta}}{g^{\psi\psi}}\tilde{\xi}_\perp\right) - \frac{(2\boldsymbol{\nabla}\psi\cdot\boldsymbol{\kappa})B_0^2}{\mathcal{J}g^{\psi\psi}}\tilde{\xi}_\perp$$
$$- \boldsymbol{\nabla}\cdot\left(\mathbf{B}_0\times\boldsymbol{\nabla}\psi\frac{B_0}{|\boldsymbol{\nabla}\psi|}\tilde{\xi}_\wedge\right) . \tag{2.66}$$

Note that since $\boldsymbol{\nabla}\times\boldsymbol{B}_0 = \mu_0\boldsymbol{J}_0$ and lines of current are contained within a particular flux surface then the following equality holds:

$$\boldsymbol{\nabla}\cdot(\mathbf{B}_0\times\boldsymbol{\nabla}\psi) = \boldsymbol{\nabla}\psi\cdot(\boldsymbol{\nabla}\times\boldsymbol{B}_0) - \boldsymbol{B}_0\cdot(\boldsymbol{\nabla}\times\boldsymbol{\nabla}\psi) = 0 . \tag{2.67}$$

So the total pressure is rewritten more simply as:

$$\mu_0 p_T = -\frac{B_0^2}{\mathcal{J}}\partial_\psi \tilde{\xi}_\perp - \frac{B_0^2}{\mathcal{J}}\partial_\vartheta\left(\frac{g^{\psi\vartheta}}{g^{\psi\psi}}\tilde{\xi}_\perp\right) - \frac{(2\boldsymbol{\nabla}\psi\cdot\boldsymbol{\kappa})B_0^2}{\mathcal{J}g^{\psi\psi}}\tilde{\xi}_\perp$$
$$- g^{\psi\psi}(\boldsymbol{T}\cdot\boldsymbol{\nabla})\left(\frac{B_0}{|\boldsymbol{\nabla}\psi|}\tilde{\xi}_\wedge\right) . \tag{2.68}$$

We use Eq. (2.68) to eliminate the total pressure term from Eqs. (2.47) and (2.63), which results in:

$$\frac{\mu_0\rho_0}{\mathcal{J}g^{\psi\psi}}\frac{\partial^2\tilde{\xi}_\perp}{\partial t^2} =$$
$$\partial_\psi\left(\frac{B_0^2}{\mathcal{J}}\partial_\psi\tilde{\xi}_\perp + \frac{B_0^2}{\mathcal{J}}\partial_\vartheta\left(\frac{g^{\psi\vartheta}}{g^{\psi\psi}}\tilde{\xi}_\perp\right) + \frac{(2\boldsymbol{\nabla}\psi\cdot\boldsymbol{\kappa})B_0^2}{\mathcal{J}g^{\psi\psi}}\tilde{\xi}_\perp\right)$$
$$+ \frac{g^{\psi\vartheta}}{g^{\psi\psi}}\partial_\vartheta\left(\frac{B_0^2}{\mathcal{J}}\partial_\psi\tilde{\xi}_\perp + \frac{B_0^2}{\mathcal{J}}\partial_\vartheta\left(\frac{g^{\psi\vartheta}}{g^{\psi\psi}}\tilde{\xi}_\perp\right) + \frac{(2\boldsymbol{\nabla}\psi\cdot\boldsymbol{\kappa})B_0^2}{\mathcal{J}g^{\psi\psi}}\tilde{\xi}_\perp\right)$$
$$- \frac{(2\boldsymbol{\nabla}\psi\cdot\boldsymbol{\kappa})B_0^2}{\mathcal{J}g^{\psi\psi}}\partial_\psi\tilde{\xi}_\perp - \frac{(2\boldsymbol{\nabla}\psi\cdot\boldsymbol{\kappa})B_0^2}{\mathcal{J}g^{\psi\psi}}\partial_\vartheta\left(\frac{g^{\psi\vartheta}}{g^{\psi\psi}}\tilde{\xi}_\perp\right) - \frac{(2\boldsymbol{\nabla}\psi\cdot\boldsymbol{\kappa})^2B_0^2}{\mathcal{J}g^{\psi\psi 2}}\tilde{\xi}_\perp$$
$$+ (\mathbf{B_0}\cdot\boldsymbol{\nabla})\left(\frac{(\boldsymbol{B_0}\cdot\boldsymbol{\nabla})\{\frac{1}{\mathcal{J}}\tilde{\xi}_\perp\}}{g^{\psi\psi}}\right) - \frac{S}{\mathcal{J}}\frac{(g^{\psi\psi}S - \mu_0\mathbf{j}_0\cdot\mathbf{B}_0)}{B_0^2}\tilde{\xi}_\perp + \mu_0 p_0^{'}\frac{(2\boldsymbol{\nabla}\psi\cdot\boldsymbol{\kappa})}{\mathcal{J}g^{\psi\psi}}\tilde{\xi}_\perp$$
$$+ \partial_\psi\left(g^{\psi\psi}(\boldsymbol{T}\cdot\boldsymbol{\nabla})\frac{B_0}{|\nabla\psi|}\tilde{\xi}_\wedge\right) + \frac{g^{\psi\vartheta}}{g^{\psi\psi}}\partial_\vartheta\left(g^{\psi\psi}(\boldsymbol{T}\cdot\boldsymbol{\nabla})\frac{B_0}{|\nabla\psi|}\tilde{\xi}_\wedge\right)$$
$$- (2\boldsymbol{\nabla}\psi\cdot\boldsymbol{\kappa})(\boldsymbol{T}\cdot\boldsymbol{\nabla})\left(\frac{B_0}{|\nabla\psi|}\tilde{\xi}_\wedge\right) + \frac{g^{\psi\psi}S - \mu_0\mathbf{J}_0\cdot\mathbf{B}_0}{B_0^2}(\mathbf{B_0}\cdot\boldsymbol{\nabla})\left(\frac{B_0}{|\nabla\psi|}\tilde{\xi}_\wedge\right) , \tag{2.69}$$

$$
\begin{aligned}
&\mathcal{J}\mu_0\rho_0\frac{\partial^2\tilde{\xi}_\wedge}{\partial t^2} = \\
&\mathcal{J}|\nabla\psi|B_0(\boldsymbol{T}\cdot\boldsymbol{\nabla})\left(\frac{1}{\mathcal{J}}\partial_\psi\tilde{\xi}_\perp + \frac{1}{\mathcal{J}}\partial_\vartheta\left(\frac{g^{\psi\vartheta}}{g^{\psi\psi}}\tilde{\xi}_\perp\right)\right) + \mathcal{J}|\nabla\psi|B_0(\boldsymbol{T}\cdot\boldsymbol{\nabla})\left(\frac{(2\boldsymbol{\nabla}\psi\cdot\boldsymbol{\kappa})}{\mathcal{J}g^{\psi\psi}}\tilde{\xi}_\perp\right) \\
&-\frac{\mathcal{J}B_0}{|\nabla\psi|}(\mathbf{B_0}\cdot\boldsymbol{\nabla})\left[\frac{g^{\psi\psi}S-\mu_0\mathbf{J}_0\cdot\mathbf{B}_0}{\mathcal{J}B_0^2}\tilde{\xi}_\perp\right] \\
&+\mathcal{J}|\nabla\psi|B_0(\boldsymbol{T}\cdot\boldsymbol{\nabla})\left(\frac{g^{\psi\psi}}{B_0^2}(\boldsymbol{T}\cdot\boldsymbol{\nabla})\left(\frac{B_0}{|\nabla\psi|}\tilde{\xi}_\wedge\right)\right) \\
&+\frac{\mathcal{J}B_0}{|\nabla\psi|}(\mathbf{B_0}\cdot\boldsymbol{\nabla})\left[\frac{g^{\psi\psi}}{B_0^2}(\mathbf{B_0}\cdot\boldsymbol{\nabla})\left(\frac{B_0}{|\nabla\psi|}\tilde{\xi}_\wedge\right)\right] . \qquad (2.70)
\end{aligned}
$$

These equations are equivalent to the ideal-MHD wave equation given by Eqs. (3.51)-(3.54) of [39], reformulated for the components of $\boldsymbol{\xi}$ given by Eq. (2.18). We have also applied a specific axisymmetric geometry and the additional assumptions of zero plasma-β and no hot-ion pressure tensor.

2.3 Hall-MHD

To obtain the linearised Hall-MHD equations describing the Eulerian perturbations to the MHD equilibrium we neglect the plasma pressure terms, i.e. p_0 and p_1, in favour of magnetic terms. This ensures that there is no force along the equilibrium magnetic field and $v_{1\|} = 0$. However, this condition is not enforced in setting up the equilibrium. We recall the linearised Hall-MHD equations Eqs. (2.1)-(2.6) and write the mass, momentum and induction equations again here:

$$\frac{\partial\rho_1}{\partial t} = -\boldsymbol{\nabla}\cdot(\rho_0\mathbf{v}_1) , \qquad (2.71)$$

$$\rho_0\frac{\partial\mathbf{v}_1}{\partial t} = \mathbf{J}_0\times\mathbf{B}_1 + \mathbf{J}_1\times\mathbf{B}_0 , \qquad (2.72)$$

$$\frac{\partial\mathbf{B}_1}{\partial t} = \boldsymbol{\nabla}\times\left[\mathbf{v}_1\times\mathbf{B}_0 - \frac{1}{en_0}(\mathbf{J}_0\times\mathbf{B}_1 + \mathbf{J}_1\times\mathbf{B}_0)\right] . \qquad (2.73)$$

The equilibrium density can be written $\rho_0 = (m_e + m_i)n_0 \simeq m_i n_0$ since we assume $m_e \ll m_i$. We again introduce the plasma displacement to write the induction equation as:

$$\mathbf{B}_1 = \boldsymbol{\nabla}\times\left[\boldsymbol{\xi}\times\mathbf{B}_0 - H\frac{\partial\boldsymbol{\xi}}{\partial t}\right] , \qquad (2.74)$$

where we introduced the mass-charge ratio $H = m_i/e$. We introduce a modified displacement $\boldsymbol{\eta}$ where:

$$\boldsymbol{\eta} = \boldsymbol{\xi} + \frac{H}{B_0^2}\frac{\partial\boldsymbol{\xi}}{\partial t}\times\mathbf{B}_0 . \qquad (2.75)$$

This allows us to reformulate the induction equation into the ideal-MHD form:

$$\mathbf{B}_1 = \boldsymbol{\nabla} \times (\boldsymbol{\eta} \times \mathbf{B}_0) \ . \tag{2.76}$$

The modified displacement $\boldsymbol{\eta}$ is decomposed in the same manner as $\boldsymbol{\xi}$, i.e. such that $\eta_\perp = \boldsymbol{\eta} \cdot \boldsymbol{\nabla}\psi$ and $\eta_\wedge = \boldsymbol{\eta} \cdot \mathbf{T}$. We know that in the zero plasma-β regime that $\xi_\parallel = 0$, so taking the scalar product of (2.75) with B_0 shows that $\eta_\parallel = 0$ for zero plasma-β. The remaining components of $\boldsymbol{\eta}$ are then written in terms of the chosen geometry as:

$$\eta_\perp = \xi_\perp + H \frac{g^{\psi\psi}}{B_0^2} \frac{\partial \xi_\wedge}{\partial t} \ , \tag{2.77}$$

$$\eta_\wedge = \xi_\wedge - H \frac{1}{g^{\psi\psi}} \frac{\partial \xi_\perp}{\partial t} \ . \tag{2.78}$$

The choice of the modified displacement means the expressions for the perturbed magnetic field components have the same mathematical form but with $\boldsymbol{\eta}$ in the place of $\boldsymbol{\xi}$:

$$b_\perp = (\mathbf{B}_0 \cdot \boldsymbol{\nabla})\eta_\perp \ , \tag{2.79}$$

$$b_\wedge = \frac{g^{\psi\psi}}{B_0^2}[(\mathbf{B}_0 \cdot \boldsymbol{\nabla})\eta_\wedge - S\eta_\perp] \ , \tag{2.80}$$

$$b_\parallel = -\boldsymbol{\nabla} \cdot (B_0^2 \boldsymbol{\eta}) \ . \tag{2.81}$$

For ideal-MHD in the zero plasma-β limit we write the linearised perturbed momentum equations as:

$$\frac{\mu_0 \rho_0}{\mathcal{J} g^{\psi\psi}} \frac{\partial^2 \tilde{\xi}_\perp}{\partial t^2} = \mathcal{G}_\perp(\tilde{\xi}_\perp, \tilde{\xi}_\wedge) \ , \tag{2.82}$$

$$\mathcal{J} \mu_0 \rho_0 \frac{\partial^2 \tilde{\xi}_\wedge}{\partial t^2} = \mathcal{G}_\wedge(\tilde{\xi}_\perp, \tilde{\xi}_\wedge) \ , \tag{2.83}$$

where $\mathcal{G}_\perp$ and $\mathcal{G}_\wedge$ represent the right-hand side terms of Eqs. (2.69) and (2.70) respectively. It follows that in Hall-MHD we can easily rewrite those momentum equations as:

$$\frac{\mu_0 \rho_0}{\mathcal{J} g^{\psi\psi}} \frac{\partial^2 \tilde{\xi}_\perp}{\partial t^2} = \mathcal{G}_\perp(\tilde{\eta}_\perp, \tilde{\eta}_\wedge) \ , \tag{2.84}$$

$$\mathcal{J} \mu_0 \rho_0 \frac{\partial^2 \tilde{\xi}_\wedge}{\partial t^2} = \mathcal{G}_\wedge(\tilde{\eta}_\perp, \tilde{\eta}_\wedge) \ , \tag{2.85}$$

where we apply the variable transformation of Eqs. (2.64)-(2.65) to η, i.e.:

$$\tilde{\eta}_\perp = \mathcal{J}\eta_\perp = \tilde{\xi}_\perp + H\mathcal{J}\frac{|\boldsymbol{\nabla}\psi|}{B_0}\frac{\partial\tilde{\xi}_\wedge}{\partial t} \ , \tag{2.86}$$

$$\tilde{\eta}_\wedge = \frac{|\boldsymbol{\nabla}\psi|}{B_0}\eta_\wedge = \tilde{\xi}_\wedge - \frac{H}{\mathcal{J}}\frac{1}{B_0|\boldsymbol{\nabla}\psi|}\frac{\partial\tilde{\xi}_\perp}{\partial t} \ . \tag{2.87}$$

Eq. (2.75) implies that in the limit $\omega H/B_0 \to 0$, i.e. $\omega \ll \omega_{ci}$, then $\boldsymbol{\eta} \to \boldsymbol{\xi}$ and the equations of ideal-MHD are recovered. We rewrite Eqs. (2.84)-(2.85) in terms of $\boldsymbol{\xi}$, arriving at:

$$\frac{\mu_0\rho_0}{\mathcal{J}g^{\psi\psi}}\frac{\partial^2\tilde{\xi}_\perp}{\partial t^2} = \mathcal{G}_\perp(\tilde{\xi}_\perp,\tilde{\xi}_\wedge) + H\mathcal{G}_\perp\left(\mathcal{J}\frac{|\boldsymbol{\nabla}\psi|}{B_0}\frac{\partial\tilde{\xi}_\wedge}{\partial t}, -\frac{1}{\mathcal{J}B_0|\boldsymbol{\nabla}\psi|}\frac{\partial\tilde{\xi}_\perp}{\partial t}\right) \ , \tag{2.88}$$

$$\mathcal{J}\mu_0\rho_0\frac{\partial^2\tilde{\xi}_\wedge}{\partial t^2} = \mathcal{G}_\wedge(\tilde{\xi}_\perp,\tilde{\xi}_\wedge) + H\mathcal{G}_\wedge\left(\mathcal{J}\frac{|\boldsymbol{\nabla}\psi|}{B_0}\frac{\partial\tilde{\xi}_\wedge}{\partial t}, -\frac{1}{\mathcal{J}B_0|\boldsymbol{\nabla}\psi|}\frac{\partial\tilde{\xi}_\perp}{\partial t}\right) \ , \tag{2.89}$$

We apply the following transformation to the radial co-ordinate, $\psi \to s = \sqrt{\psi}$, meaning the radial derivatives are transformed: $\partial_\psi \to (1/2s)\partial_s$. Multiplying through by the factor $\frac{\partial\psi}{\partial s} = 2s$ more easily facilitates some integration by parts that will be applied later on, and so the linearised Hall-MHD equations become:

$$2s\frac{\mu_0\rho_0}{\mathcal{J}g^{\psi\psi}}\frac{\partial^2\tilde{\xi}_\perp}{\partial t^2} = \tilde{\mathcal{G}}_\perp(\tilde{\xi}_\perp,\tilde{\xi}_\wedge) + \frac{\partial}{\partial t}\left\{H\tilde{\mathcal{G}}_\perp\left(\mathcal{J}\frac{|\boldsymbol{\nabla}\psi|}{B_0}\tilde{\xi}_\wedge, -\frac{1}{\mathcal{J}B_0|\boldsymbol{\nabla}\psi|}\tilde{\xi}_\perp\right)\right\} \ , \tag{2.90}$$

$$2s\mathcal{J}\mu_0\rho_0\frac{\partial^2\tilde{\xi}_\wedge}{\partial t^2} = \tilde{\mathcal{G}}_\wedge(\tilde{\xi}_\perp,\tilde{\xi}_\wedge) + \frac{\partial}{\partial t}\left\{H\tilde{\mathcal{G}}_\wedge\left(\mathcal{J}\frac{|\boldsymbol{\nabla}\psi|}{B_0}\tilde{\xi}_\wedge, -\frac{1}{\mathcal{J}B_0|\boldsymbol{\nabla}\psi|}\tilde{\xi}_\perp\right)\right\} \ , \tag{2.91}$$

where we can move the time derivative outside of $\mathcal{G}$ due to the assumption that the equilibrium is static, i.e. $\partial_t A_0 = 0$. The terms $\tilde{\mathcal{G}}_\perp$ and $\tilde{\mathcal{G}}_\wedge$ are:

$$
\begin{aligned}
&\tilde{\mathcal{G}}_\perp(\tilde{\xi}_\perp, \tilde{\xi}_\wedge) = \\
&\partial_s\left(\frac{B_0^2}{2s\mathcal{J}}\partial_s\tilde{\xi}_\perp + \frac{B_0^2}{\mathcal{J}}\partial_\vartheta\left(\frac{g^{\psi\vartheta}}{g^{\psi\psi}}\tilde{\xi}_\perp\right) + \frac{(2\boldsymbol{\nabla}\psi\cdot\boldsymbol{\kappa})B_0^2}{\mathcal{J}g^{\psi\psi}}\tilde{\xi}_\perp\right) \\
&+ \frac{g^{\psi\vartheta}}{g^{\psi\psi}}\partial_\vartheta\left(\frac{B_0^2}{\mathcal{J}}\partial_s\tilde{\xi}_\perp + 2s\frac{B_0^2}{\mathcal{J}}\partial_\vartheta\left(\frac{g^{\psi\vartheta}}{g^{\psi\psi}}\tilde{\xi}_\perp\right) + 2s\frac{(2\boldsymbol{\nabla}\psi\cdot\boldsymbol{\kappa})B_0^2}{\mathcal{J}g^{\psi\psi}}\tilde{\xi}_\perp\right) \\
&- \frac{(2\boldsymbol{\nabla}\psi\cdot\boldsymbol{\kappa})B_0^2}{\mathcal{J}g^{\psi\psi}}\partial_s\tilde{\xi}_\perp - 2s\frac{(2\boldsymbol{\nabla}\psi\cdot\boldsymbol{\kappa})B_0^2}{\mathcal{J}g^{\psi\psi}}\partial_\vartheta\left(\frac{g^{\psi\vartheta}}{g^{\psi\psi}}\tilde{\xi}_\perp\right) - 2s\frac{(2\boldsymbol{\nabla}\psi\cdot\boldsymbol{\kappa})^2B_0^2}{\mathcal{J}g^{\psi\psi}{}^2}\tilde{\xi}_\perp \\
&+ 2s(\mathbf{B_0}\cdot\boldsymbol{\nabla})\left(\frac{(\boldsymbol{B_0}\cdot\boldsymbol{\nabla})\{\frac{1}{\mathcal{J}}\tilde{\xi}_\perp\}}{g^{\psi\psi}}\right) - 2s\frac{S}{\mathcal{J}}\frac{(g^{\psi\psi}S - \mu_0\mathbf{j}_0\cdot\mathbf{B}_0)}{B_0^2}\tilde{\xi}_\perp \\
&+ \partial_s\left(g^{\psi\psi}(\boldsymbol{T}\cdot\boldsymbol{\nabla})\frac{B_0}{|\nabla\psi|}\tilde{\xi_\wedge}\right) + 2s\frac{g^{\psi\vartheta}}{g^{\psi\psi}}\partial_\vartheta\left(g^{\psi\psi}(\boldsymbol{T}\cdot\boldsymbol{\nabla})\frac{B_0}{|\nabla\psi|}\tilde{\xi_\wedge}\right) \\
&- 2s(2\boldsymbol{\nabla}\psi\cdot\boldsymbol{\kappa})(\boldsymbol{T}\cdot\boldsymbol{\nabla})\left(\frac{B_0}{|\nabla\psi|}\tilde{\xi_\wedge}\right) \\
&+ 2s\frac{g^{\psi\psi}S - \mu_0\mathbf{J}_0\cdot\mathbf{B}_0}{B_0^2}(\mathbf{B_0}\cdot\boldsymbol{\nabla})\left(\frac{B_0}{|\nabla\psi|}\tilde{\xi_\wedge}\right) ,
\end{aligned}
\tag{2.92}
$$

$$
\begin{aligned}
\tilde{\mathcal{G}}_\wedge(\tilde{\xi}_\perp, \tilde{\xi}_\wedge) \; =& \mathcal{J}|\nabla\psi|B_0(\boldsymbol{T}\cdot\boldsymbol{\nabla})\left(\frac{1}{\mathcal{J}}\partial_s\tilde{\xi}_\perp + \frac{2s}{\mathcal{J}}\partial_\vartheta\left(\frac{g^{\psi\vartheta}}{g^{\psi\psi}}\tilde{\xi}_\perp\right) + 2s\frac{(2\boldsymbol{\nabla}\psi\cdot\boldsymbol{\kappa})}{\mathcal{J}g^{\psi\psi}}\tilde{\xi}_\perp\right) \\
&- 2s\frac{\mathcal{J}B_0}{|\nabla\psi|}(\mathbf{B_0}\cdot\boldsymbol{\nabla})\left[\frac{g^{\psi\psi}S - \mu_0\mathbf{J}_0\cdot\mathbf{B}_0}{\mathcal{J}B_0^2}\tilde{\xi}_\perp\right] \\
&+ 2s\mathcal{J}|\nabla\psi|B_0(\boldsymbol{T}\cdot\boldsymbol{\nabla})\left(\frac{g^{\psi\psi}}{B_0^2}(\boldsymbol{T}\cdot\boldsymbol{\nabla})\left(\frac{B_0}{|\nabla\psi|}\tilde{\xi_\wedge}\right)\right) \\
&+ 2s\frac{\mathcal{J}B_0}{|\nabla\psi|}(\mathbf{B_0}\cdot\boldsymbol{\nabla})\left[\frac{g^{\psi\psi}}{B_0^2}(\mathbf{B_0}\cdot\boldsymbol{\nabla})\left(\frac{B_0}{|\nabla\psi|}\tilde{\xi_\wedge}\right)\right] .
\end{aligned}
\tag{2.93}
$$

For completeness we expand out the Hall terms of Eqs. (2.90)-(2.91) as we use the product rule to simplify some terms, in particular:

$$
\begin{aligned}
\partial_s\left(\frac{(2\boldsymbol{\nabla}\psi\cdot\boldsymbol{\kappa})B_0}{|\nabla\psi|}\tilde{\xi}_\wedge\right) - \frac{(2\boldsymbol{\nabla}\psi\cdot\boldsymbol{\kappa})B_0^2}{\mathcal{J}g^{\psi\psi}}\partial_s\left(\mathcal{J}\frac{|\nabla\psi|}{B_0}\tilde{\xi}_\wedge\right) = \\
\partial_s\left(\frac{(2\boldsymbol{\nabla}\psi\cdot\boldsymbol{\kappa})B_0^2}{\mathcal{J}g^{\psi\psi}}\right)\mathcal{J}\frac{|\nabla\psi|}{B_0}\tilde{\xi}_\wedge ,
\end{aligned}
\tag{2.94}
$$

The Hall terms are then:

$$
\begin{aligned}
&\tilde{\mathcal{G}}_\perp\left(\mathcal{J}\frac{|\boldsymbol{\nabla}\psi|}{B_0}\tilde{\xi}_\wedge, -\frac{1}{\mathcal{J}B_0|\boldsymbol{\nabla}\psi|}\tilde{\xi}_\perp\right) = \\
&-\partial_s\left(g^{\psi\psi}(\boldsymbol{T}\cdot\boldsymbol{\nabla})\frac{1}{\mathcal{J}g^{\psi\psi}}\tilde{\xi}_\perp\right) - 2s\frac{g^{\psi\vartheta}}{g^{\psi\psi}}\partial_\vartheta\left(g^{\psi\psi}(\boldsymbol{T}\cdot\boldsymbol{\nabla})\frac{1}{\mathcal{J}g^{\psi\psi}}\tilde{\xi}_\perp\right) \\
&+2s(2\boldsymbol{\nabla}\psi\cdot\boldsymbol{\kappa})(\boldsymbol{T}\cdot\boldsymbol{\nabla})\left(\frac{1}{\mathcal{J}g^{\psi\psi}}\tilde{\xi}_\perp\right) - 2s\frac{g^{\psi\psi}S-\mu_0\mathbf{j}_0\cdot\mathbf{B}_0}{B_0^2}(\mathbf{B_0}\cdot\boldsymbol{\nabla})\left(\frac{1}{\mathcal{J}g^{\psi\psi}}\tilde{\xi}_\perp\right) \\
&+\partial_s\left(\frac{B_0|\nabla\psi|}{2s}\partial_s\tilde{\xi}_\wedge + \frac{B_0^2}{\mathcal{J}}\partial_\psi\left(\mathcal{J}\frac{|\nabla\psi|}{B_0}\right)\tilde{\xi}_\wedge + \frac{B_0^2}{\mathcal{J}}\partial_\vartheta\left(\frac{g^{\psi\vartheta}}{g^{\psi\psi}}\mathcal{J}\frac{|\nabla\psi|}{B_0}\tilde{\xi}_\wedge\right)\right) \\
&+\frac{g^{\psi\vartheta}}{g^{\psi\psi}}\partial_\vartheta\left(B_0|\nabla\psi|\partial_s\tilde{\xi}_\wedge + 2s\frac{B_0^2}{\mathcal{J}}\partial_\psi\left(\mathcal{J}\frac{|\nabla\psi|}{B_0}\right)\tilde{\xi}_\wedge + 2s\frac{B_0^2}{\mathcal{J}}\partial_\vartheta\left(\frac{g^{\psi\vartheta}}{g^{\psi\psi}}\mathcal{J}\frac{|\nabla\psi|}{B_0}\tilde{\xi}_\wedge\right)\right. \\
&\left.+2s\frac{(2\boldsymbol{\nabla}\psi\cdot\boldsymbol{\kappa})B_0}{|\nabla\psi|}\tilde{\xi}_\wedge\right) + \partial_s\left(\frac{(2\boldsymbol{\nabla}\psi\cdot\boldsymbol{\kappa})B_0^2}{\mathcal{J}g^{\psi\psi}}\right)\mathcal{J}\frac{|\nabla\psi|}{B_0}\tilde{\xi}_\wedge \\
&-2s\frac{(2\boldsymbol{\nabla}\psi\cdot\boldsymbol{\kappa})B_0^2}{\mathcal{J}g^{\psi\psi}}\partial_\vartheta\left(\frac{g^{\psi\vartheta}}{g^{\psi\psi}}\mathcal{J}\frac{|\nabla\psi|}{B_0}\tilde{\xi}_\wedge\right) - 2s\frac{(2\boldsymbol{\nabla}\psi\cdot\boldsymbol{\kappa})^2B_0}{g^{\psi\psi}|\nabla\psi|}\tilde{\xi}_\wedge \\
&+2s(\mathbf{B_0}\cdot\boldsymbol{\nabla})\left(\frac{(\boldsymbol{B_0}\cdot\boldsymbol{\nabla})\{\frac{|\nabla\psi|}{B_0}\tilde{\xi}_\wedge\}}{g^{\psi\psi}}\right) - 2s\frac{S}{B_0^2}(g^{\psi\psi}S-\mu_0\mathbf{j}_0\cdot\mathbf{B}_0)\frac{|\nabla\psi|}{B_0}\tilde{\xi}_\wedge\ , \qquad (2.95)
\end{aligned}
$$

$$
\begin{aligned}
&\tilde{\mathcal{G}}_\wedge\left(\mathcal{J}\frac{|\boldsymbol{\nabla}\psi|}{B_0}\tilde{\xi}_\wedge, -\frac{1}{\mathcal{J}B_0|\boldsymbol{\nabla}\psi|}\tilde{\xi}_\perp\right) = \\
&-2s\mathcal{J}|\nabla\psi|B_0(\boldsymbol{T}\cdot\boldsymbol{\nabla})\left(\frac{g^{\psi\psi}}{B_0^2}(\boldsymbol{T}\cdot\boldsymbol{\nabla})\left(\frac{1}{\mathcal{J}g^{\psi\psi}}\tilde{\xi}_\perp\right)\right) \\
&-2s\frac{\mathcal{J}B_0}{|\nabla\psi|}(\mathbf{B_0}\cdot\boldsymbol{\nabla})\left[\frac{g^{\psi\psi}}{B_0^2}(\mathbf{B_0}\cdot\boldsymbol{\nabla})\left(\frac{1}{\mathcal{J}g^{\psi\psi}}\tilde{\xi}_\perp\right)\right] \\
&+\mathcal{J}|\nabla\psi|B_0(\boldsymbol{T}\cdot\boldsymbol{\nabla})\left(\frac{|\nabla\psi|}{B_0}\partial_s\tilde{\xi}_\wedge + \frac{2s}{\mathcal{J}}\partial_\psi\left(\mathcal{J}\frac{|\nabla\psi|}{B_0}\right)\tilde{\xi}_\wedge + \frac{2s}{\mathcal{J}}\partial_\vartheta\left(\frac{g^{\psi\vartheta}}{g^{\psi\psi}}\mathcal{J}\frac{|\nabla\psi|}{B_0}\tilde{\xi}_\wedge\right)\right) \\
&+2s\mathcal{J}|\nabla\psi|B_0(\boldsymbol{T}\cdot\boldsymbol{\nabla})\left(\frac{(2\boldsymbol{\nabla}\psi\cdot\boldsymbol{\kappa})}{|\nabla\psi|B_0}\tilde{\xi}_\wedge\right) \\
&-2s\frac{\mathcal{J}B_0}{|\nabla\psi|}(\mathbf{B_0}\cdot\boldsymbol{\nabla})\left[\frac{g^{\psi\psi}S-\mu_0\mathbf{j}_0\cdot\mathbf{B}_0}{B_0^2}\frac{|\nabla\psi|}{B_0}\tilde{\xi}_\wedge\right]\ . \qquad (2.96)
\end{aligned}
$$

2.4 MHD wave coupling

There exist physical mechanisms via which the different types of MHD mode can exchange energy, converting one type of MHD wave into another. In particular, CAEs, which are discrete fast-magnetoacoustic modes, can exchange energy with continuum modes through *resonant mode conversion*. Take the example of homogeneous plasma cylinder and introduce a radial density profile to the plasma. This

means that the Alfvén speed has a radial profile and so the shear Alfvén dispersion relation, $\omega_A(r) = V_A(r)k_{\|}$, has a unique Alfvén frequency for every flux surface $\psi(r)$. If the CAE frequency matches the local Alfvén frequency on a particular flux surface then resonant mode conversion can occur [20]. Fig. 2.2 shows an example of this phenomenon occurring in output from Whales2. The 'pure' CAE is modified by a local spike, which is the shear Alfvén mode on the flux surface where the frequencies match. CAEs can couple to the slow continuum in the same way, though in most tokamak plasmas $\omega_{CAE} > \omega_S$.

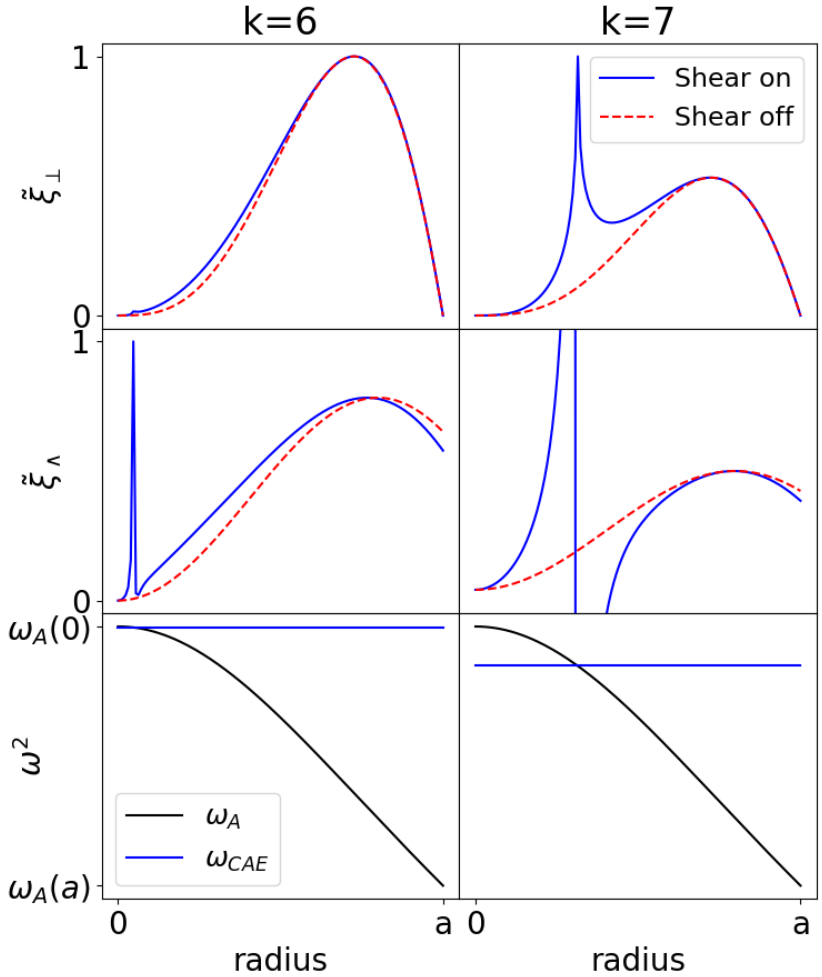

Figure 2.2: The perturbed displacement components of a CAE mode in a cylinder are shown for axial wavenumbers $k = 6, 7$ and radially varying equilibrium density profile. The resonant mode conversion can be seen to occur at the point where the CAE frequency coincides with the local Alfvén frequency. Solving for the same mode whilst neglecting the shear terms removes this local mode conversion.

This physical coupling is important in real plasmas as a damping mechanism for the CAEs, but it complicates the study of CAE properties and so we

employ strategies in Whales2 to mitigate these couplings. We have assumed zero plasma-β in the perturbed MHD equations, Eqs (2.90)-(2.91), to exclude the slow-magnetoacoustic modes from the solutions. In order to suppress the shear Alfvén continuum so that $\omega_{CAE} > \omega_A$ we identify terms in the MHD equations that contribute predominately to shear Alfvén modes in order to neglect them from Whales2. We want to do this whilst modifying the 'pure' CAE mode as little as possible, so we aim to be parsimonious in the terms we neglect. We follow the practice of [3] which identifies terms of the order $k_{\|}^2$, i.e. $(\mathbf{B}_0 \cdot \boldsymbol{\nabla})^2$ acting on a perturbed quantity, to be neglected. We shall refer to these simply as the *shear terms* when there is no ambiguity. Whales2 includes a user option to either include or neglect these terms from the perturbed MHD equations. Fig. 2.2 compares the output from Whales2 when the shear terms are either included or neglected for two cases where the CAE couples to the shear Alfvén continuum with varying coupling strength.

The inclusion of resistivity into the perturbed MHD equations lifts the resonant mode conversion of CAEs with the shear Alfvén continuum [20]. We chose not include resistivity in Whales2 as the objective of Whales2 is to study the effect of the Hall term on CAEs. The ideal-MHD equations are self-adjoint and so admit only real eigenvalues, $\omega^2 \in \mathbb{R}$. Therefore, the frequencies of modes in ideal-MHD are purely real or imaginary. The inclusion of either the Hall term or non-zero resistivity allows any complex frequency, so extra work would be required to separate the Hall effects from the dissipative effects.

2.5 Boundary Conditions

We introduce spatial boundary conditions to the Hall-MHD equations in order to represent the effect of having a physical outer boundary and to ensure the continuity of the plasma displacement at the magnetic axis. The solutions to the Hall-MHD wave equation must be 2π-periodic in both angular directions and these conditions will be automatically satisfied by the particular form that we will choose the solutions to have. In the radial direction there are two boundaries to consider: the outer wall and the magnetic axis. We assume that the plasma fully extends to the outer wall, i.e. that there is no vacuum region.

2.5.1 Magnetic Axis

The choice of co-ordinate system (see Section 2.2) suffers from a geometric singularity at the magnetic axis. This is merely due to the choice of co-ordinate system but means that we must impose a boundary condition at the magnetic axis to ensure

continuity of the plasma displacement, which we would expect physically. To derive the boundary conditions at the magnetic axis we follow a similar procedure to the analysis in [46]. We first assume that sufficiently near to the magnetic axis the flux surfaces are related to the local tokamak coordinates by:

$$R = R_0 + s\cos\vartheta \ , \tag{2.97}$$

$$\phi = \phi \ , \tag{2.98}$$

$$Z = s\sin\vartheta \ , \tag{2.99}$$

i.e. the flux surfaces in the vicinity of the magnetic axis are concentric circles centred on the magnetic axis. Note that the following analysis is also applicable for concentric ellipses centre on the magnetic axis, so we assume circles for brevity. The components of the displacement ξ_i for $i \in \{R, \phi, Z\}$ are analytic functions in the plasma volume so they are Taylor expanded around the magnetic axis. We are only concerned with the behaviour of the displacement in the R-Z plane and so keep the toroidal coordinate ϕ fixed. The Taylor expansions thus become:

$$\xi_i = A_i + B_i(R - R_0) + C_i Z + ... \tag{2.100}$$

$$= A_i + B_i s\cos\vartheta + C_i s\sin\vartheta + \mathcal{O}(s^2) \ , \tag{2.101}$$

with A_i, B_i, C_i constants.

The position vector is $\boldsymbol{r} = R\hat{R} + Z\hat{Z}$ and so the flux coordinates are related to the tokamak coordinates as:

$$\hat{s} = \frac{1}{\left|\frac{\partial \boldsymbol{r}}{\partial s}\right|}\frac{\partial \boldsymbol{r}}{\partial s} = \cos\vartheta\hat{R} + \sin\vartheta\hat{Z} \ , \tag{2.102}$$

$$\hat{\vartheta} = \frac{1}{\left|\frac{\partial \boldsymbol{r}}{\partial \vartheta}\right|}\frac{\partial \boldsymbol{r}}{\partial \vartheta} = -\sin\vartheta\hat{R} + \cos\vartheta\hat{Z} \ , \tag{2.103}$$

or, inversely:

$$\hat{R} = \cos\vartheta\hat{s} - \sin\vartheta\hat{\vartheta} \ , \tag{2.104}$$

$$\hat{Z} = \sin\vartheta\hat{s} + \cos\vartheta\hat{\vartheta} \ . \tag{2.105}$$

The displacement vector can be written as:

$$\boldsymbol{\xi} = \xi_s\hat{s} + \xi_\vartheta\hat{\vartheta} + \xi_\phi\hat{\phi} \tag{2.106}$$

$$= \xi_R\hat{R} + \xi_Z\hat{Z} + \xi_\phi\hat{\phi} \ . \tag{2.107}$$

Substituting $(\hat{R}, \hat{Z})$ in terms of $(\hat{s}, \hat{\vartheta})$ in Eq. (2.107) implies that:

$$\xi_s = \xi_R \cos\vartheta + \xi_Z \sin\vartheta \ , \tag{2.108}$$

$$\xi_\vartheta = -\xi_R \sin\vartheta + \xi_Z \cos\vartheta \ . \tag{2.109}$$

We use Eq. (2.101) to expand this out to:

$$\begin{aligned}\xi_s =& \frac{1}{2}(B_R + C_Z)s + A_R \cos\vartheta + A_Z \sin\vartheta + \frac{1}{2}(B_R - C_Z)s\cos 2\vartheta \\ &+ \frac{1}{2}(C_R + B_Z)s\sin 2\vartheta + \mathcal{O}(s^2) \ , \end{aligned}\tag{2.110}$$

$$\begin{aligned}\xi_\vartheta =& \frac{1}{2}(B_Z - C_R)s + A_Z \cos\vartheta - A_R \sin\vartheta + \frac{1}{2}(B_Z + C_R)s\cos 2\vartheta \\ &+ \frac{1}{2}(C_Z - B_R)s\sin 2\vartheta + \mathcal{O}(s^2) \ , \end{aligned}\tag{2.111}$$

$$\xi_\phi = A_\phi + B_\phi s\cos\vartheta + C_\phi s \sin\vartheta + \mathcal{O}(s^2) \ . \tag{2.112}$$

We expand $\boldsymbol{\xi}$ as a Fourier series in the poloidal direction, giving:

$$\boldsymbol{\xi}(s, \vartheta) = \sum_{m=-\infty}^{\infty} \boldsymbol{\xi}^m(s) e^{im\vartheta} \tag{2.113}$$

We now compare Eqs. (2.110) - (2.112) to Eq. (2.113) to derive a boundary condition for each component of the Fourier expansion at the magnetic axis. The components ξ_s and ξ_ϑ have the same form and so we focus on ξ_s to determine the boundary condition for both of these components.

$\mathbf{m = 0}$

For $m = 0$ then we identify the components of $\boldsymbol{\xi}^0$ with:

$$\xi_s^0(s) = \frac{1}{2}(B_R + C_Z)s + \mathcal{O}(s^2) \ , \tag{2.114}$$

$$\xi_\phi^0(s) = A_\phi + \mathcal{O}(s^2) \ . \tag{2.115}$$

Taking the limit $s \to 0$, i.e. at the magnetic axis, then $\xi_s^0 \to 0$ and $\xi_\phi^0 \to A_\phi$. Taking the radial derivative then $\partial\xi_\phi^0/\partial s \sim \mathcal{O}(s)$ and so $\partial\xi_\phi^0/\partial s \to 0$ as $s \to 0$. We may therefore state the boundary condition for m=0 as:

$$\xi_s^0 = 0 \ , \ \xi_\vartheta^0 = 0 \ , \ \frac{\partial \xi_\phi^0}{\partial s} = 0 \ . \tag{2.116}$$

$\mathbf{m = \pm 1}$

We consider solely the $m = 1$ Fourier harmonic, noting that the $m = -1$ case will have the same result. We identify the real and imaginary components of $\boldsymbol{\xi}^1 e^{i\vartheta}$:

$$\xi^1_\alpha e^{i\vartheta} = \left\{\Re(\xi^1_\alpha)\cos\vartheta - \Im(\xi^1_\alpha)\sin\vartheta\right\} + i\left\{\Re(\xi^1_\alpha)\sin\vartheta + \Im(\xi^1_\alpha)\cos\vartheta\right\} \ . \tag{2.117}$$

So we compare this with Eqs. (2.110) - (2.112) to give the following equalities, in leading order in s:

$$\Re(\xi^1_s) = A_R \ , \quad \Im(\xi^1_s) = -A_Z \ , \tag{2.118}$$

$$\Re(\xi^1_\vartheta) = A_Z \ , \quad \Im(\xi^1_\vartheta) = A_R \ , \tag{2.119}$$

$$\Re(\xi^1_\phi) = B_\phi s \ , \quad \Im(\xi^1_\phi) = C_\phi s \ . \tag{2.120}$$

We take the limit $s \to 0$ to produce the final boundary conditions which, following the same reasoning as the $m = 0$ case, are:

$$\frac{\partial \xi^m_s}{\partial s} = 0 \ , \ \frac{\partial \xi^m_\vartheta}{\partial s} = 0 \ , \ \partial \xi^m_\phi = 0 \ , \quad m = \pm 1 \ . \tag{2.121}$$

$\mathbf{|m| \geq 2}$

For $|m| \geq 2$ it is clear that $\xi^m_s, \xi^m_\vartheta = \mathcal{O}(s^{|m|-1})$, $\xi^m_\phi = \mathcal{O}(s^{|m|})$ so the boundary condition becomes:

$$\xi^m_s = 0 \ , \ \xi^m_\phi = 0 \ , \ \xi^m_\vartheta = 0 \ . \tag{2.122}$$

The $m = \pm 1$ case implies a transverse displacement of the magnetic axis in the poloidal cross-section. For all other values of m, the magnetic axis remains at rest. This transverse displacement is characteristic of the *internal kink mode*, a plasma instability that can occur for the poloidal mode number $|m| = 1$ [9].

To translate the derived boundary conditions into conditions for variables $\xi_\perp, \xi_\wedge$ we take advantage of their definition as projections of the displacement vector:

$$\begin{aligned}
\xi_\perp &= \boldsymbol{\xi} \cdot \boldsymbol{\nabla}\psi \\
&= \frac{\partial \psi}{\partial s}\frac{\partial s}{\partial R}\xi_R + \frac{\partial \psi}{\partial s}\frac{\partial s}{\partial Z}\xi_Z \\
&= \frac{\partial \psi}{\partial s}\cos\vartheta\xi_R + \frac{\partial \psi}{\partial s}\sin\vartheta\xi_Z \\
&= \frac{\partial \psi}{\partial s}\xi_s \ .
\end{aligned} \tag{2.123}$$

Since $|\boldsymbol{\nabla}\psi| \sim \frac{\partial\psi}{\partial s} \sim s$ then it follows that $\xi_\perp = 0$ at the magnetic axis for all values of m. Furthermore, $\mathcal{J}$ is a non-zero constant as $s \to 0$ and so the modified displacement $\tilde{\xi}_\perp = \mathcal{J}\xi_\perp$ has the same boundary condition as $\xi_\perp$ at the magnetic axis.

For $\xi_\wedge$ recall that ψ is related to the equilibrium magnetic field as a stream-function and so:

$$\begin{aligned}
\xi_\wedge &= \boldsymbol{\xi} \cdot \frac{\boldsymbol{B}_0 \times \boldsymbol{\nabla}\psi}{|\boldsymbol{\nabla}\psi|^2} \\
&= \frac{1}{|\boldsymbol{\nabla}\psi|^2}\left[B_{0\phi}\frac{\partial\psi}{\partial Z}\xi_R + \left(B_{0Z}\frac{\partial\psi}{\partial R} - B_{0R}\frac{\partial\psi}{\partial Z}\right)\xi_\phi - B_{0\phi}\frac{\partial\psi}{\partial R}\xi_Z\right] \\
&= \frac{1}{|\boldsymbol{\nabla}\psi|^2}\left[B_{0\phi}\frac{\partial\psi}{\partial s}\sin\vartheta\xi_R + \frac{1}{R}\left(\left(\frac{\partial\psi}{\partial R}\right)^2 + \left(\frac{\partial\psi}{\partial Z}\right)^2\right)\xi_\phi - B_{0\phi}\frac{\partial\psi}{\partial s}\cos\vartheta\xi_Z\right] \\
&= \frac{1}{R}\xi_\phi - \frac{B_{0\phi}}{|\boldsymbol{\nabla}\psi|^2}\frac{\partial\psi}{\partial s}\xi_\vartheta \ . \qquad (2.124)
\end{aligned}$$

Both R and $B_{0\phi}$ are finite and non-zero over the plasma domain and in the limit $s \to 0$ then $\xi_\wedge \sim \xi_\vartheta/s$. For $|m| = 1$ this would suggest that $\xi_\wedge \to \infty$ at the magnetic axis, due to the geometric singularity. This singularity is lifted when we consider the modified variable $\tilde{\xi}_\vartheta = \frac{|\boldsymbol{\nabla}\psi|}{B_0}\xi_\wedge$:

$$\tilde{\xi}_\wedge = \frac{|\boldsymbol{\nabla}\psi|}{R}\xi_\phi - \frac{B_{0\phi}}{|\boldsymbol{\nabla}\psi|}\frac{\partial\psi}{\partial s}\xi_\vartheta \ . \qquad (2.125)$$

The first term is proportional to s for all values of m. The second term is proportional to s for $|m| \neq 1$ and is a finite constant for $|m| = 1$. Therefore $\tilde{\xi}_\wedge$ follows the same boundary conditions as ξ_ϑ at the magnetic axis. We summarize the boundary conditions at the magnetic axis as:

$$\begin{aligned}
&\tilde{\xi}_\perp = 0 \ , \ \tilde{\xi}_\wedge = 0 \ , \ m = 0 \ , \\
&\tilde{\xi}_\perp = 0 \ , \ \frac{\partial\tilde{\xi}_\wedge}{\partial s} = 0 \ , \ |m| = 1 \ , \\
&\tilde{\xi}_\perp = 0 \ , \ \tilde{\xi}_\wedge = 0 \ , \ |m| \geq 2 \ . \qquad (2.126)
\end{aligned}$$

2.5.2 Outer Wall

Since there is no vacuum region the outer boundary of the computational plasma domain is taken to be a particular flux surface (usually the last closed flux surface) of the plasma equilibrium found from solving the Grad-Shafranov equation. This is the "reactor wall". We assume that this wall is perfectly conducting and that

there is no particle flux through the wall. This is not a realistic scenario as a typical tokamak will have a vacuum region in the vacuum vessel and there will be some plasma that hits and recombines with the wall, as well as impurities that enter the plasma from the wall. However, for our purposes this is acceptable as we are aiming to study small amplitude CAEs, as per our linearisation. The conditions of a perfectly conducting solid wall can be written as [26]:

$$\mathbf{n} \cdot \boldsymbol{\xi} = 0 \ , \tag{2.127}$$

$$\mathbf{n} \cdot \mathbf{B} = 0 \ , \tag{2.128}$$

where $\mathbf{n}$ is the normal to the wall and is parallel to $\boldsymbol{\nabla}\psi$ at the last closed flux surface. This implies that $\tilde{\xi}_{\perp} = 0$ at the outer boundary. Then $\mathbf{n} \cdot \mathbf{B} = 0$ follows directly from Eq. (2.40).

This choice of boundary condition at the wall preserves the quantities of magnetic flux, energy, mass and momentum [26]. This is important for studying the effect of the Hall-term on CAE modes as keeping the system as simple as possible means the physics of the CAEs can be studied without the 'noise' of outside phenomena.

Chapter 3

Methodology

In order to solve the Hall-MHD wave equations (2.90) and (2.91) we opt to solve for a discrete approximation to the continuous function $\boldsymbol{\xi}$. In order to discretise the PDEs we employ the *finite elements* method radially and *spectral methods* in the angular directions.

3.1 Finite Elements

For the radial direction ($\boldsymbol{\nabla}\psi$) we use finite elements analysis [23, 47, 48]. Finite elements first requires that a finite set of points, or nodes, is chosen in the space of the independent variables. For example in a 1-d space suppose the domain is $[x_{min}, x_{max}]$ and we choose a set of $n_r + 1$ points $\{x_i\}_{i=0}^{n_r} \in [x_{min}, x_{max}]$, where $x_0 = x_{min}$, $x_{n_r} = x_{max}$ and $x_i < x_{i+1}$. The intervals $[x_{i-1}, x_{i+1}]$ (appropriately truncated at the domain boundary) are then the so-called elements. The dependant variables, or field values, are then approximated by a weighted sum of piecewise polynomials. These polynomials are localised to a particular element with at least one piecewise polynomial for each different element. Suppose, for brevity, we're looking to solve the homogeneous ODE: $F(y(x)) = 0$ (the method can easily be extended to include non-homogeneous ODEs). We define an approximate solution $y^{(N)}(x) = \sum_{j=0}^{N-1} y_j H_j(x)$ where N is the number of local polynomials in the approximation. The integer N depends on the choice of finite elements scheme and is a strictly increasing function of n_r. The *basis functions* $H_j(x)$ are piecewise polynomials local to a specific element and zero everywhere else. The weights y_j are related to the approximate function $y^{(N)}(x)$ as values of the function, or values of the function's derivative, at a specific point within the element to which H_j is localised (usually the central gridpoint x_j). Finite elements is similar to the method of *finite differences*, but whereas the

continuous variables in finite elements are approximated by a discrete set of basis functions with local support, in finite differences the variables are approximated by a discrete set of values at the gridpoints.

In order to solve the ODE $F(y(x)) = 0$ numerically we seek to minimise the absolute value of the *residual*, defined as $r^{(N)}(x) := F(y(x)) - F(y^{(N)}(x)) = F(y^{(N)}(x))$, across all $x \in [x_{min}, x_{max}]$. It is clearly desirable that $r^{(N)}(x) \to 0$ as $n_r \to \infty$ for all x in the domain. To solve for the unknown values y_j we specify that a set of weighted integrals of the residual are each equal to zero:

$$\int_{x_{min}}^{x_{max}} w_j \; r^{(N)} dx = 0 \quad , \quad \forall j. \tag{3.1}$$

Upon specification of the weight functions $w_j(x)$ this creates a set of linear equations that can be solved for y_j. In the *Galerkin* scheme the weight functions are chosen to be the same as the basis functions. This choice implies that the basis functions are orthogonal to the residual for the inner product defined by $\int_{x_{min}}^{x_{max}} H_j(x) \; r^{(N)}(x) dx$.

We also employ the *weak formulation* of the problem whereby an integration by parts is performed to lower the order of a derivative term in the ODE $F(y)$. The derivative is shifted onto the weight function [23]. This allows for solutions that have a lower order of differentiability, increasing the size of the possible solution space. For the Hall-MHD equations (2.90)-(2.91) there are second order differentials in the radial direction, meaning the solution must be at least twice differentiable in the radial variable. In the weak formulation the solution only needs to be once differentiable in the radial variable. Eq. (3.1) can be represented in matrix form $\underline{\underline{\mathcal{A}}} \cdot \boldsymbol{y}^{(N)} = \mathbf{0}$. Now $\boldsymbol{y}^{(N)} = (y_0, y_1, ..., y_N)$ and $\mathcal{A}_{ij} = \int_{x_{min}}^{x_{max}} H_i F(H_j) dx$ with $\underline{\underline{\mathcal{A}}}$ an $N \times N$ matrix. This system of equations can then be solved by standard methods.

We impose the radial boundary conditions of the physical system on the linear system of equations. The boundary conditions of the perfectly conducting wall and the magnetic axis can be categorised into two different types. A 'Dirichlet' type boundary condition occurs when the function value is fixed on the boundary, for example $y(0) = 0$. In finite elements problems these are called *essential boundary conditions* as they must be explicitly applied to the model. In practice this means removing those basis functions which do not satisfy the boundary condition, effectively setting rows of the system matrix to zero. 'Neumann' type boundary conditions involve specifying functional derivatives at the boundary. In finite elements these are termed *natural boundary conditions* and in the weak formulation they can usually be imposed on the surface terms arising from the by-parts integration. In practice this does not happen in Whales2 as the surface terms are all forced to zero

when the essential boundary conditions are imposed, and we do not impose the natural boundary conditions in any additional way.

Choosing basis functions

The function space that is chosen for our basis functions can be characterised as a space of local piecewise polynomials of a given degree of differentiability. Gruber and Rappaz offer the notation S_p^d for the functional spaces to which the approximate solutions of the finite elements analysis belong [49]. The function $y^{(N)}(x) \in S_p^d$ will have the following properties: $y^{(N)}$ is $d-1$ times continuously differentiable across the whole domain, where $d = 1$ implies that $y^{(N)}$ is continuous but not necessarily differentiable, and $d = 0$ does not impose continuity. $y^{(N)}$ is also a piecewise polynomial of order p on restriction to each interval $[x_i, x_{i+1}]$. The details of how to construct a basis for S_p^d are well explained in [49]. Example bases are shown in Fig. 3.1.

The basis functions currently available in Whales2 are chosen to have the highest order of differentiability that is permitted for a basis of a particular polynomial order, i.e. the bases in Whales2 form the spaces S_0^0, S_1^1, S_2^1, S_3^2, S_4^2 which we refer to as the *constant*, *linear*, *quadratic*, *cubic* and *quartic* bases respectively. The approximate solutions using these bases can be written as follows:

$$\text{Constant} : \xi^{(N)} = \sum_{i=0}^{n_r-1} \xi_{i+\frac{1}{2}} H_i \ , \tag{3.2}$$

$$H_i(x) = \begin{cases} 1 & x \in [x_i, x_{i+1}] \ , \\ 0 & x \notin [x_i, x_{i+1}] \ . \end{cases}$$

$$\text{Linear} : \xi^{(N)} = \sum_{i=0}^{n_r} \xi_i H_i \ , \tag{3.3}$$

$$H_i(x) = \begin{cases} \frac{x-x_{i-1}}{x_i-x_{i-1}} & x \in [x_{i-1}, x_i] \ , \\ \frac{x_{i+1}-x}{x_{i+1}-x_i} & x \in [x_i, x_{i+1}] \ , \\ 0 & x \notin [x_{i-1}, x_{i+1}] \ . \end{cases}$$

$$\text{Quadratic}: \ \xi^{(N)} = \sum_{i=0}^{n_r} \xi_i H_i^1 + \sum_{i=0}^{n_r-1} \xi_{i+\frac{1}{2}} H_i^2 \ , \tag{3.4}$$

$$H_i^1(x) = \begin{cases} \frac{(2x-x_i-x_{i-1})(x_i-x)}{(x_i-x_{i-1})^2} & x \in [x_{i-1}, x_i] \ , \\ \frac{(2x-x_{i+1}-x_i)(x-x_{i+1})}{(x_{i+1}-x_i)^2} & x \in [x_i, x_{i+1}] \ , \\ 0 & x \notin [x_{i-1}, x_{i+1}] \ , \end{cases}$$

$$H_i^2(x) = \begin{cases} \frac{4(x-x_i)(x_{i+1}-x)}{(x_{i+1}-x_i)^2} & x \in [x_i, x_{i+1}] \\ 0 & x \notin [x_i, x_{i+1}] \end{cases}$$

$$\text{Cubic}: \ \xi^{(N)} = \sum_{i=0}^{n_r} \xi_i H_i^1 + \sum_{i=0}^{n_r} \xi_i' H_i^2 \ , \tag{3.5}$$

$$H_i^1(x) = \begin{cases} \frac{(x-x_{i-1})^2(3x_i-x_{i-1}-2x)}{(x_i-x_{i-1})^3} & x \in [x_{i-1}, x_i] \ , \\ \frac{(x_{i+1}-x)^2(x_{i+1}-3x_i+2x)}{(x_{i+1}-x_i)^3} & x \in [x_i, x_{i+1}] \ , \\ 0 & x \notin [x_{i-1}, x_{i+1}] \ , \end{cases}$$

$$H_i^2(x) = \begin{cases} \frac{(x-x_{i-1})^2(x-x_i)}{(x_i-x_{i-1})^2} & x \in [x_{i-1}, x_i] \ , \\ \frac{(x_{i+1}-x)^2(x-x_i)}{(x_{i+1}-x_i)^2} & x \in [x_i, x_{i+1}] \ , \\ 0 & x \notin [x_{i-1}, x_{i+1}] \ , \end{cases}$$

$$\text{Quartic}: \ \xi^{(N)} = \sum_{i=0}^{n_r} \xi_i H_i^1 + \sum_{i=0}^{n_r} \xi_i' H_i^2 + \sum_{i=0}^{n_r-1} \xi_{i+\frac{1}{2}} H_i^3 \ , \tag{3.6}$$

$$H_i^1(x) = \begin{cases} \frac{(x-x_{i-1})^2(x_{i-1}^2-4x_ix_{i-1}-5x_i^2-2x_{i-1}x+14x_ix-8x^2)}{(x_i-x_{i-1})^4} & x \in [x_{i-1}, x_i] \ , \\ \frac{(x_{i+1}-x)^2(x_{i+1}^2-4x_ix_{i+1}-5x_i^2+2x_{i+1}x+14x_ix-8x^2)}{(x_{i+1}-x_i)^4} & x \in [x_i, x_{i+1}] \ , \\ 0 & x \notin [x_{i-1}, x_{i+1}] \ , \end{cases}$$

$$H_i^2(x) = \begin{cases} \frac{(x_{i-1}+x_i-2x)(x_i-x)(x_{i-1}-x)^2}{(x_i-x_{i-1})^3} & x \in [x_{i-1}, x_i] \ , \\ \frac{(x_{i+1}+x_i-2x)(x-x_i)(x_{i+1}-x)^2}{(x_{i+1}-x_i)^3} & x \in [x_i, x_{i+1}] \ , \\ 0 & x \notin [x_{i-1}, x_{i+1}] \ , \end{cases}$$

$$H_i^3(x) = \begin{cases} \frac{16(x-x_i)^2(x_{i+1}-x)^2}{(x_{i+1}-x_i)^4} & x \in [x_i, x_{i+1}] \\ 0 & x \notin [x_i, x_{i+1}] \ . \end{cases}$$

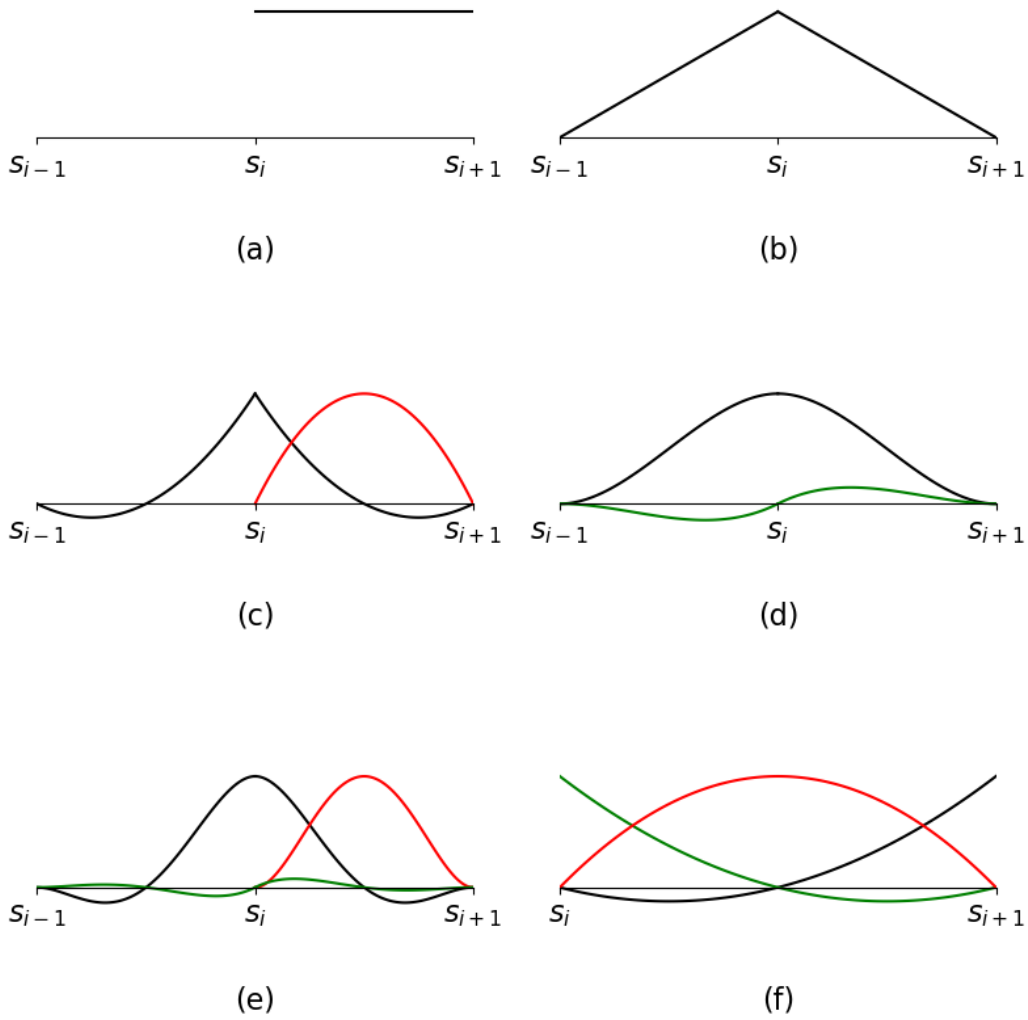

Figure 3.1: Figures (a) - (e) show the full bases within the spaces S_0^0, S_1^1, S_2^1, S_3^2, S_4^2 which are employed by the Whales2 code. These particular elements are chosen such that they have the highest order of differentiability allowed within the constraints imposed on a finite elements basis. Figure (f) shows the bases in S_2^1 decomposed into three *shape functions* restricted to a particular grid-cell. The bases can then be thought of as unions of these shape functions.

Spectral pollution

Since the Hall-MHD formulation (2.90)-(2.91) has two variables $\tilde{\xi}_\perp, \tilde{\xi}_\wedge$ there are two independent choices of basis for the finite elements analysis. However, most choices will lead to *spectral pollution* and so must be avoided. Take the model eigenvalue problem $\underline{\underline{\mathcal{A}}} \cdot \boldsymbol{x} = \Lambda \boldsymbol{x}$ and suppose finite elements analysis produces approximate solutions $(\boldsymbol{x}_i, \lambda_i)_{i=0}^N$. Spectral pollution describes a phenomenon where in the limit $n_r \to \infty$ (i.e. vanishingly small grid spacing) the limit $\lim_{n_r \to \infty} \lambda_i = \Lambda_i$ is not a solution of the original system [49]. Alternatively each individual eigenvalue may converge as $n \to \infty$ but the system as a whole does not converge [50], i.e. $\max_i |\lambda_i - \Lambda_i|$ does not converge.

Spectral pollution is associated with systems that have an accumulation point, an infinitely degenerate eigenvalue or a continuous spectrum [49]. The ideal-MHD equations usually have two associated continuous spectra - the shear Alfvén continuum and the slow continuum. In the case of a homogeneous ideal-MHD equilibrium these continua become infinitely degenerate points in frequency-space. The assumption of zero plasma-β eliminates the slow spectrum. The shear Alfvén modes are typically lower frequency than the CAEs, but good representation of the Alfvén continuum is important for the following reasons. Firstly, since the CAEs couple to the Alfvén continuum via resonant absorption then a poor representation of the Alfvén spectrum may lead to spurious coupling and hinder strategies to calculate 'pure' CAEs. Also, spurious modes clutter calculated spectra making it harder to analyse results and so should be avoided as a matter of course. The Hall-MHD equations also form a continuum of shear Alfvén modes in the limit of zero plasma-β. Inclusion of the Hall term and non-zero plasma pressure, however, transforms this continuum into a set of discrete modes [51].

Pollution can arise when a given physical condition cannot be sufficiently fulfilled across the domain. In the case of the Alfvén spectrum in ideal-MHD one particular condition of interest has been identified as $\boldsymbol{\nabla} \cdot \boldsymbol{\xi} = 0$ [52, 53]. In the simple case of a homogeneous θ-pinch, with cylindrical co-ordinates (r, θ, z), the Alfvén modes are clustered at the infinitely degenerate point where:

$$\omega_A^2 = \frac{k^2 B_0^2}{\rho_0} \ . \tag{3.7}$$

The wavenumber $k = \boldsymbol{k} \cdot \hat{z}$ is the cylindrical analogue of the toroidal wavenumber n. These Alfvén modes are incompressible, i.e. $\boldsymbol{\nabla} \cdot \boldsymbol{\xi} = 0$, across the whole domain. Given the cylindrical geometry then the expression for incompressibility can be

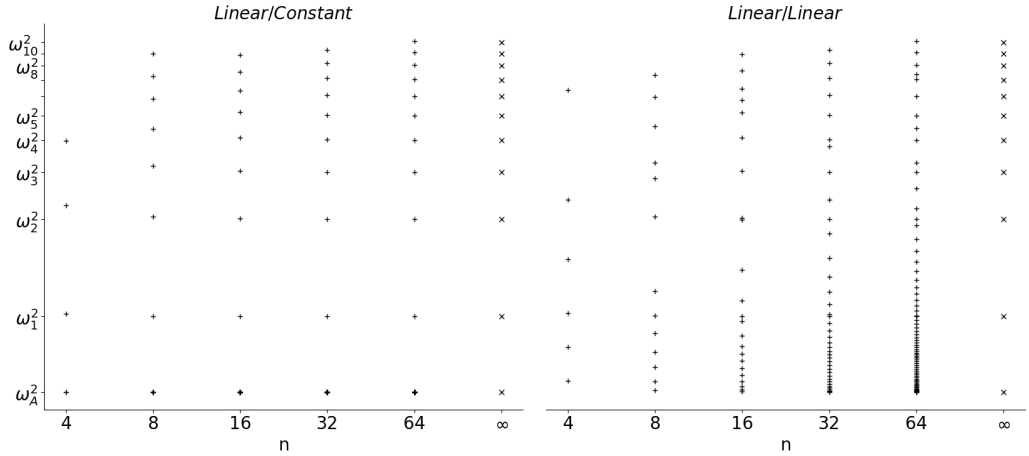

Figure 3.2: Both figures show the output frequencies (+) from Whales2 for a given equilibrium against increasing radial resolution, with the analytically known frequencies (x) at perfect resolution "$n_r = \infty$". The left figure uses linear-constant basis elements and shows a clear convergence to the known solutions. The figure on the right uses a linear-linear basis, which is higher order overall than the left figure but produces much worse convergence. The poorly represented shear Alfvén modes can be seen scattered across the whole range of frequencies.

expanded as:

$$\boldsymbol{\nabla} \cdot \boldsymbol{\xi} = \frac{1}{r}\frac{\partial(r\xi_r)}{\partial r} + \frac{im}{r}\xi_\theta = 0 \ , \tag{3.8}$$

since $\xi_z = 0$ for this particular set of solutions [52] and only a single Fourier harmonic in the poloidal direction is necessary. The variables employed by Whales2 become in this regime $\tilde{\xi}_\perp \to r\xi_r,\ \tilde{\xi}_\wedge \to \xi_\theta,\ s \sim r$.

Suppose $\tilde{\xi}_\perp, \tilde{\xi}_\wedge$ belong to the space of local piecewise linear functions that are continuous over the whole domain, S_1^1. Then Eq. (3.8) cannot be satisfied everywhere. $\partial_s\tilde{\xi}_\perp$ is a piecewise constant (discontinuous) function in s whilst $\tilde{\xi}_\wedge$ is piecewise linear, so the only way to impose incompressibility across all the grid cells is to set each to zero. Therefore the Alfvén spectrum will not be well represented by such a scheme and searching for non-trivial solutions will violate condition (3.8), producing spurious solutions.

This can be formulated in terms of dimensions and constraints. For a scheme in which piecewise linear functions are employed there are $2(n_r + 1)$ nodal values so this is the dimension of the system. Suppose $|m| \neq 1$, for brevity. There are three constraints from the boundary conditions. Further, the condition (3.8) adds $2(n_r - 1) + 1$ constraints, after the application of boundary conditions, since $\tilde{\xi}_\perp$

and $\tilde{\xi}_\wedge$ must be individually constrained to ensure $\boldsymbol{\nabla} \cdot \boldsymbol{\xi} = 0$ over each grid cell. Therefore, the total number of constraints is $2(n_r + 1)$, equal to the dimension of the system and so no solutions satisfying (3.8) are allowed [52]. Bases of higher order polynomials may allow a handful of such solutions. A non-polluting choice is $\tilde{\xi}_\perp \in S_1^1$ and $\tilde{\xi}_\wedge \in S_0^0$ so that each term in Eq. (3.8) is piecewise constant. The incompressibility can be satisfied everywhere whilst $\boldsymbol{\xi} \neq \mathbf{0}$. This is because the incompressibility condition now only applies n_r constraints on the space of (slightly lower) dimension $2n_r + 1$. There are now two applicable boundary conditions, so overall there are $n_r - 1$ possible solutions that can satisfy (3.8).

In the weak formulation of the ideal-MHD wave equations, the $\tilde{\xi}_\perp$ displacement component may be subject to first-order radial derivatives whereas $\tilde{\xi}_\wedge$ is not subject to any radial derivatives. This relationship in the order of derivatives naturally suggests that $\tilde{\xi}_\perp$ should be approximated with a functional dependence on the radial co-ordinate, s, of exactly one order higher than that of $\tilde{\xi}_\wedge$. Therefore we extend the principle set out above, that suppresses spectral pollution in a homogeneous θ-pinch, and apply it to all equilibrium configurations when solving the ideal-MHD wave equations. We refer to the order of a particular finite elements scheme in the form *perp-wedge*, for example if $\tilde{\xi}_\perp \in S_1^1$ and $\tilde{\xi}_\wedge \in S_0^0$ then we would call this choice of basis function *linear-constant*.

Spectral pollution has also been found to occur in MHD linear stability codes that use a 2-dimensional finite elements approach in the radial and poloidal directions, even though the basis functions are chosen so that the incompressibility condition (3.8) can be satisfied [54]. The pollution was determined to stem from the operator $(\boldsymbol{B}_0 \cdot \boldsymbol{\nabla})$ which could not vanish exactly on a singular surface with the particular finite elements implementation. This prompted the proposal of *finite hybrid elements* in which the variables of the system and their derivatives are considered as independent variables [55]. Note that this is only applied to derivatives in the directions where finite elements analysis is employed. In this manner finite hybrid elements should be considered as an extension of the basis matching described above, where now each variable and their derivatives are chosen to have the same functional dependence. For example, in the case of the ideal-MHD setup above we expand the set of variables from $(\tilde{\xi}_\perp, \tilde{\xi}_\wedge)$ to $(\partial_s \tilde{\xi}_{\perp 1}, \tilde{\xi}_{\perp 2}, \tilde{\xi}_\wedge)$. Then we choose, say, $\tilde{\xi}_{\perp 1} \in S_1^1$ and $\tilde{\xi}_{\perp 2}, \tilde{\xi}_\wedge \in S_0^0$ so that, after the radial derivative is applied, each variable is approximated by a discontinuous constant basis. Integral conditions are applied to relate each variable to its derivatives [49, 55]. The condition that must

be satisfied is [49]:

$$\int_{x_{min}}^{x_{max}} \left(\tilde{\xi}_{\perp 1} - \tilde{\xi}_{\perp 2}\right) w(x) dx = 0 \quad \forall w \in S \ , \tag{3.9}$$

where here S is the space of all piecewise polynomial functions on the domain $[x_{min}, x_{max}]$. For the example bases chosen we only need consider $w \in S_0^0$ to get the necessary relation between the nodal values. $\tilde{\xi}_{\perp 1} = \sum_{i=0}^{n_r} \xi_{\perp,i} H_i^{LN}$ and $\tilde{\xi}_{\perp 2} = \sum_{i=0}^{n_r} \xi_{\perp,i+\frac{1}{2}} H_i^{CN}$ as defined by (3.2)-(3.3) respectively. We look at the restriction of Eq. (3.9) to a particular grid-cell, say $[x_i, x_{i+1}]$, from which the relation emerges:

$$\xi_{\perp,i+\frac{1}{2}} = \frac{\xi_{\perp,i+1} + \xi_{\perp,i}}{2} \ . \tag{3.10}$$

We use this to make the substitution to eliminate $\xi_{\perp,i+\frac{1}{2}}$ in favour of $\xi_{\perp,i}$.

We have found finite hybrid elements to often give better results than regular finite elements when applied to the Hall-MHD perturbations. This is likely because due to the introduction of radial derivatives acting on $\tilde{\xi}_\wedge$, which means that if we apply the non-polluting schemes for the incompressibility condition there is now a two-order difference between the radial polynomials for the variables $\tilde{\xi}_\perp$ and $\partial_s \tilde{\xi}_\wedge$. Hybrid elements allows us to choose the same functional dependence for $\tilde{\xi}_\perp$, $\partial_s \tilde{\xi}_\perp$, $\tilde{\xi}_\wedge$, $\partial_s \tilde{\xi}_\wedge$.

3.2 Spectral Methods

Spectral methods work similarly to the finite elements method. The domain is discretized and the solution is approximated by a weighted sum of functions. In this case the functions used are global functions on the domain of interest. This is particularly useful when these global functions satisfy a desired property of the exact solution. Spectral methods are applied in the direction of the poloidal and toroidal angles where the geometry 2π-periodic and so the solutions are 2π-periodic also. Therefore we approximate the solution using a truncated Fourier series as each Fourier harmonic satisfies the periodicity property.

In the toroidal direction the system is symmetric and so only a single Fourier harmonic is required as there is no toroidal coupling. In the poloidal direction the solution is approximated by the truncated series

$$y(\vartheta) \simeq y^{(M)}(\vartheta) = \sum_{k=m-M}^{m+M} y_k e^{ik\vartheta} \ , \tag{3.11}$$

where m is any integer. As with finite elements we aim to minimise the residual (c.f. Eq. (3.1)), though now over the interval $[0, 2\pi]$. The weight functions are chosen to be the complex conjugates of the basis functions and so we can use the orthogonality relation:

$$\int_0^{2\pi} e^{i(k-l)\vartheta} d\vartheta = 2\pi\delta_{kl} \ . \tag{3.12}$$

Again a linear system is set up $\underline{\underline{A}} \cdot \boldsymbol{y}^{(M)} = \boldsymbol{0}$ with $A_{kl} = F_{(k-l)}$, the $(k-l)^{th}$ Fourier harmonic of $F(y_l)$.

3.3 Code Elements

Applying the finite elements and spectral methods to discretise the Hall-MHD equations (2.90)-(2.91) means that there two residuals to minimise, one for each equation:

$$\begin{aligned} r_\perp^{NM} =& -2s\frac{\mu_0\rho_0}{\mathcal{J}g^{\psi\psi}}\frac{\partial^2\tilde{\xi}_\perp^{NM}}{\partial t^2} + \tilde{\mathcal{G}}_\perp\left(\tilde{\xi}_\perp^{NM}, \tilde{\xi}_\wedge^{NM}\right) \\ &+ H\frac{\partial}{\partial t}\tilde{\mathcal{G}}_\perp\left(\mathcal{J}\frac{|\boldsymbol{\nabla}\psi|}{B_0}\tilde{\xi}_\wedge^{NM}, -\frac{1}{\mathcal{J}B_0|\boldsymbol{\nabla}\psi|}\tilde{\xi}_\perp^{NM}\right) \ , \end{aligned} \tag{3.13}$$

$$\begin{aligned} r_\wedge^{NM} =& -2s\mathcal{J}\mu_0\rho_0\frac{\partial^2\tilde{\xi}_\wedge^{NM}}{\partial t^2} + \tilde{\mathcal{G}}_\wedge\left(\tilde{\xi}_\perp^{NM}, \tilde{\xi}_\wedge^{NM}\right) \\ &+ H\frac{\partial}{\partial t}\tilde{\mathcal{G}}_\wedge\left(\mathcal{J}\frac{|\boldsymbol{\nabla}\psi|}{B_0}\tilde{\xi}_\wedge^{NM}, -\frac{1}{\mathcal{J}B_0|\boldsymbol{\nabla}\psi|}\tilde{\xi}_\perp^{NM}\right) \ . \end{aligned} \tag{3.14}$$

The discretised displacement components are each given by the expression:

$$\tilde{\xi}_{\perp/\wedge}^{NM} = \sum_{l=m-M}^{m+M}\sum_{j=0}^{n_r}\hat{\xi}_{\perp/\wedge}^{jl}H_{\perp/\wedge}^{j}(s)e^{i(l\vartheta+n\phi-\omega t)} \ , \tag{3.15}$$

We assume, for clarity of illustration, that we are using a linear-linear system of shape functions and we ignore boundary conditions, meaning that each displacement component has exactly one associated variable per radial node. This gives the radial system size as $N = 2(n_r + 1)$, where n_r is the number of radial nodes (not to be confused with toroidal mode number n). $H_{\perp/\wedge}^{j}(s)$ refers to the basis function centered on the jth node for either the $\perp$ or $\wedge$ displacement component. The residuals must each satisfy:

$$\int_{\boldsymbol{V}} e^{-ik\vartheta}H_{\perp/\wedge}^{h}(s)r_{\perp/\wedge}^{NM}\, d\boldsymbol{V} = 0 \ , \quad \forall k, h \ . \tag{3.16}$$

where $\boldsymbol{V}$ is the plasma volume so that:

$$\int_{\boldsymbol{V}} d\boldsymbol{V} = \frac{1}{(2\pi)^2} \int_0^{2\pi} \int_0^{2\pi} \int_{s_{min}}^{s_{max}} ds d\vartheta d\phi \ . \tag{3.17}$$

This gives a set of linear equations to be solved for the coefficients $\hat{\xi}^{jl}_{\perp/\wedge}$ and can be represented in a matrix format. We solve for normal modes of the Hall-MHD wave equation for which the displacement has a temporal dependency of the form:

$$\boldsymbol{\xi}(\boldsymbol{r}, t) = \boldsymbol{\xi}(\boldsymbol{r})\, e^{-i\omega t} \ . \tag{3.18}$$

The equations Eq. (3.16) can then be written:

$$\left(\omega^2 \underline{\underline{\mathcal{I}}} + \omega \underline{\underline{\mathcal{H}}} + \underline{\underline{\mathcal{F}}}\right) \cdot \boldsymbol{\xi}^{NM} = \boldsymbol{0} \ , \tag{3.19}$$

where

$$\boldsymbol{\xi}^{NM} = \left(\hat{\xi}^{0(m-M)}_{\perp}, \hat{\xi}^{0(m-M)}_{\wedge}, \ldots, \hat{\xi}^{n_r(m+M)}_{\perp}, \hat{\xi}^{n_r(m+M)}_{\wedge}\right) \ . \tag{3.20}$$

Eq. (3.19) has the form of a generalised eigenvalue problem and can be solved by standard numerical methods. The matrices $\underline{\underline{\mathcal{I}}}$, $\underline{\underline{\mathcal{H}}}$, $\underline{\underline{\mathcal{F}}}$ correspond to the *inertial*, *Hall* and *force* terms respectively. Each matrix can be split up into blocks that correspond to each Fourier harmonic. Within each of these blocks we iterate over the radial basis functions. So the overall matrix is a $(2M+1) \times (2M+1)$ block matrix and each block is $N \times N$ in size (note that N depends on the boundary conditions and the choice of finite element shape functions). We denote the $(h, j)^{th}$ element of the $(k, l)^{th}$ block of matrix $\underline{\underline{\mathcal{A}}}$ by $\mathcal{A}^{kl}_{hj}$.

$$\underline{\underline{\mathcal{A}}} = \begin{pmatrix} \underline{\underline{\mathcal{M}}}_{00} & \underline{\underline{\mathcal{M}}}_{01} & \cdots & \underline{\underline{\mathcal{M}}}_{0(2M)} \\ \underline{\underline{\mathcal{M}}}_{10} & \underline{\underline{\mathcal{M}}}_{11} & \cdots & \underline{\underline{\mathcal{M}}}_{1(2M)} \\ \cdots & & & \\ \underline{\underline{\mathcal{M}}}_{(2M)0} & \underline{\underline{\mathcal{M}}}_{(2M)1} & \cdots & \underline{\underline{\mathcal{M}}}_{(2M)(2M)} \end{pmatrix} \tag{3.21}$$

$$\underline{\underline{\mathcal{M}}}_{kl} = \begin{pmatrix} \mathcal{A}^{kl}_{00} & \mathcal{A}^{kl}_{01} & \cdots & \mathcal{A}^{kl}_{0(N-1)} \\ \mathcal{A}^{kl}_{10} & \mathcal{A}^{kl}_{11} & \cdots & \mathcal{A}^{kl}_{1(N-1)} \\ \cdots & & & \\ \mathcal{A}^{kl}_{(N-1)0} & \mathcal{A}^{kl}_{(N-1)1} & \cdots & \mathcal{A}^{kl}_{(N-1)(N-1)} \end{pmatrix} \tag{3.22}$$

$$\mathcal{A}^{kl}_{\tilde{h}\tilde{j}} = \int_{\boldsymbol{V}} e^{-i(k\vartheta + n\phi)} H^h_\alpha(s) A_{\alpha\beta} \left(H^j_\beta(s) e^{i(l\vartheta + n\phi)}\right) d\boldsymbol{V} \ . \tag{3.23}$$

Here we have used $\tilde{h}$ and $\tilde{j}$ where:

$$h = \begin{cases} \tilde{h}/2 & \tilde{h} \text{ even} \\ (\tilde{h}-1)/2 & \tilde{h} \text{ odd} \end{cases} \tag{3.24}$$

and similarly for j, so that $\tilde{h}, \tilde{j} \in \{0, \ldots, N-1\}$ and $h, j \in \{0, \ldots, n_r\}$. So if $\tilde{h}/\tilde{j}$ is even then it refers to a weight/basis function $H_\perp$ and $\tilde{h}/\tilde{j}$ odd refers to $H_\wedge$, as per the even-odd pattern in Eq. (3.20). $A_{\alpha\beta}(\bullet)$ is an operator that denotes the relevant part of the residual, Eqs. (3.13)-(3.14), that contributes to the matrix $\underline{\underline{\mathcal{A}}}$, where $\alpha, \beta \in \{\perp, \wedge\}$. So $\alpha = \perp$ if $\tilde{h}$ is even and $\alpha = \wedge$ if $\tilde{h}$ is odd (similarly with β and $\tilde{j}$). For each matrix, the integrand operators can be split up:

$$I_{\perp\perp}(\bullet) = 2s\frac{\mu_0\rho_0}{\mathcal{J}g^{\psi\psi}}\bullet \ , \tag{3.25}$$

$$I_{\wedge\wedge}(\bullet) = 2s\mathcal{J}\mu_0\rho_0\bullet \ , \tag{3.26}$$

$$H_{\perp\perp}(\bullet) = iH\tilde{\mathcal{G}}_\perp\left(0, \frac{1}{\mathcal{J}B_0|\boldsymbol{\nabla}\psi|}\bullet\right) \ , \tag{3.27}$$

$$H_{\perp\wedge}(\bullet) = -iH\tilde{\mathcal{G}}_\perp\left(\mathcal{J}\frac{|\boldsymbol{\nabla}\psi|}{B_0}\bullet, 0\right) \ , \tag{3.28}$$

$$H_{\wedge\perp}(\bullet) = iH\tilde{\mathcal{G}}_\wedge\left(0, \frac{1}{\mathcal{J}B_0|\boldsymbol{\nabla}\psi|}\bullet\right) \ , \tag{3.29}$$

$$H_{\wedge\wedge}(\bullet) = -iH\tilde{\mathcal{G}}_\wedge\left(\mathcal{J}\frac{|\boldsymbol{\nabla}\psi|}{B_0}\bullet, 0\right) \ , \tag{3.30}$$

$$F_{\perp\perp}(\bullet) = \tilde{\mathcal{G}}_\perp(\bullet, 0) \ , \tag{3.31}$$

$$F_{\perp\wedge}(\bullet) = \tilde{\mathcal{G}}_\perp(0, \bullet) \ , \tag{3.32}$$

$$F_{\wedge\perp}(\bullet) = \tilde{\mathcal{G}}_\wedge(\bullet, 0) \ , \tag{3.33}$$

$$F_{\wedge\wedge}(\bullet) = \tilde{\mathcal{G}}_\wedge(0, \bullet) \ . \tag{3.34}$$

To illustrate, if $\tilde{h}$ and $\tilde{j}$ are both even then:

$$\mathcal{I}^{kl}_{\tilde{h}\tilde{j}} = e^{-i\omega t}\int_{\boldsymbol{V}} e^{i(l-k)\vartheta}H^h_\perp(s)2s\frac{\mu_0\rho_0}{\mathcal{J}g^{\psi\psi}}H^j_\perp(s)d\boldsymbol{V} \ . \tag{3.35}$$

In order to fully write out the functions that form the matrices, we further separate these functions into whether radial derivatives are applied to the weight/basis function. This allows us to denote where we have applied the integration by parts required to achieve the weak Galerkin form. We write $A_{\alpha\beta} = \bar{A}_{\alpha'\beta'} + \bar{A}_{\alpha'\beta} + \bar{A}_{\alpha\beta'} + \bar{A}_{\alpha\beta}$ where for α' an integration by parts has been performed. The integral (3.23) be-

comes:

$$
\begin{aligned}
\mathcal{A}^{kl}_{\tilde{h}\tilde{j}} =& S + \int_{\boldsymbol{V}} e^{-i(k\vartheta+n\phi)} \frac{\mathrm{d}H^h_\alpha(s)}{\mathrm{d}s} \bar{A}_{\alpha'\beta'} \left(\frac{\mathrm{d}H^j_\beta(s)}{\mathrm{d}s} e^{i(l\vartheta+n\phi)} \right) d\boldsymbol{V} \\
&+ \int_{\boldsymbol{V}} e^{-i(k\vartheta+n\phi)} \frac{\mathrm{d}H^h_\alpha(s)}{\mathrm{d}s} \bar{A}_{\alpha'\beta} \left(H^j_\beta(s) e^{i(l\vartheta+n\phi)} \right) d\boldsymbol{V} \\
&+ \int_{\boldsymbol{V}} e^{-i(k\vartheta+n\phi)} H^h_\alpha(s) \bar{A}_{\alpha\beta'} \left(\frac{\mathrm{d}H^j_\beta(s)}{\mathrm{d}s} e^{i(l\vartheta+n\phi)} \right) d\boldsymbol{V} \\
&+ \int_{\boldsymbol{V}} e^{-i(k\vartheta+n\phi)} H^h_\alpha(s) \bar{A}_{\alpha\beta} \left(H^j_\beta(s) e^{i(l\vartheta+n\phi)} \right) d\boldsymbol{V} \ ,
\end{aligned} \tag{3.36}
$$

where S represents the collected "surface terms" associated with the by-parts integration. We list each of the integrand functions used to build the matrices Eq. (3.19):

$$
\bar{I}_{\perp\perp}(\bullet) = 2s \frac{\mu_0 \rho_0}{\mathcal{J} g^{\psi\psi}} \bullet \ , \tag{3.37}
$$

$$
\bar{I}_{\wedge\wedge}(\bullet) = 2s \mathcal{J} \mu_0 \rho_0 \bullet \ , \tag{3.38}
$$

$$
\frac{\bar{H}_{\perp'\perp}(\bullet)}{(-iH)} = g^{\psi\psi} (\boldsymbol{T} \cdot \boldsymbol{\nabla}) \frac{1}{\mathcal{J} g^{\psi\psi}} \bullet \ , \tag{3.39}
$$

$$
\begin{aligned}
\frac{\bar{H}_{\perp\perp}(\bullet)}{(-iH)} =& 2s \left\{ -\frac{g^{\psi\vartheta}}{g^{\psi\psi}} \partial_\vartheta \left(g^{\psi\psi} (\boldsymbol{T} \cdot \boldsymbol{\nabla}) \frac{1}{\mathcal{J} g^{\psi\psi}} \bullet \right) + (2\boldsymbol{\nabla}\psi \cdot \boldsymbol{\kappa})(\boldsymbol{T} \cdot \boldsymbol{\nabla}) \left(\frac{1}{\mathcal{J} g^{\psi\psi}} \bullet \right) \right. \\
& \left. - \frac{g^{\psi\psi} S - \mu_0 \mathbf{j}_0 \cdot \mathbf{B}_0}{B_0^2} (\mathbf{B_0} \cdot \boldsymbol{\nabla}) \left(\frac{1}{\mathcal{J} g^{\psi\psi}} \bullet \right) \right\} \ ,
\end{aligned} \tag{3.40}
$$

$$
\frac{\bar{H}_{\perp'\wedge'}(\bullet)}{(-iH)} = -\frac{B_0 |\nabla\psi|}{2s} \bullet \ , \tag{3.41}
$$

$$
\frac{\bar{H}_{\perp'\wedge}(\bullet)}{(-iH)} = -\frac{B_0^2}{\mathcal{J}} \partial_\psi \left(\mathcal{J} \frac{|\nabla\psi|}{B_0} \right) \bullet - \frac{B_0^2}{\mathcal{J}} \partial_\vartheta \left(\frac{g^{\psi\vartheta}}{g^{\psi\psi}} \mathcal{J} \frac{|\nabla\psi|}{B_0} \bullet \right) \ , \tag{3.42}
$$

$$
\frac{\bar{H}_{\perp\wedge'}(\bullet)}{(-iH)} = \frac{g^{\psi\vartheta}}{g^{\psi\psi}} \partial_\vartheta \left(B_0 |\nabla\psi| \bullet \right) \ , \tag{3.43}
$$

$$
\begin{aligned}
&\frac{\bar{H}_{\perp\wedge}(\bullet)}{(-iH)} = \\
&2s\left\{\frac{g^{\psi\vartheta}}{g^{\psi\psi}}\partial_\vartheta\left(\frac{B_0^2}{\mathcal{J}}\partial_\psi\left(\mathcal{J}\frac{|\nabla\psi|}{B_0}\right)\bullet+\frac{B_0^2}{\mathcal{J}}\partial_\vartheta\left(\frac{g^{\psi\vartheta}}{g^{\psi\psi}}\mathcal{J}\frac{|\nabla\psi|}{B_0}\bullet\right)+\frac{(2\boldsymbol{\nabla}\psi\cdot\boldsymbol{\kappa})B_0}{|\nabla\psi|}\bullet\right)\right. \\
&+\partial_\psi\left(\frac{(2\boldsymbol{\nabla}\psi\cdot\boldsymbol{\kappa})B_0^2}{\mathcal{J}g^{\psi\psi}}\right)\mathcal{J}\frac{|\nabla\psi|}{B_0}\bullet-\frac{(2\boldsymbol{\nabla}\psi\cdot\boldsymbol{\kappa})B_0^2}{\mathcal{J}g^{\psi\psi}}\partial_\vartheta\left(\frac{g^{\psi\vartheta}}{g^{\psi\psi}}\mathcal{J}\frac{|\nabla\psi|}{B_0}\bullet\right) \\
&-\frac{(2\boldsymbol{\nabla}\psi\cdot\boldsymbol{\kappa})^2B_0}{g^{\psi\psi}|\nabla\psi|}\bullet \\
&\left.+(\mathbf{B_0}\cdot\boldsymbol{\nabla})\left(\frac{(\boldsymbol{B_0}\cdot\boldsymbol{\nabla})\{\frac{|\nabla\psi|}{B_0}\bullet\}}{g^{\psi\psi}}\right)-\frac{S}{B_0^2}(g^{\psi\psi}S-\mu_0\mathbf{j}_0\cdot\mathbf{B}_0)\frac{|\nabla\psi|}{B_0}\bullet\right\}\ ,
\end{aligned}
\tag{3.44}
$$

$$
\begin{aligned}
\frac{\bar{H}_{\wedge\perp}(\bullet)}{(-iH)} =&2s\left\{-\mathcal{J}|\nabla\psi|B_0(\boldsymbol{T}\cdot\boldsymbol{\nabla})\left(\frac{g^{\psi\psi}}{B_0^2}(\boldsymbol{T}\cdot\boldsymbol{\nabla})\left(\frac{1}{\mathcal{J}g^{\psi\psi}}\bullet\right)\right)\right. \\
&\left.-\frac{\mathcal{J}B_0}{|\nabla\psi|}(\mathbf{B_0}\cdot\boldsymbol{\nabla})\left[\frac{g^{\psi\psi}}{B_0^2}(\mathbf{B_0}\cdot\boldsymbol{\nabla})\left(\frac{1}{\mathcal{J}g^{\psi\psi}}\bullet\right)\right]\right\}\ ,
\end{aligned}
\tag{3.45}
$$

$$
\frac{\bar{H}_{\wedge\wedge'}(\bullet)}{(-iH)} = \mathcal{J}|\nabla\psi|B_0(\boldsymbol{T}\cdot\boldsymbol{\nabla})\left(\frac{|\nabla\psi|}{B_0}\bullet\right)\ ,
\tag{3.46}
$$

$$
\begin{aligned}
\frac{\bar{H}_{\wedge\wedge}(\bullet)}{(-iH)} =&2s\left\{\mathcal{J}|\nabla\psi|B_0(\boldsymbol{T}\cdot\boldsymbol{\nabla})\left[\frac{1}{\mathcal{J}}\partial_\psi\left(\mathcal{J}\frac{|\nabla\psi|}{B_0}\right)\bullet+\frac{1}{\mathcal{J}}\partial_\vartheta\left(\frac{g^{\psi\vartheta}}{g^{\psi\psi}}\mathcal{J}\frac{|\nabla\psi|}{B_0}\bullet\right)\right.\right. \\
&\left.\left.+\frac{(2\boldsymbol{\nabla}\psi\cdot\boldsymbol{\kappa})}{|\nabla\psi|B_0}\bullet\right]-\frac{\mathcal{J}B_0}{|\nabla\psi|}(\mathbf{B_0}\cdot\boldsymbol{\nabla})\left[\frac{g^{\psi\psi}S-\mu_0\mathbf{j}_0\cdot\mathbf{B}_0}{B_0^2}\frac{|\nabla\psi|}{B_0}\bullet\right]\right\}\ ,
\end{aligned}
\tag{3.47}
$$

$$
\bar{F}_{\perp'\perp'}(\bullet) = -\frac{B_0^2}{2s\mathcal{J}}\bullet\ ,
\tag{3.48}
$$

$$
\bar{F}_{\perp'\perp}(\bullet) = -\frac{B_0^2}{\mathcal{J}}\partial_\vartheta\left(\frac{g^{\psi\vartheta}}{g^{\psi\psi}}\bullet\right)-\frac{(2\boldsymbol{\nabla}\psi\cdot\boldsymbol{\kappa})B_0^2}{\mathcal{J}g^{\psi\psi}}\bullet\ ,
\tag{3.49}
$$

$$
\bar{F}_{\perp\perp'}(\bullet) = \frac{g^{\psi\vartheta}}{g^{\psi\psi}}\partial_\vartheta\left(\frac{B_0^2}{\mathcal{J}}\bullet\right)-\frac{(2\boldsymbol{\nabla}\psi\cdot\boldsymbol{\kappa})B_0^2}{\mathcal{J}g^{\psi\psi}}\bullet\ ,
\tag{3.50}
$$

$$\bar{F}_{\perp\perp}(\bullet) = 2s\left\{\frac{g^{\psi\vartheta}}{g^{\psi\psi}}\partial_\vartheta\left(\frac{B_0^2}{\mathcal{J}}\partial_\vartheta\left(\frac{g^{\psi\vartheta}}{g^{\psi\psi}}\bullet\right) + \frac{(2\boldsymbol{\nabla}\psi\cdot\boldsymbol{\kappa})B_0^2}{\mathcal{J}g^{\psi\psi}}\bullet\right)\right.$$
$$- \frac{(2\boldsymbol{\nabla}\psi\cdot\boldsymbol{\kappa})B_0^2}{\mathcal{J}g^{\psi\psi}}\partial_\vartheta\left(\frac{g^{\psi\vartheta}}{g^{\psi\psi}}\bullet\right) - \frac{(2\boldsymbol{\nabla}\psi\cdot\boldsymbol{\kappa})^2 B_0^2}{\mathcal{J}g^{\psi\psi 2}}\bullet$$
$$\left. + (\mathbf{B_0}\cdot\boldsymbol{\nabla})\left(\frac{(\boldsymbol{B_0}\cdot\boldsymbol{\nabla})\{\frac{1}{\mathcal{J}}\bullet\}}{g^{\psi\psi}}\right) - \frac{S}{\mathcal{J}}\frac{(g^{\psi\psi}S - \mu_0\mathbf{j}_0\cdot\mathbf{B}_0)}{B_0^2}\bullet\right\}\ , \tag{3.51}$$

$$\bar{F}_{\perp'\wedge}(\bullet) = -\,g^{\psi\psi}(\boldsymbol{T}\cdot\boldsymbol{\nabla})\frac{B_0}{|\nabla\psi|}\bullet\ , \tag{3.52}$$

$$\bar{F}_{\perp\wedge}(\bullet) = 2s\left\{\frac{g^{\psi\vartheta}}{g^{\psi\psi}}\partial_\vartheta\left(g^{\psi\psi}(\boldsymbol{T}\cdot\boldsymbol{\nabla})\frac{B_0}{|\nabla\psi|}\bullet\right) - (2\boldsymbol{\nabla}\psi\cdot\boldsymbol{\kappa})(\boldsymbol{T}\cdot\boldsymbol{\nabla})\frac{B_0}{|\nabla\psi|}\bullet\right.$$
$$\left. + \frac{g^{\psi\psi}S - \mu_0\mathbf{J}_0\cdot\mathbf{B}_0}{B_0^2}(\mathbf{B_0}\cdot\boldsymbol{\nabla})\frac{B_0}{|\nabla\psi|}\bullet\right\}\ , \tag{3.53}$$

$$\bar{F}_{\wedge\perp'}(\bullet) = \mathcal{J}|\nabla\psi|B_0(\boldsymbol{T}\cdot\boldsymbol{\nabla})\frac{1}{\mathcal{J}}\bullet\ , \tag{3.54}$$

$$\bar{F}_{\wedge\perp}(\bullet) = 2s\left\{\mathcal{J}|\nabla\psi|B_0(\boldsymbol{T}\cdot\boldsymbol{\nabla})\left(\frac{1}{\mathcal{J}}\partial_\vartheta\left(\frac{g^{\psi\vartheta}}{g^{\psi\psi}}\bullet\right) + \frac{(2\boldsymbol{\nabla}\psi\cdot\boldsymbol{\kappa})}{\mathcal{J}g^{\psi\psi}}\bullet\right)\right.$$
$$\left. - \frac{\mathcal{J}B_0}{|\nabla\psi|}(\mathbf{B_0}\cdot\boldsymbol{\nabla})\left[\frac{g^{\psi\psi}S - \mu_0\mathbf{J}_0\cdot\mathbf{B}_0}{\mathcal{J}B_0^2}\bullet\right]\right\}\ , \tag{3.55}$$

$$\bar{F}_{\wedge\wedge}(\bullet) = 2s\left\{\mathcal{J}|\nabla\psi|B_0(\boldsymbol{T}\cdot\boldsymbol{\nabla})\left(\frac{g^{\psi\psi}}{B_0^2}(\boldsymbol{T}\cdot\boldsymbol{\nabla})\left(\frac{B_0}{|\nabla\psi|}\bullet\right)\right)\right.$$
$$\left. + \frac{\mathcal{J}B_0}{|\nabla\psi|}(\mathbf{B_0}\cdot\boldsymbol{\nabla})\left[\frac{g^{\psi\psi}}{B_0^2}(\mathbf{B_0}\cdot\boldsymbol{\nabla})\left(\frac{B_0}{|\nabla\psi|}\bullet\right)\right]\right\}\ . \tag{3.56}$$

The surface terms from the integration by parts are evaluated at the points $s = 0$ and $s(r = a)$ and each act on at least one of either the weight or basis function that corresponds to $H_\perp$ and is not differentiated. The boundary conditions Eqs. (2.126)-(2.127) therefore imply that all of the surface terms vanish. In order to construct these matrix elements it is necessary to perform Fourier transforms as well as numerical derivative and integration (quadrature) schemes.

Fourier transforms

Discrete Fourier Transforms (DFTs) are a standard numerical technique, covered in many texts - for example [56]. Whales2 uses the FFTW3 library [57] to perform the required DFTs on equilibrium quantities. For a quantity, say X, defined over an equally spaced poloidal grid $\{\vartheta_0, \ldots, \vartheta_{N_\vartheta - 1}\} \in [0, 2\pi]$ then denote $X_j = X(\vartheta_j)$. The DFT calculates:

$$Y_k = \sum_{j=0}^{N_\vartheta - 1} X_j e^{-i\frac{2\pi}{N_\vartheta}jk} \tag{3.57}$$

After appropriate normalisation these Y_k form the coefficients for approximating X by a truncated Fourier series, which can easily be seen from the inverse DFT:

$$X_j = \frac{1}{N_\vartheta} \sum_{k=0}^{N_\vartheta - 1} Y_k e^{i\frac{2\pi}{N_\vartheta}jk} = \frac{1}{N_\vartheta} \sum_{k=0}^{N_\vartheta - 1} Y_k e^{ik\vartheta_j} \tag{3.58}$$

with $\vartheta_j = j\frac{2\pi}{N_\vartheta}$ being the equally spaced grid in ϑ. Since $Y_{N_\vartheta - k} = Y_{-k}$ we can instead think of the sum above as being in the range $k = \{-(N_\vartheta - 1)/2, \ldots, (N_\vartheta - 1)/2\}$ for N_ϑ odd or $k = \{-(N_\vartheta/2) + 1, \ldots, N_\vartheta/2\}$ for N_ϑ even. In the even case we choose to ignore the ambiguous coefficient $Y_{-N_\vartheta/2} = Y_{N_\vartheta/2}$ after performing the DFT, so the range becomes $k = \{-(N_\vartheta/2) + 1, \ldots, (N_\vartheta/2) - 1\}$.

The equilibrium quantities used in Whales2 are all real numbers and so must correspond to a real-valued DFT, implying that $Y_k = Y_{-k}^\dagger$ where † denotes a complex conjugation. This has the corollary that Y_0 is a real number.

Derivatives

Derivatives of discrete quantities are applied differently depending on whether the derivative is in the direction of a periodic co-ordinate. In the angular directions taking a Fourier transform then replaces the derivative with multiplication. For the toroidal direction $\xi(\phi) \sim e^{in\phi}$ and our geometry is symmetric in ϕ meaning that equilibrium quantities have no ϕ-dependence and so $\partial_\phi \to in$. Equilibrium functions may vary poloidally and so each Fourier component is multiplied by the appropriate exponent, for example since $\xi(\vartheta) \sim e^{im\vartheta}$ then:

$$\partial_\vartheta (X\xi) \sim \partial_\vartheta \left(\sum_{k=0}^{N_\vartheta - 1} Y_k e^{ik\vartheta} e^{im\vartheta} \right) = \sum_{k=0}^{N_\vartheta - 1} i(k+m) Y_k e^{ik\vartheta} e^{im\vartheta} \tag{3.59}$$

The equilibrium functions and discretised displacement are not approximated by a Fourier series in the radial direction and so we employ a finite dif-

ference approach to radial derivatives of equilibrium functions. For the discretised displacement the radial derivatives of the basis functions are known exactly and so are used when appropriate. The finite difference method makes a discrete approximation to the derivative function using values of the operand on the grid of the independent variable. Suppose equilibrium function f is defined on the discrete grid $\{s_0, \ldots, s_{n-1}\} \in [s_{min}, s_{max}]$, so $f_i = f(s_i)$. Consider the Taylor series $f_{i+1} = f_i + f_i'(s_{i+1} - s_i) + \frac{f_i''}{2!}(s_{i+1} - s_i)^2 + \ldots$ where we denote $(s_{i+1} - s_i) = \Delta s_i$. Then rearranging gives the desired approximation:

$$f_i' = \frac{f_{i+1} - f_i}{\Delta s_i} + \mathcal{O}(\Delta s_i) \tag{3.60}$$

and the process is easily generalised to higher order derivatives.

In order to decrease the error there are two main strategies. Firstly, we note that the error is a function of Δs_i which therefore should be made a small quantity to decrease the error. Secondly, if $\Delta s_i \ll 1$ then the accuracy of the derivative can be increased by increasing the leading order to which the error depends on Δs_i. To achieve the second of these we can take Taylor series for the dependent function at further grid points, say $f_{i-1} = f_i - f_i' \Delta s_{i-1} + \frac{f_i''}{2!}\Delta s_{i-1}^2 + \ldots$, then solve to eliminate $f_i, f_i'', \ldots$ whilst not eliminating f_i' (or similar for whichever desired order of derivative). The number of grid point values used in the discrete derivative can also be called the *stencil* of the derivative.

The derivative formula (3.60) is called a *forward difference* derivative [48] as it uses only values f_j to calculate f_i' where $j \geq i$. A similar definition is made for *backward difference* derivatives with $j \leq i$. These are usually made at the grid boundaries due to the unavailability of points $s_j > s_{n-1}$ or $s_j < s_0$, but in the grid interior a *central difference* formula is often preferable as it usually offers a reduced error on equally spaced grids. For example, suppose $\Delta s_i = \Delta s_{i-1} = \Delta s$, then:

$$f_i' = \frac{f_{i+1} - f_{i-1}}{2\Delta s} + \mathcal{O}(\Delta s^2) \tag{3.61}$$

Integration

Again there are separate schemes for performing numerical integration depending over which direction it is applied. For the angular directions the orthogonality relation (3.12) applies and so integration is replaced merely with identifying the appropriate Fourier components.

For the radial direction Gaussian quadrature provides a simply implemented, reasonably accurate numerical integration scheme. Gaussian quadrature provides a

method of approximating integrals of the form

$$\int_a^b w(s)f(s)ds \simeq \sum_{i=0}^{N-1} w_i f(s_i) \ , \tag{3.62}$$

where the integrand, $f(s)$, and the *weight function*, $w(s)$, are defined on the (possibly infinite) interval $[a, b]$. The weight function must adhere to certain conditions to be suitable for the Gaussian quadrature process, though we do not list them here as it is sufficient to note that all positive, continuous functions on $[a, b]$ are valid [58].

The *weights* and *abscissas*, w_i and s_i, are found through the following process. First we introduce the space of weighted square integrable functions $L^2[a, b]$ and the inner product:

$$(f, g) = \int_a^b w(s)f(s)g(s)ds \ , \tag{3.63}$$

so $f(s) \in L^2[a, b]$ if (f, f) is well-defined and finite [58]. The first step is then to generate a sequence of functions $p_n \in L^2[a, b]$ such that p_n is a polynomial of order n and $(p_i, p_j) = 0$ for $i \neq j$. The sequence is defined specifically by the recurrence relation:

$$p_0(s) \equiv 1 \quad , \quad \text{“ } p_{-1}(s) \equiv 0 \text{ ”}$$

$$p_{i+1}(s) = (s - \delta_{i+1})p_i(s) - \gamma_{i+1}^2 p_{i-1}(s) \tag{3.64}$$

$$\delta_{i+1} = \frac{(xp_i, p_i)}{(p_i, p_i)} \quad , \quad \gamma_{i+1}^2 = \begin{cases} 1 & i = 0 \\ \frac{(p_i, p_i)}{(p_{i-1}, p_{i-1})} & i \geq 1 \end{cases} \tag{3.65}$$

Finally, for a scheme of order n, our abscissas are the roots of the polynomial $p_n(s)$, $\{s_0, \ldots, s_{n-1}\} \in (a, b)$ and the weights are the solutions to the following linear system:

$$\sum_{i=0}^{n-1} p_k(s_i)w_i = \begin{cases} (p_0, p_0) & k = 0 \\ 0 & k = 1, \ldots, n-1 \end{cases} \tag{3.66}$$

Then the Gaussian quadrature scheme of order n can be expressed through the sum Eq. (3.62). It can further be shown that if $f(s)$ is a polynomial of order $2n - 1$ or less then the quadrature is exact [58].

The Gaussian quadrature implemented as standard in Whales2 is Gauss-Legendre quadrature. This particular variation of Gaussian quadrature uses the weight function $w(s) = 1$ and is expressed on the interval $[a, b] = [-1, 1]$. The advantage of this method is that the abscissas and weights for many values of N have already been calculated in many texts, such as [59], or are easily calculated.

The Legendre polynomials are generated by the recurrence relation described above, abscissas can be solved with a numerical root finder (or analytically as radicals in the case of some low N values) and the weights are given by the formula [59]:

$$w_i = \frac{2}{(1-s_i^2)[P_N'(s_i)]^2} \ . \tag{3.67}$$

So the weights and abscissas can be pre-calculated and held in Whales2, thereby decreasing the computational load and ensuring that the values are calculated to the correct precision beforehand. To apply these values to the integrals required in Whales2 a change of limits is necessary, namely:

$$\int_a^b f(s)ds = \frac{b-a}{2}\int_{-1}^{1} f\left(\frac{b-a}{2}\tilde{s} + \frac{b+a}{2}\right) d\tilde{s} \ . \tag{3.68}$$

If $\tilde{w}_i$ and $\tilde{s}_i$ correspond to the interval $[-1, 1]$ then the corresponding weights and abscissas used to integrate over $[a, b]$ are:

$$s_i = \frac{b-a}{2}\tilde{s}_i + \frac{b+a}{2} \ , \tag{3.69}$$

$$w_i = \frac{b-a}{2}\tilde{w}_i \ . \tag{3.70}$$

This method will integrate polynomials of order up to and including $2N-1$ exactly, though of course this is limited by floating point precision. However, machine precision can nearly be achieved when using the same precision abscissas and weights. In order to determine the required value of N, the integrand in finite elements can be thought of as the product of the two shape functions with the equilibrium function. If the equilibrium is taken from a numerical solver, then the equilibrium functions will be represented by an interpolating polynomial and so it is trivial to calculate the value of N that will give exact integration, since both of the shape functions are also polynomials. In this case, the error is determined by the interpolation rather than the quadrature. In the case of an analytical equilibrium, such as Soloviev, the equilibrium functions will not necessarily be polynomials and so exact integration is not ensured. An upper bound for the error in Gaussian Quadrature can be given as [60]:

$$E_N = (b-a)^{2N+1}\frac{N+1}{N(2N+1)}\frac{N!^4}{(2N)!^3}||f^{(2N)}||_\infty \ . \tag{3.71}$$

This converges to zero quickly with increasing N and so for most situations simply calculating the required n to exactly integrate the product of the two polynomials and setting $N = n+1$ is more than sufficient, with one major exception outlined

below. Choosing a larger N is often wasteful as it significantly increases the computational time required to set up the matrices.

Furthermore, the geometry employed in Whales2 suffers from a geometric singularity at the magnetic axis, $s = 0$, and functions of the type s^{-j} can be encountered in the integrands, where j is positive. These functions are not well approximated by polynomials in the vicinity of the singularity and so the Gaussian-Legendre quadrature becomes inaccurate. This applies to grid cells which are near to but do not include the singularity so we refer to this as an "offstage singularity" [61]. An alternative quadrature is therefore made available in Whales2 based on Gaussian quadrature but with a weight function of the form $w(s) = s^{-2}$. The quadrature becomes:

$$\int_a^b f(s)ds = \int_a^b w(s)(s^2 f(s))ds \simeq \sum_{i=0}^{N-1} w_i(s_i^2 f(s_i)) \tag{3.72}$$

So any functions of the sort $f(s) \sim s^{-j}$ can be integrated accurately as polynomials for $j \leq 2$. The extension of this method for $j > 2$ is simple to implement. The advantage of this method over Gauss-Legendre is that the offstage singularity can be treated up to arbitrary order in s^{-j}. Also, it is a general method that does not require much information about the integrand beforehand, though it will become inaccurate if j in the integrand is higher than the weight function. The drawback of this method is that it will require a larger N to have the same highest order accuracy as Gauss-Legendre. This new method will be able to "perfectly" integrate an integrand $s^2 f(s)$ of polynomial order $2N-1$, implying the function $f(s)$ is of order $2N - 3$. The polynomials for this quadrature can be calculated by hand in terms of a and b but this quickly becomes very tedious and prone to mistakes, so instead the recurrence relation Eq. (3.64) is set up to numerically calculate the polynomial coefficients. Using common floating point datatypes (float, double) quickly leads to unacceptable truncation error and so a high precision datatype is necessary. The abscissas and weights are solved for using standard numerical techniques as there are no general analytic expressions in this case. Since this recurrence must be performed for each $[a, b]$ and requires high precision floating point numbers there is additional computational burden compared to Gauss-Legendre, though it is small compared to the overall runtime of a typical Whales2 run.

An alternative method to handle offstage singularities is given by Carley [61], building on the work of Kolm and Rokhlin [62]. The implementation is similar to that of Gaussian Quadrature, but requires that a system of equations is solved for each interval of integration to reflect the changing position of the singularity relative

to the interval. This method is reported to achieve high precision for sufficiently high order N. However, it loses the attractive fundamental property of Gaussian quadrature that ensures precise integration of polynomials of order $2N-1$ or less [61]. Therefore, this scheme has not been included in this version of Whales2.

3.4 Choice of eigenvalue solver

The finite elements discretisation of the MHD equations implies that the matrices of the generalised eigenvalue problem (3.19) are *banded matrices*, meaning that all non-zero elements of the matrix are present within a constrained number of columns from the central diagonal, where the constraint is less than the matrix size. Whales2 employs finite elements that use the smallest possible stencil, only coupling to their immediate neighbours. This gives a banding size of $3V$ where V is the number of variables at each node. The spectral method of discretisation uses global modes that can all couple, producing a dense block matrix of these banded submatrices (see Eqs. (3.21)-(3.22)). This overall matrix is still sparse and so using sparse eigenvalue solvers to solve Eq. (3.19) can be significantly more efficient than dense solvers when only a few eigenvalues are required. Whales2 uses the SLEPc library [63, 64] of eigensolvers, which includes a range of sparse and dense eigensolvers with options to use external packages.

3.5 Self-Adjointness of Whales2

The linearised ideal-MHD equations can be cast into the form (cf. Eq. 2.16):

$$\mu_0 \frac{\partial^2 \boldsymbol{\xi}}{\partial t^2} = \frac{1}{\rho_0} F(\boldsymbol{\xi}) \ . \tag{3.73}$$

If we introduce the form of the normal modes as per Eq. (3.18) then we retrieve the eigenvalue equation:

$$-\mu_0 \omega^2 \boldsymbol{\xi} = \frac{1}{\rho_0} F(\boldsymbol{\xi}) \ . \tag{3.74}$$

for the linear operator $\rho_0^{-1} F$, which is known to be self-adjoint [65]. This property of self-adjointness informs the *spectral theory* of the linearised Ideal-MHD equations, implying that $\omega^2 \in \mathbb{R}$ [26]. Therefore, linear ideal-MHD supports modes that are oscillatory, so-called stable waves, with $\omega^2 > 0$ so the temporal dependence of the normal modes becomes $e^{\pm i\sqrt{\omega}t}$, and instabilities for $\omega^2 < 0$ which gives $e^{\pm\sqrt{\omega}t}$. We are not aware of any similar proof of self-adjointness for the linearised ideal

Hall-MHD equations, so in this regime there are additional possible modes where $\omega^2 \in \mathbb{C}$ that are not purely real or imaginary. Labelling the frequency $\omega = \omega_R + i\omega_I$ we see that these modes can either be stable, damped modes with $e^{\pm i\omega_R t - \omega_I t}$ or *overstable* modes with $e^{\pm i\omega_R t + \omega_I t}$. The self-adjointness of the linear ideal-MHD operator should be preserved in the numerical scheme used to model the equations, though it is not guaranteed. In particular this means for the setup of Eq. (3.19), $\left(\omega^2 \underline{\underline{\mathcal{I}}} + \omega \underline{\underline{\mathcal{H}}} + \underline{\underline{\mathcal{F}}}\right) \cdot \boldsymbol{\xi}^{NM} = \mathbf{0}$, the inertial and force matrices should be self-adjoint - i.e. each matrix should equal its transpose complex conjugate. For the ideal-MHD system: $\left(\omega^2 \underline{\underline{\mathcal{I}}} + \underline{\underline{\mathcal{F}}}\right) \cdot \boldsymbol{\xi}^{NM} = \mathbf{0}$, self-adjointness of both matrices guarantees that the eigenvalues ω^2 are real numbers [26].

We will demonstrate that the scheme employed by Whales2 leads to self-adjoint inertial and force matrices. The general term of the inertial matrix can be written:

$$\begin{aligned}\mathcal{I}^{kl}_{\tilde{h}\tilde{j}} = &\int_{\boldsymbol{V}} e^{i(l-k)\vartheta} H^h_\perp(s) 2s \frac{\mu_0 \rho_0}{\mathcal{J} g^{\psi\psi}} H^j_\perp(s)\ d\boldsymbol{V} \\ &+ \int_{\boldsymbol{V}} e^{i(l-k)\vartheta} H^h_\wedge(s) 2s \mathcal{J} \mu_0 \rho_0 H^j_\wedge(s)\ d\boldsymbol{V}\ . \end{aligned} \tag{3.75}$$

The complex conjugate transpose of this general term of the inertial matrix is:

$$\begin{aligned}\left(\mathcal{I}^{lk}_{\tilde{j}\tilde{h}}\right)^\dagger = &\int_{\boldsymbol{V}} e^{-i(k-l)\vartheta} H^{j\,\dagger}_\perp(s) 2s \frac{\mu_0 \rho_0^\dagger}{\mathcal{J}^\dagger g^{\psi\psi\dagger}} H^{h\,\dagger}_\perp(s)\ d\boldsymbol{V} \\ &+ \int_{\boldsymbol{V}} e^{-i(k-l)\vartheta} H^{j\,\dagger}_\wedge(s) 2s \mathcal{J}^\dagger \mu_0 \rho_0^\dagger H^{h\,\dagger}_\wedge(s)\ d\boldsymbol{V}\ . \end{aligned} \tag{3.76}$$

The equilibrium quantities and shape functions are strictly real, so this expression becomes:

$$\begin{aligned}\left(\mathcal{I}^{lk}_{\tilde{j}\tilde{h}}\right)^\dagger = &\int_{\boldsymbol{V}} e^{i(l-k)\vartheta} H^j_\perp(s) 2s \frac{\mu_0 \rho_0}{\mathcal{J} g^{\psi\psi}} H^h_\perp(s)\ d\boldsymbol{V} \\ &+ \int_{\boldsymbol{V}} e^{i(l-k)\vartheta} H^j_\wedge(s) 2s \mathcal{J} \mu_0 \rho_0 H^h_\wedge(s)\ d\boldsymbol{V} \\ = &\mathcal{I}^{kl}_{\tilde{h}\tilde{j}}\ , \end{aligned} \tag{3.77}$$

so we see that the inertial matrix is self-adjoint (given that the surface terms vanish). To show that the force matrix is self-adjoint we devise a set of rules for integrand terms that ensure self-adjointness. Suppose we have equilibrium quantity A and integrands of the form:

$$F^{lk}_{\tilde{j}\tilde{h}} = e^{-il\vartheta} H^j_\alpha\, A\, e^{ik\vartheta} H^h_\beta\ , \tag{3.78}$$

and

$$G^{lk}_{\tilde{j}\tilde{h}} = e^{-il\vartheta} H^j_\beta \, A \, e^{ik\vartheta} H^h_\alpha \ . \tag{3.79}$$

These integrands are each other's complex conjugate transpose, i.e. $\left(F^{kl}_{\tilde{h}\tilde{j}}\right)^\dagger = G^{lk}_{\tilde{j}\tilde{h}}$ and vice versa. The integral of the sum of these integrands, say $\mathcal{P}^{lk}_{\tilde{j}\tilde{h}}$, will therefore be self-adjoint:

$$\mathcal{P}^{lk}_{\tilde{j}\tilde{h}} = \int_{\boldsymbol{V}} F^{lk}_{\tilde{j}\tilde{h}} + G^{lk}_{\tilde{j}\tilde{h}} \ d\boldsymbol{V} \ , \tag{3.80}$$

$$\left(\mathcal{P}^{kl}_{\tilde{h}\tilde{j}}\right)^\dagger = \int_{\boldsymbol{V}} \left(F^{kl}_{\tilde{h}\tilde{j}}\right)^\dagger + \left(G^{kl}_{\tilde{h}\tilde{j}}\right)^\dagger \ d\boldsymbol{V} \tag{3.81}$$

$$= \int_{\boldsymbol{V}} G^{lk}_{\tilde{j}\tilde{h}} + F^{lk}_{\tilde{j}\tilde{h}} \ d\boldsymbol{V} \tag{3.82}$$

$$= \mathcal{P}^{lk}_{\tilde{j}\tilde{h}} \ . \tag{3.83}$$

So terms of the force matrix integrand that obey this relationship will only contribute self-adjoint terms to the matrix. Note that if $\alpha = \beta$ then this term in an integrand is its own complex conjugate transpose - this is the case for the integrands of inertial matrix (3.37)-(3.38). This is also true for the force matrix integrand (3.48). For the purposes of establishing self-adjointness we view the radial derivatives of the shape functions as though they are shape functions for an independent variable, i.e. $\alpha, \beta \in \{\perp, \perp', \wedge, \wedge'\}$. Therefore, we see that the second terms in each of the integrands (3.49) and (3.50) obey the same relationship as Eqs. (3.78)-(3.79) and so will contribute self-adjoint terms to the force matrix. By establishing a full set of such relationships that cover each type of function encountered in the force matrix integrands we show that the force matrix is self-adjoint.

In the case that the integrand contains a derivative in the poloidal direction we have to take into account that the equilibrium functions can also have a poloidal dependence. The equilibrium functions are real-valued and analytical across the plasma domain, so we write a generic equilibrium quantity as:

$$E(\vartheta) = \sum_{m=-\infty}^{\infty} E^{(m)} e^{im\vartheta} \ , \tag{3.84}$$

with $E^{(m)} = \left(E^{(-m)}\right)^\dagger$. Suppose we have the integrands:

$$F^{lk}_{\tilde{j}\tilde{h}} = e^{-il\vartheta} H^j_\alpha \, A \partial_\vartheta \left(B \, e^{ik\vartheta} H^h_\beta\right) \ , \tag{3.85}$$

and

$$G^{lk}_{\tilde{j}\tilde{h}} = -e^{-il\vartheta} H^j_\beta \, B \partial_\vartheta \left(A \, e^{ik\vartheta} H^h_\alpha \right) \ . \tag{3.86}$$

We will show that $F^{lk}_{\tilde{j}\tilde{h}} = \left(G^{kl}_{\tilde{h}\tilde{j}} \right)^\dagger$. The equilibrium functions A and B are expanded as (3.84) and we choose a, b such that $a + b + k - l = 0$ as only these terms will contribute to the matrix. We write, without loss of generality:

$$\begin{aligned} F^{lk}_{\tilde{j}\tilde{h}} &= e^{-il\vartheta} H^j_\alpha \, A^{(a)} e^{ia\vartheta} \partial_\vartheta \left(B^{(b)} e^{ib\vartheta} \, e^{ik\vartheta} H^h_\beta \right) \\ &= i(b+k) e^{i(a+b+k-l)\vartheta} H^j_\alpha \, A^{(a)} \, B^{(b)} \, H^h_\beta \ . \end{aligned} \tag{3.87}$$

We only need to show that $G^{kl}_{\tilde{h}\tilde{j}}$ contains a term that is the complex conjugate of (3.87). We choose the $-a$ and $-b$ terms of the expansions of A and B respectively:

$$\begin{aligned} G^{kl}_{\tilde{h}\tilde{j}} &= -e^{-ik\vartheta} H^h_\beta \, B^{(-b)} e^{-ib\vartheta} \partial_\vartheta \left(A^{(-a)} e^{-ia\vartheta} \, e^{il\vartheta} H^j_\alpha \right) \\ &= -i(l-a) e^{-i(a+b+k-l)} H^h_\beta \, B^{(-b)} \, A^{(-a)} \, H^j_\alpha \\ &= -i(b+k) e^{-i(a+b+k-l)} H^j_\alpha \, A^{(-a)} \, B^{(-b)} \, H^h_\beta \ , \end{aligned} \tag{3.88}$$

where we have used that $a + b + k - l = 0$. Now using that $\left(A^{(-a)} \right)^\dagger = A^{(a)}$ then it is clear that $F^{lk}_{\tilde{j}\tilde{h}} = \left(G^{kl}_{\tilde{h}\tilde{j}} \right)^\dagger$ so the sum of Eqs. (3.85) and (3.86) gives self-adjoint terms.

Omitting further tedious derivation we present a list of integrand pairs that, when taken together, give self-adjoint terms to the matrix. We employ the condensed notation $H_{\alpha/\beta} = e^{\pm il\vartheta} H^j_{\alpha/\beta}$ for all l/k and j/h. The list starts with the two relations just derived:

$$H_\alpha \, A \, H_\beta \leftrightarrow H_\beta \, A \, H_\alpha \ , \tag{3.89}$$

$$H_\alpha \, A \, \partial_\vartheta \left(B \, H_\beta \right) \leftrightarrow -H_\beta \, B \, \partial_\vartheta \left(A \, H_\alpha \right) \ , \tag{3.90}$$

$$H_\alpha \, A \, \partial_\vartheta \left(B \, \partial_\vartheta \left(C \, H_\beta \right) \right) \leftrightarrow H_\beta \, C \, \partial_\vartheta \left(B \, \partial_\vartheta \left(A \, H_\alpha \right) \right) \ , \tag{3.91}$$

$$H_\alpha \, A \, \partial_\phi H_\beta \leftrightarrow -H_\beta \, A \, \partial_\phi H_\alpha \ , \tag{3.92}$$

$$H_\alpha \, A \, \partial^2_\phi H_\beta \leftrightarrow H_\beta \, A \, \partial^2_\phi H_\alpha \ . \tag{3.93}$$

We expand out the wedge and parallel directional derivatives:

$$\nabla_B = (\mathbf{B}_0 \cdot \boldsymbol{\nabla}) = \frac{1}{\mathcal{J}} \partial_\vartheta + f(\psi) g^{\phi\phi} \partial_\phi \ , \tag{3.94}$$

$$\nabla_T = (\mathbf{T} \cdot \boldsymbol{\nabla}) = g^{\phi\phi} \partial_\phi - \frac{f(\psi)}{\mathcal{J} g^{\psi\psi}} \partial_\vartheta \ , \tag{3.95}$$

and use Eqs. (3.89)-(3.93) to derive the following:

$$H_\alpha\, A\, \mathcal{J} \nabla_B\, (B\, H_\beta) \leftrightarrow -H_\beta\, B\, \mathcal{J} \nabla_B\, (A\, H_\alpha) \tag{3.96}$$

$$H_\alpha\, A\, \mathcal{J} \nabla_B\, (B\, \nabla_B\, (C\, H_\beta)) \leftrightarrow H_\beta\, C\, \mathcal{J} \nabla_B\, (B\, \nabla_B\, (A\, H_\alpha)) \tag{3.97}$$

$$H_\alpha\, A\, \mathcal{J} g^{\psi\psi} \nabla_T\, (B\, H_\beta) \leftrightarrow -H_\beta\, B\, \mathcal{J} g^{\psi\psi} \nabla_T\, (A\, H_\alpha) \tag{3.98}$$

$$H_\alpha\, A\, \mathcal{J} g^{\psi\psi} \nabla_T\, (B\, \nabla_T\, (C\, H_\beta)) \leftrightarrow H_\beta\, C\, \mathcal{J} g^{\psi\psi} \nabla_T\, (B\, \nabla_T\, (A\, H_\alpha)) \tag{3.99}$$

$$H_\alpha\, A\, \partial_\vartheta \left(B\, \mathcal{J} g^{\psi\psi} \nabla_T\, (C\, H_\beta) \right) \leftrightarrow H_\beta\, C\, \mathcal{J} g^{\psi\psi} \nabla_T\, (B\, \partial_\vartheta\, (A\, H_\alpha)) \tag{3.100}$$

All terms in the force matrix integrands (3.48)-(3.56) have a self-adjoint pair as per the rules derived above, therefore we conclude that both the force and inertial matrices in Whales2 are self-adjoint. The self-adjoint nature of the ideal-MHD equations is therefore preserved in Whales2.

3.6 Convergence testing

To determine the effectiveness of the implementation of finite elements scheme, we measure the error in the eigenfrequency output from Whales2 as a function of the number of grid points, N. The expected relation between these variables is a power law in the form:

$$\lambda_N = \lambda + E_0 \cdot N^{-t} \tag{3.101}$$

where λ is the true eigenfrequency, λ_N is the approximate eigenfrequency, E_0 is a constant, and t is a positive constant. In the case of a single variable PDE then first order accuracy in the eigenfunction is predicted when using constant basis functions [66]. This leads to second order accuracy of the eigenfrequency, i.e. $t = 2$, as the frequency is an integral quantity of the equation. Increasing the order of the basis polynomial gives an increase of two orders in the accuracy of the eigenvalue, so that a linear basis gives fourth-order accuracy in the eigenfrequency etc [67]. Fig. 3.3 shows the error convergence for Whales2 in the case of a CAE in a homogeneous cylinder, for which the frequency is analytically known. Fig. 3.3 plots the error $|\lambda - \lambda_N|$ against N in a log-log scale, so that power law relations will be seen as straight lines with gradient $-t$. We expect that the mixed basis elements are limited in accuracy by the lower order basis, so that a linear-constant basis, for example, will predict a second-order convergence in the eigenfrequency. In fact, Fig. 3.3 shows that the linear-constant choice of basis in Whales2 leads to a power law with $2 \leq t \leq 3$. The quadratic-linear and cubic-quadratic bases conform to the expectation well, clearly showing power law relations of $t = 4$ and $t = 6$ respectively.

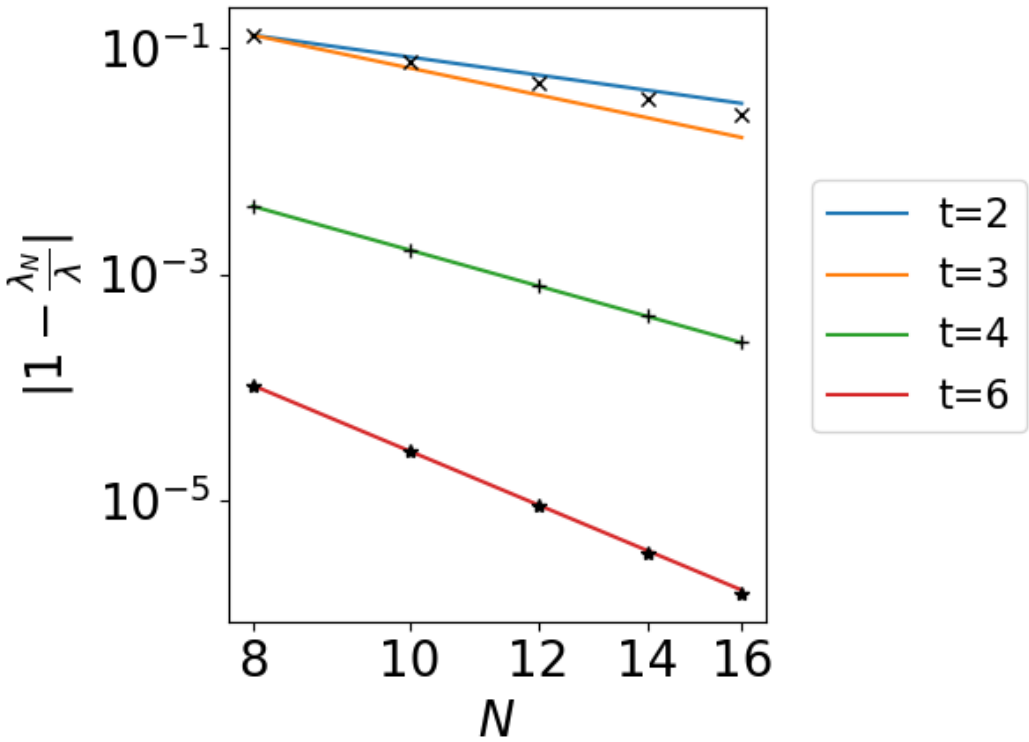

Figure 3.3: The output from Whales2 for each basis function is represented as follows: linear-constant ($\times$, top), quadratic-linear ($+$, middle) and cubic-quadratic ($*$, bottom). Example power law relations, in solid colours, are of the form Eq. (3.101) where E_0 is calculated to match the $N = 8$ point of the Whales2 output.

3.7 MHD linear stability codes

This thesis presents a linear stability code, Whales2, that calculates the spectrum of CAEs in a given tokamak geometry using the ideal Hall-MHD wave equation. There are several linear stability codes currently available to solve for MHD eigenmodes such as MARS [68, 69], CASTOR [70–72], NOVA [39, 73], CAE3B [3, 74] and WHALES [3, 29]. MARS and CASTOR solve the resistive-MHD equations for the spectrum of eigenmodes using finite elements and spectral methods. NOVA solves the ideal-MHD equations using finite elements and spectral methods. These codes do not include the Hall term and so are restricted to the frequency regime such that $\omega \ll \omega_{ci}$.

CAE3B and WHALES are both based around the methodology set out by Smith and Verwichte [3], though neither code is named at that point. Each solves the linearised ideal Hall-MHD equations. CAE3B follows the methodology of [3] directly,

solving for the three components of the perturbed magnetic field $b_\perp$, $b_\wedge$ and $b_\parallel$ using a finite difference scheme in the radial and poloidal directions. A single Fourier mode is assumed in the toroidal direction, though CAE3B is extended to include the effects of toroidal equilibrium plasma flow. WHALES employs finite elements in the radial direction, a Fourier series poloidally and single Fourier harmonic toroidally to solve for the two components of the modified displacement $\eta_\perp$ and $\eta_\wedge$. WHALES and CAE3B both assume a negligible plasma-β to eliminate the slow-magnetoacoustic modes and neglect the shear terms, $k_\parallel^2$, to suppress the shear Alfvén eigenmodes.

Whales2 is built on the same principles as CAE3B and WHALES, so shares many traits with these linear stability codes. However, meaningful differences exist and so a comparison can be made. Though ostensibly CAE3B, WHALES and Whales2 solve the same equations of linearised ideal Hall-MHD, they are solved in different representations for different variables. CAE3B uses a dielectric tensor description of the linearised Hall-MHD, solving for the eigenfrequency iteratively with the Hall term correction updated with each iteration. In WHALES the user can choose to switch the Hall term off, like in Whales2. However, the underlying ideal-MHD equations in WHALES do not have the self-adjointness property that is preserved in Whales2. The lack of self-adjointness makes it difficult for the user to distinguish non-ideal effects occurring due to the lack of self-adjointness and those arising from the inclusion of the Hall term. Whales2 also allows the user choice in the finite elements scheme employed and the eigenvalue solver. Judicious application of both can be used to optimise the performance of Whales2. A comparison of results between the three codes CAE3B, WHALES and Whales2 would be useful to determine the relative advantages of each implementation of [3] and is recommended for further work to build on the results in this thesis.

Chapter 4

CAEs in cylindrical Hall-MHD

Whales2 is used to explore particular eigenmode structures and the spectrum of eigenfrequencies for CAEs. We demonstrate the code's ability to reproduce CAE modes by applying it to a cylindrical geometry, the simplest geometry implemented in Whales2. We use the (r, θ, z) coordinate system to describe the cylinder. Due to the θ and z symmetries the equilibrium only depends on the radial coordinate. Only cylinders with a circular cross-section have currently been implemented in Whales2. The ideal-MHD equilibrium in a cylinder follows a simple force balance equation that can be written in terms of the magnetic field and plasma pressure. We achieve this by rearranging the Lorentz force equation (1.75), the Solenoidal condition (1.67), and Ampère's law (1.66) into the following equation [26]:

$$\frac{\mathrm{d}}{\mathrm{d}r}\left[\mu_0 p(r) + \frac{B_0^2}{2}\right] = -\frac{B_{0\theta}^2}{r} \ . \tag{4.1}$$

We focus on results for CAEs solved with the inclusion of Hall terms in the linearised MHD equations. As noted in Section 3.5, in this case the CAE frequencies can be complex numbers. However, for all of the results in this section we have found that the imaginary component of the frequency is negligible to the point where it is indistinguishable from computational error. Therefore, we treat the computed frequencies as though they are purely real numbers.

4.1 Homogeneous θ-pinch

The homogeneous θ-pinch is described by an equilibrium with uniform magnetic field, pressure and density profiles - this clearly satisfies the force balance Eq. (4.1). We choose the pressure function to be zero. The magnetic field is in the $\hat{z}$-direction,

$\mathbf{B}_0 = B_0\hat{z}$, which means that there is no poloidal magnetic flux. Therefore, for this equilibrium we choose to use the toroidal magnetic flux function in place of the poloidal flux function. The toroidal flux function is:

$$\psi_T = \frac{B_0}{2} r^2 \ . \tag{4.2}$$

We note that the relation of this toroidal flux function to the toroidal magnetic flux, Φ_T, is: $\psi_T = \Phi_T/2\pi$. The coordinate vectors (2.17) for the homogeneous θ-pinch become:

$$\boldsymbol{\nabla}\psi = B_0 r\hat{r} \ , \ \mathbf{T} = \frac{1}{r}\hat{\theta} \ , \ \mathbf{B}_0 = B_0\hat{z} \ , \tag{4.3}$$

and the displacement components:

$$\tilde{\xi}_\perp = r\xi_r \ , \ \tilde{\xi}_\wedge = \xi_\theta \ . \tag{4.4}$$

The following quantities are simply expressed:

$$S = 0 \ , \ \kappa = 0 \ , \ \mathbf{J}_0 = \mathbf{0} \ , \ V_A^2 = \frac{B_0^2}{\mu_0\rho_0} \ , \tag{4.5}$$

where the Alfvén velocity is constant. We define the Alfvén frequency:

$$\omega_A^2 = V_A^2 k^2 \ . \tag{4.6}$$

The variables for this configuration can be summarised:

$$B_0 \ , \ a \ , \ \rho_0 \ , \ s \ , \ m \ , \ k \ , \tag{4.7}$$

where here, and throughout the rest of this chapter unless stated otherwise, s is the radial wavenumber. We use the 'quantum number' style notation (s, m, k) to label discrete eigenmodes within a given equilibrium. The quantum numbers m and k are well-defined in the cylindrical geometry as each refers to a single Fourier harmonic in the azimuthal (poloidal) and longitudinal (toroidal) directions respectively. However, s depends on the radial boundary conditions which depend on m and are not consistent across the various perturbed quantities that we are interested in, i.e. $\tilde{\xi}_\perp$, $\tilde{\xi}_\wedge$ and $b_\parallel$. Therefore, we use the convention that the fundamental harmonic, i.e. the CAE that exists with the fewest number of nodes/anti-nodes, is labelled $s = 1$ and subsequent CAEs in the sense of increasing number of nodes/anti-nodes are labelled consecutively with integer values of s.

Ideal-MHD

When the Hall term is set to zero in Eq. (3.19) the eigenvalue problem is reduced to:

$$\left(\omega^2 \underline{\underline{\mathcal{I}}} + \underline{\underline{\mathcal{F}}}\right) \cdot \boldsymbol{\xi}^{NM} = 0 \ . \tag{4.8}$$

In the ideal-MHD case Whales2 solves for the eigenvalue ω^2. Therefore there are actually two degenerate solutions for each eigenmode, $\pm\omega$. For the ideal-MHD solutions we will usually refer to ω^2 rather than ω.

The ideal-MHD equations for the zero-pressure homogeneous θ-pinch with the boundary conditions Eq. (2.126)-(2.127) can be expressed through the total pressure, p_T, as:

$$\frac{\partial^2 p_T}{\partial r^2} + \frac{1}{r}\frac{\partial p_T}{\partial r} - \left(\chi^2 + \frac{m^2}{r^2}\right) = 0 \ , \tag{4.9}$$

$$\rho_0(\omega^2 - \omega_A^2)\xi_r = \frac{\partial p_T}{\partial r} \ , \tag{4.10}$$

$$\rho_0(\omega^2 - \omega_A^2)\xi_\theta = \frac{im}{r} p_T \ , \tag{4.11}$$

where χ is given by:

$$\chi^2 = -\frac{\omega^2 - \omega_A^2}{V_A^2} \ . \tag{4.12}$$

These are solved to give the displacement components for the CAEs as:

$$\xi_r = \frac{|\chi|}{\rho_0(\omega^2 - \omega_A^2)} J_m'(|\chi| r) \ , \tag{4.13}$$

$$\xi_\theta = \frac{im}{r}\frac{1}{\rho_0(\omega^2 - \omega_A^2)} J_m(|\chi| r) \ , \tag{4.14}$$

where J_m is a Bessel function of the first kind, of order m. The boundary conditions imply that for this set of solutions: $\chi^2 < 0$, i.e. the CAEs are of higher frequency than the Alfvén frequency, as we expect, and that $|\chi| a = j'_{ms}$ where j'_{ms} is the sth zero of J'_m. There is another set of solutions pertaining to the shear Alfvén modes, an infinitely degenerate set of solutions at the frequency $\omega^2 = \omega_A^2$. Eqs. (4.9)-(4.14) are unchanged under the substitution $k \to -k$, and this is also clearly true of the shear Alfvén modes. We say that in a homogeneous cylinder the linearised ideal-MHD equations are symmetric in k. For $m \to -m$ the sign of ξ_θ changes relative to ξ_r but the frequency ω^2 is unaffected. Fig. 4.1 shows that the output eigenfunctions from Whales2 well match the expressions (4.13)-(4.14) for various values of (s, m, k). The boundary conditions (2.126)-(2.127) are clearly adhered to for both $\tilde{\xi}_\perp$ and $\tilde{\xi}_\wedge$.

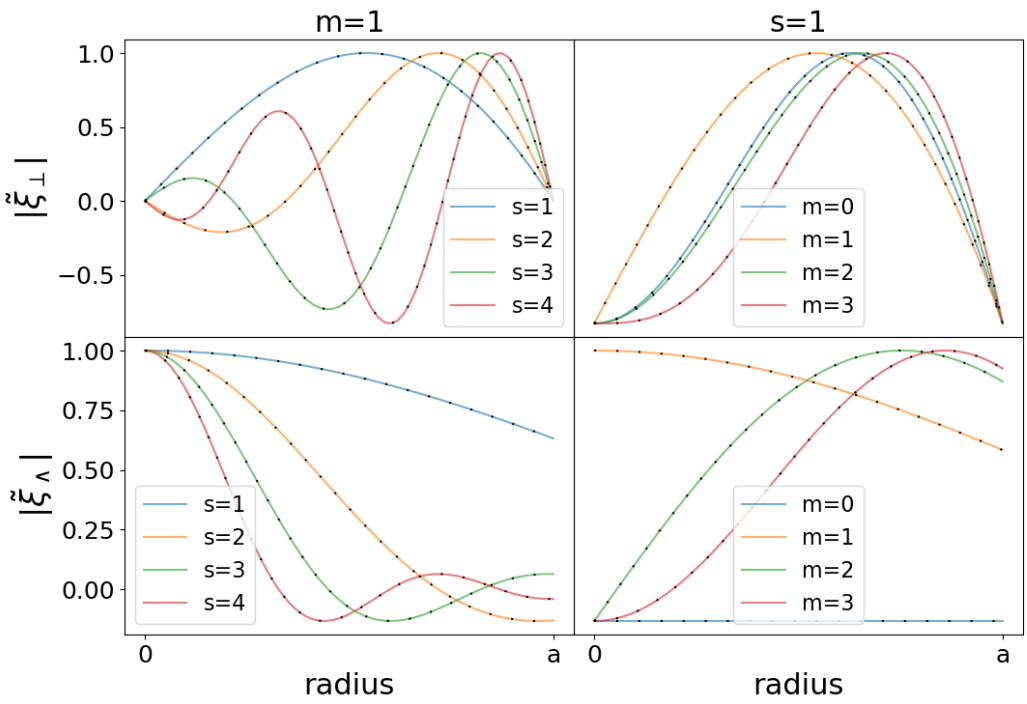

Figure 4.1: The solid coloured lines show the eigenfunctions output from Whales2, whilst the black dotted lines show the values known analytically from Eqs. (4.13) - (4.14). We have normalised both displacement components independently. The chosen equilibrium values are $B_0 = 1$ T, $a = 1$ m, $\rho_0 = 1$ kgm^{-3}, $k = 1$.

In order to study the dispersion relation of the CAE spectrum we rearrange Eq. (4.12) to give in terms of ω:

$$\omega^2 = (k^2 - \chi^2)V_A^2 = k_e^2 V_A^2 \ , \tag{4.15}$$

with $k_e = \sqrt{k^2 + j_{ms}'^2/a^2}$, the effective wavenumber for the dispersion relation. This dispersion relation for the CAE modes is clearly Sturmian - increasing wavenumber implies higher frequency - and this can be seen in Fig. 4.2. Fig. 4.2 shows a hierarchy in the quantum numbers s, m, k as to how the frequency increases with an increase in the respective wavenumber. Analogously with the dispersion relation for CAEs in a homogeneous magnetic slab Eq. (1.157), which in the absence of plasma pressure reduces to: $\omega^2 = V_A^2(k_x^2 + k_y^2 + k_z^2)$, an approximate heuristic dispersion relation for a homogeneous cylinder is [43, 75]:

$$\omega^2 \simeq V_A^2 \left(\frac{s^2}{L_r^2} + \frac{m^2}{a^2} + k^2 \right) \ , \tag{4.16}$$

where L_r is a length scale that is related to the radial width of the eigenmode. Note that the relation (4.16) is a hyperbolic function in each of the three mode numbers (s, m, k) when the other two are held constant.

Since $L_r < a$ it follows that the difference in frequency is largest for a change in the wavenumber s, i.e. $\Delta\omega_{s\to s\pm1} > \Delta\omega_{m\to m\pm1} = \Delta\omega_{k\to k\pm1}$. In Fig. 4.2 we observe $\Delta\omega_{s\to s\pm1} > \Delta\omega_{m\to m\pm1} > \Delta\omega_{k\to k\pm1}$ instead - this is more like what we would expect in a tokamak where $k \to n/R_0$ and $R_0 > a$ so $\Delta\omega_{m\to m\pm1} > \Delta\omega_{n\to n\pm1}$. The dashed lines in Fig. 4.2 show the predicted values from Eq. (4.16), where L_r has been calculated so that the predicted frequency matches the known frequency at the fundamental mode $(s, m, k) = (1, 1, 1)$. It is clear that Eq. (4.16) should only be used to predict frequencies for the lowest values of s and m.

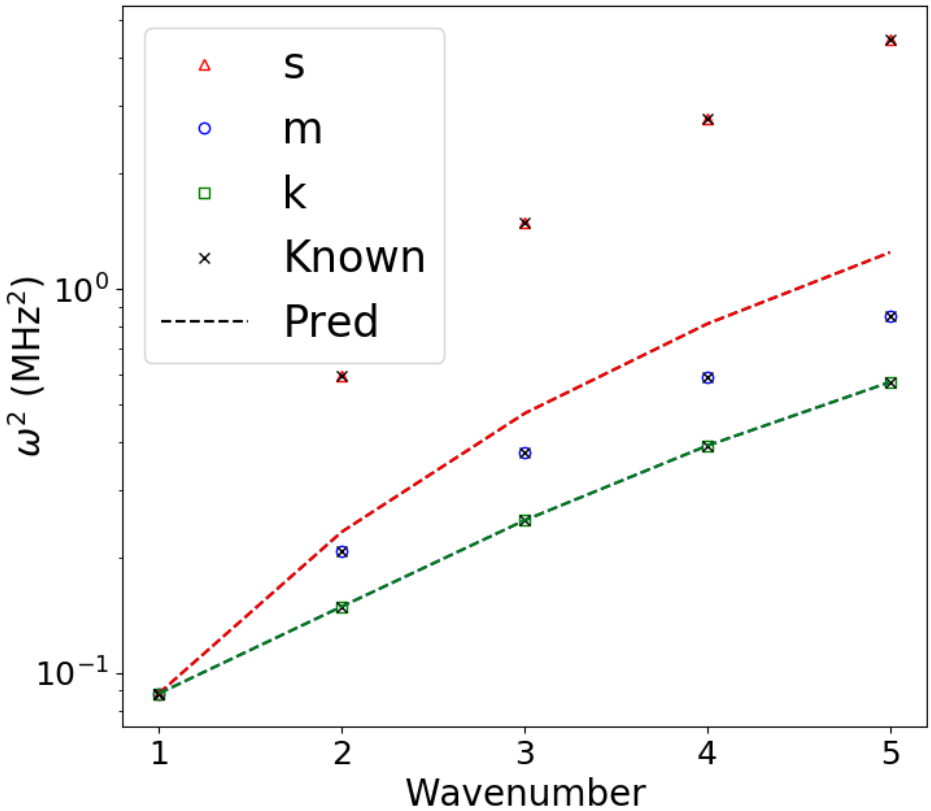

Figure 4.2: CAE dispersion relations are shown for a homogeneous θ-pinch when varying the individual "quantum numbers" s, m, and k. The crosses show the analytically known eigenfrequencies calculated from Eq. (4.15) and the dashed lines show the predicted frequencies from Eq. (4.16). Note that the dashed line for m (blue) and k (green) are coincident. The output from Whales2 was produced using $N_\psi = 64$, $N_\theta = 256$, $\rho_0 = 10^{-6}$ kgm^{-3}, $a = 1$ m, $B_0 = 1$ T.

Hall-MHD

The addition of the Hall term lifts the $\pm\omega$ degeneracy present in ideal-MHD. In this case Whales2 solves for ω as the eigenvalue. The spectrum of CAE modes for the Hall-MHD equations in a homogeneous θ-pinch has an analytical solution given by:

$$\xi_r \sim A|\chi|J'_m(|\chi|r) + h\omega_A^2 \frac{m}{r} J_m(|\chi|r) \ , \tag{4.17}$$

$$\xi_\theta \sim h\omega_A^2|\chi|J'_m(|\chi|r) + A\frac{m}{r} J_m(|\chi|r) \ , \tag{4.18}$$

with:

$$A = \omega^2 - \omega_A^2 \ , \tag{4.19}$$

$$h = \frac{\omega}{\omega_{ci}} \ , \tag{4.20}$$

$$\chi^2 = -\frac{A^2 - h^2\omega_A^4}{V_A^2(A + h^2\omega_A^2)} = -\frac{(\omega^2 - \omega_A^2)}{V_A^2}\left(\frac{1 - h^2\frac{\omega_A^4}{(\omega^2-\omega_A^2)^2}}{1 + h^2\frac{\omega_A^2}{(\omega^2-\omega_A^2)}}\right) \ . \tag{4.21}$$

We do not explicitly include the amplitude for Eqs. (4.17)-(4.18) as Whales2 is a linear code and so the amplitude of each mode is arbitrary (though the relative amplitudes of the displacement components $\tilde{\xi}_\perp$ and $\tilde{\xi}_\wedge$ are preserved). Note that in the limit $h \to 0$ expressions (4.17), (4.18) and (4.21) reduce to the equivalent ideal-MHD expressions.

The CAE dispersion relation from solving Hall-MHD equations in this geometry is:

$$\mathcal{D}(\omega) = A|\chi|J'_m(|\chi|a) + h\omega_A^2 \frac{m}{a} J_m(|\chi|a) = 0 \ . \tag{4.22}$$

Since χ is a function of ω, dispersion relation (4.22) is transcendental and an exact solution cannot be found analytically. We can still determine an approximate analytical solution. Both the components (4.17)-(4.18) and the dispersion relation (4.22) are even functions in the wavenumber k, as in the ideal-MHD case, but are no longer even in ω or m. However, m and ω appear as a product and so there is a symmetry upon the substitution $(\omega, m) \to (-\omega, -m)$. Therefore, we choose to solve for $\pm\omega$ with $m \geq 0$ (and $k \geq 0$) without loss of generality.

In order to obtain a mathematically tractable form of the dispersion relation (4.22), we assume that the contribution from the Hall term is small. For the case $m \neq 0$ we assume $h \ll 1$, and linearise the dispersion relation about the ideal-MHD dispersion relation. We denote the ideal-MHD solution quantities with a subscript 0, e.g. ω_0. The quantity χ only contains factors of h^2 and so $\chi \to \chi_0$. The dispersion

relation can be written:

$$\mathcal{D}(\omega) \simeq \mathcal{D}_0(\omega) + \mathcal{D}_1(\omega) \ , \tag{4.23}$$

$$\mathcal{D}_0(\omega) = A|\chi_0|J'_m(|\chi_0|a) \ , \tag{4.24}$$

$$\mathcal{D}_1(\omega) = h\omega_A^2 \frac{m}{a} J_m(|\chi_0|a) \ . \tag{4.25}$$

We write $\omega = \omega_0 + \delta\omega$ with $\delta\omega \sim \mathcal{O}(h)$ as the Hall correction. The linearised dispersion relation has the form:

$$\mathcal{D}(\omega) \simeq \mathcal{D}_0(\omega_0 + \delta\omega) + \mathcal{D}_1(\omega_0) \ . \tag{4.26}$$

We take a Taylor expansion: $\mathcal{D}_0(\omega_0 + \delta\omega) = \mathcal{D}_0(\omega_0) + \mathcal{D}'_0(\omega_0)\delta\omega + \mathcal{O}(h^2)$. We note that $\mathcal{D}_0(\omega_0) = 0$. We neglect the higher order terms, $\mathcal{O}(h^2)$, giving the linearised dispersion relation:

$$\mathcal{D}'_0(\omega_0)\delta\omega + \mathcal{D}_1(\omega_0) = 0 \ , \tag{4.27}$$

so rearranging for the Hall frequency correction:

$$\delta\omega = -\frac{\mathcal{D}_1(\omega_0)}{\mathcal{D}'_0(\omega_0)} \ , \tag{4.28}$$

The denominator can be simplified as follows:

$$\begin{aligned} \mathcal{D}'_0(\omega_0) &= A'_0|\chi_0|J'_m(|\chi_0|a) + A_0|\chi_0|'J'_m(|\chi_0|a) + A_0|\chi_0||\chi_0|'aJ''_m(|\chi_0|a) \\ &= A_0|\chi_0||\chi_0|'aJ''_m(|\chi_0|a) \ , \end{aligned} \tag{4.29}$$

since $J'_m(|\chi_0(\omega_0)|a) = 0$. Now we note that $A_0/V_A^2 = j'^2_{ms}/a^2$ and use this to obtain the expression:

$$\delta\omega = -\frac{m}{\omega_{ci}} \frac{\omega_A^2}{j'^2_{ml}} \frac{J_m(|\chi_0(\omega_0)|a)}{J''_m(|\chi_0(\omega_0)|a)} \tag{4.30}$$

We further simplify this using the following relations for Bessel functions [59]:

$$\frac{2m}{x} J_m(x) = J_{m-1}(x) + J_{m+1}(x) \ , \tag{4.31}$$

$$2J'_m(x) = J_{m-1}(x) - J_{m+1}(x) \ , \tag{4.32}$$

which can be manipulated to show:

$$J''_m(x) = \left\{ \left(\frac{m}{x}\right)^2 - 1 \right\} J_m(x) - \frac{1}{x} J'_m(x) \ . \tag{4.33}$$

Therefore the ratio of Bessel functions in Eq. (4.30) becomes:

$$\frac{J_m(|\chi_0(\omega_0)|a)}{J''_m(|\chi_0(\omega_0)|a)} = \frac{J_m(j'_{ms})}{J''_m(j'_{ms})} = \frac{j'^2_{ms}}{m^2 - j'^2_{ms}} \ , \tag{4.34}$$

and the final expression is:

$$\delta\omega = \frac{\omega_A^2}{\omega_{ci}} \frac{m}{j'^2_{ms} - m^2} \qquad m \neq 0 \ . \tag{4.35}$$

For the case $m = 0$, the first-order Hall frequency correction is zero. We need to expand the dispersion relation (4.22) further to include second-order terms.

$$\mathcal{D}(\omega) = A|\chi|J'_m(|\chi|a) = 0 \ \Rightarrow |\chi|a = j'_{0s} \ . \tag{4.36}$$

We write $\omega = \omega_0 + \delta\omega$ with $\delta\omega \sim \mathcal{O}(h^2)$ and apply a binomial expansion to $|\chi|$ to obtain:

$$|\chi| = \left(\frac{A^2 - h^2\omega_A^4}{V_A^2(A + h^2\omega_A^2)}\right)^{\frac{1}{2}} = \left(\frac{A^2 - h^2\omega_A^4}{V_A^2}\right)^{\frac{1}{2}} \left(\frac{1}{A_0} - \frac{2\omega_0\delta\omega + h^2\omega_A^2}{A_0} + \dots\right)^{\frac{1}{2}} \ , \tag{4.37}$$

with $A_0 = \omega_0^2 - \omega_A^2$. Now we multiply out and neglect terms of order $\mathcal{O}(h^4)$ in Eq. (4.37):

$$|\chi|(\omega_0 + \delta\omega) \simeq \frac{A_0^{\frac{1}{2}}}{V_A} \left\{1 - \frac{2A_0\omega_0\delta\omega - h^2\omega_0^2\omega_A^2}{A_0^2}\right\}^{\frac{1}{2}} \ . \tag{4.38}$$

Now we use that $|\chi_0|(\omega_0) = j'_{ms}/a$ and Eq. (4.36) to determine the expression for $\delta\omega$:

$$\delta\omega = \frac{h^2\omega_0\omega_A^2}{2A_0} = \frac{1}{2\omega_{ci}^2} \frac{(j'^2_{0s} + k^2a^2)^{\frac{3}{2}}k^2}{j'^2_{0s}a} \qquad m = 0 \ . \tag{4.39}$$

There are some interesting differences between the expressions (4.35) and (4.39) for $\delta\omega$. We label the expression in Eq. (4.35) as $\delta\omega^{(m)}$ and Eq. (4.39) as $\delta\omega^{(0)}$. $\delta\omega^{(0)}$ is an odd function in ω_0 which means that $\omega = \omega_0 + \mathrm{sgn}(\omega_0)\delta\omega(|\omega_0|)$. The positive and negative frequency solutions have the same magnitude. Alternatively, $\delta\omega^{(m)}$ is even in ω_0 and $\omega = \omega_0 + \delta\omega(|\omega_0|)$. This means that there is a difference of magnitude $2|\delta\omega|$ between the positive and negative frequency solutions. We observe that $j'^2_{ms} > m^2$, at least for moderate values of m. If we label the positive and negative frequency solutions as $\omega^+\backslash\omega^-$ respectively then $|\omega^+| > |\omega_0| > |\omega^-|$ for $m > 0$, with the inequalities reversed for $m < 0$.

It is useful to normalise Eqs. (4.35) and (4.39) by ω_0 to get a measure of the

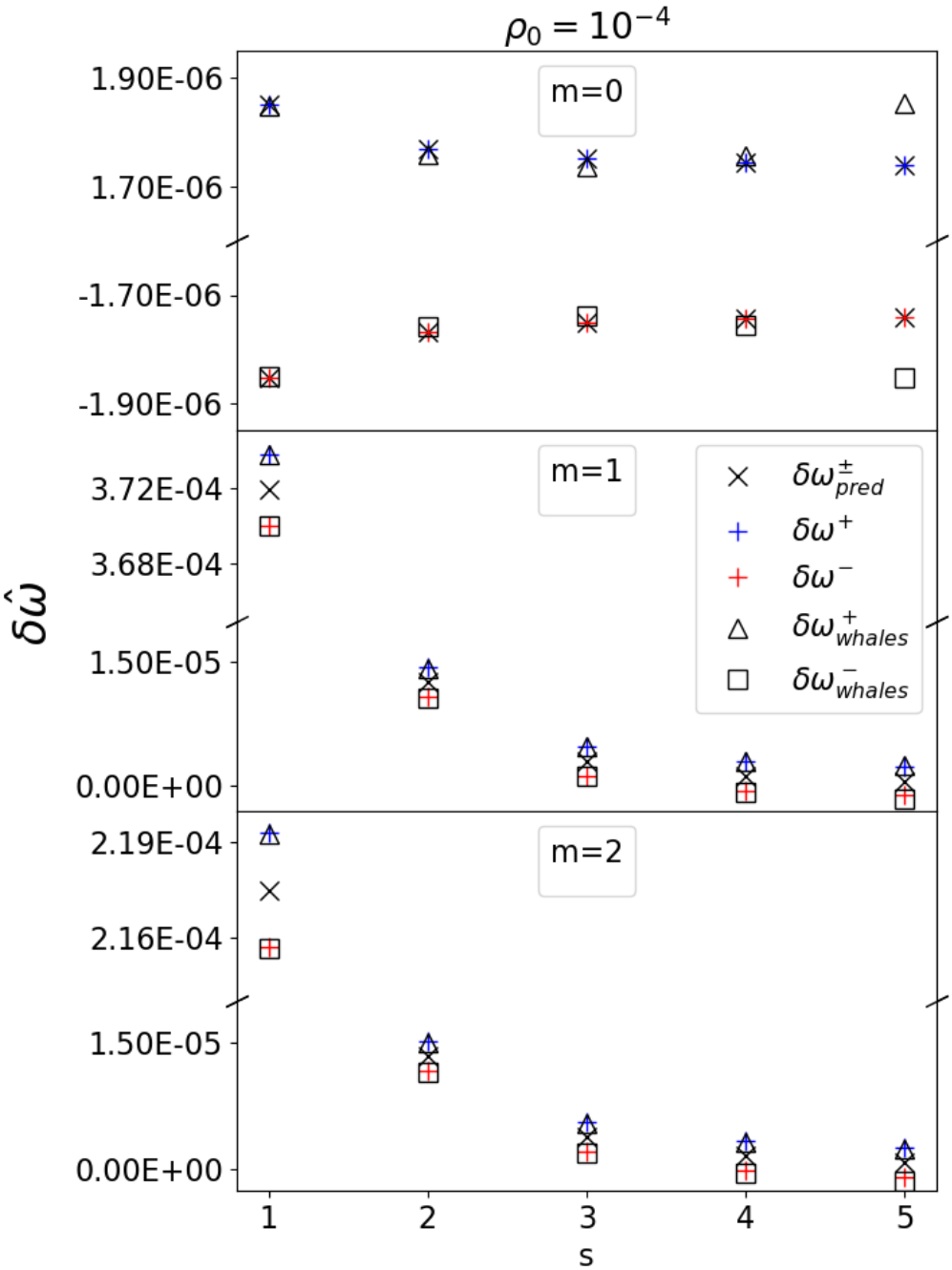

Figure 4.3: CAE dispersion relations against increasing values of the radial mode number, s, are shown for $m = 0, 1, 2$. The output from Whales2 was generated with parameters $B_0 = 1$ T, $a = 1$ m, $\rho_0 = 10^{-4}$ kgm^{-3}, $k = 1$, using hybrid quadratic elements for the perpendicular component and regular linear elements for the wedge component. The grid sizes used are $N_\psi = 128$ and $N_\vartheta = 256$.

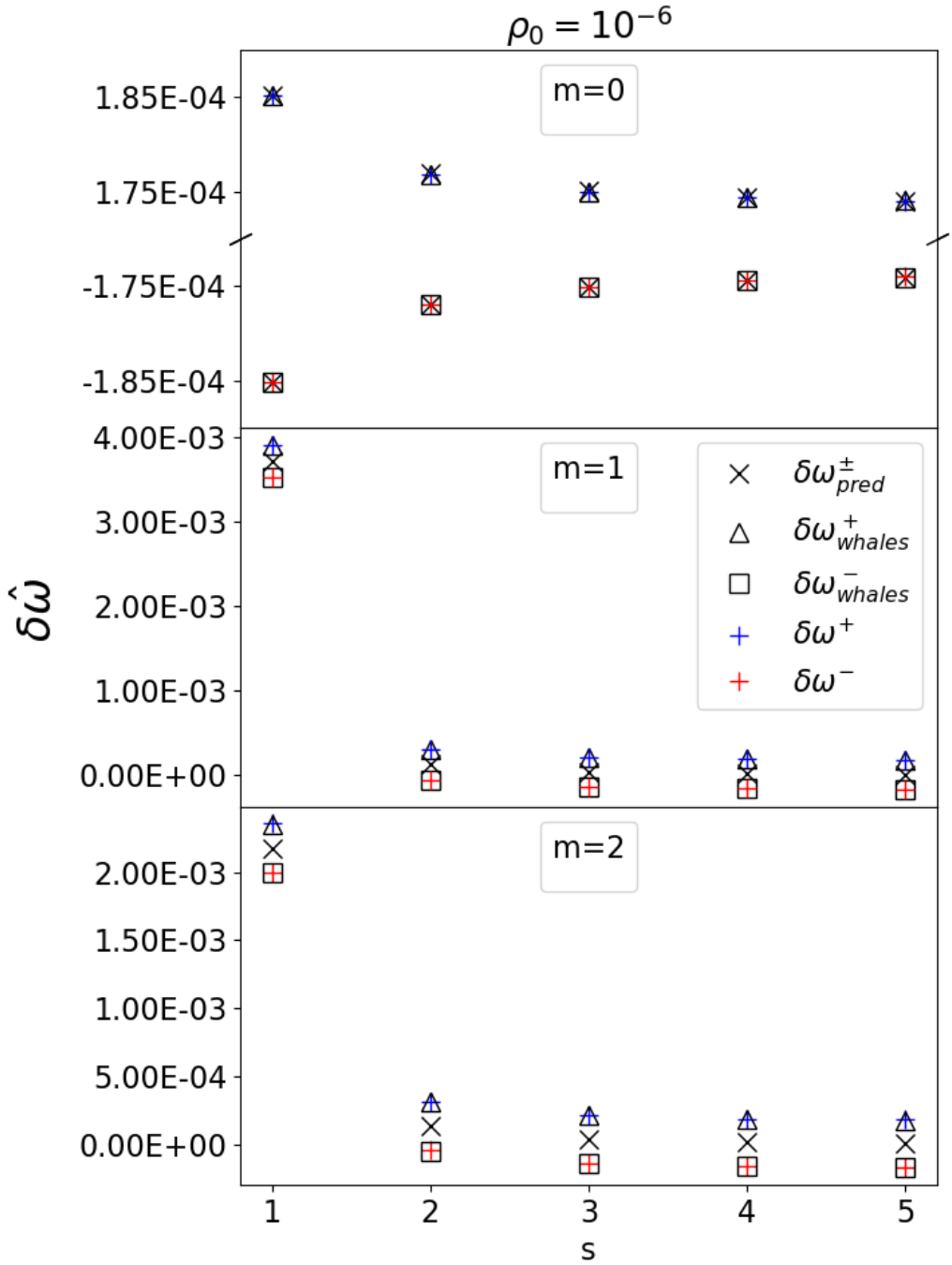

Figure 4.4: The same setup as Fig. 4.3 is used with the single change $\rho_0 = 10^{-6}$ kgm^{-3}, giving increased Hall term strength.

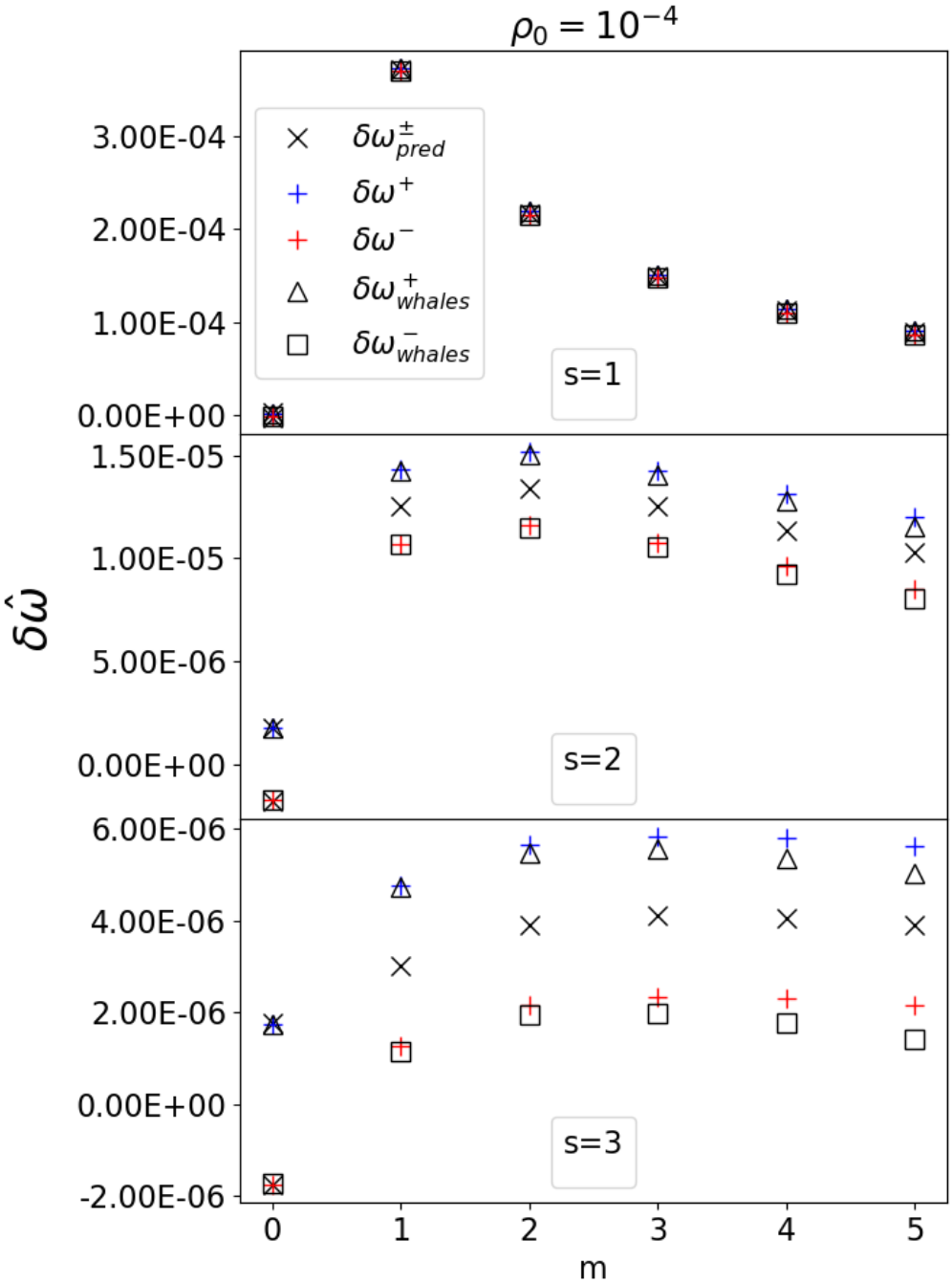

Figure 4.5: CAE dispersion relations plotted in the poloidal mode number m for $s = 1, 2, 3$, constructed using the same parameters as for Fig. 4.3. They show a marked difference between the fundamental harmonic, $s = 1$, and the higher harmonics in the shape of the dispersion relations.

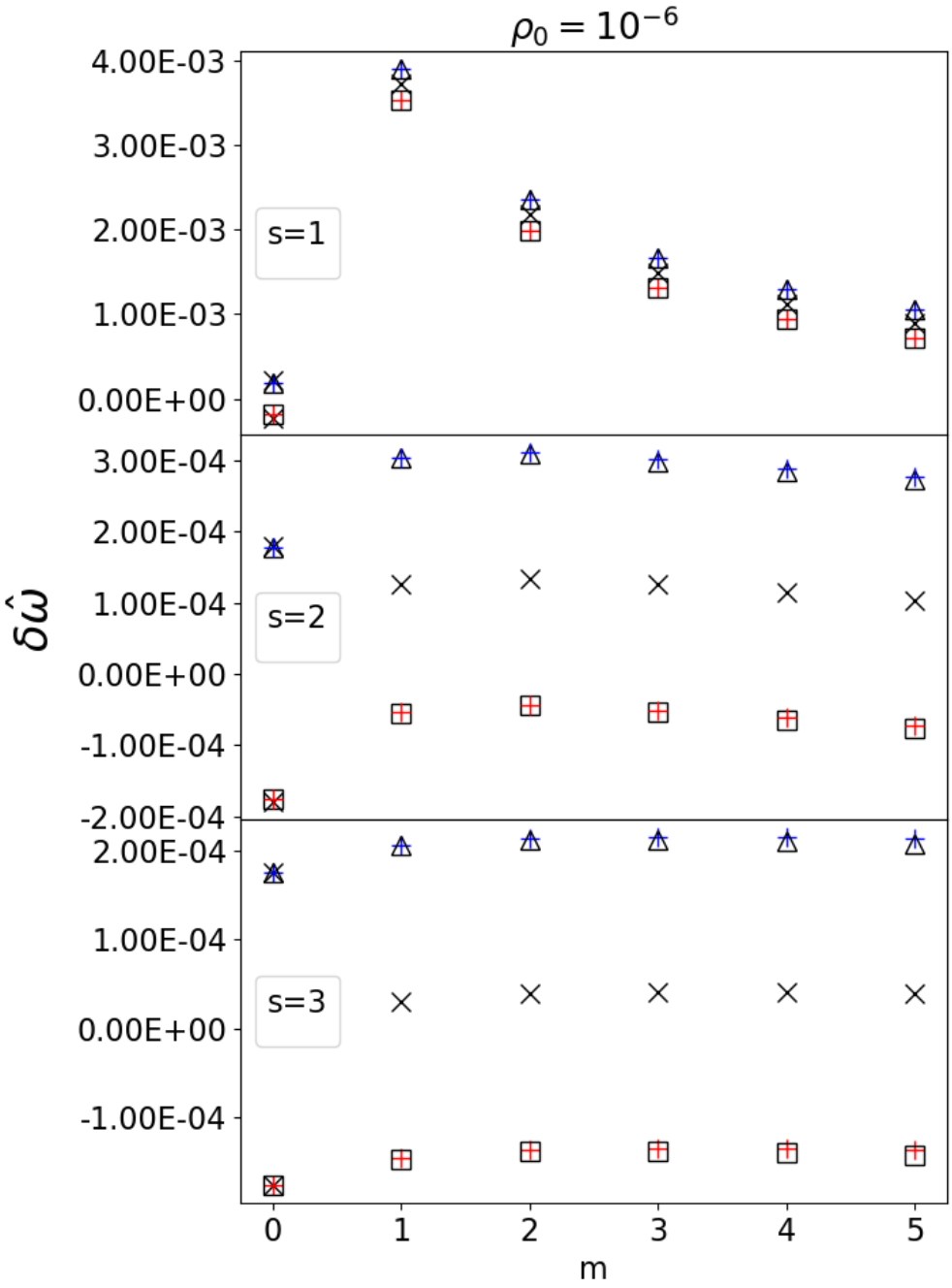

Figure 4.6: The same setup as Fig. 4.5 with the density change $\rho_0 = 10^{-6}$ kgm^{-3}.

relative size of $\delta\omega$ for each eigenmode:

$$\delta\hat{\omega}^{(0)} = \frac{\delta\omega^{(0)}}{\omega_0} = \frac{m_i^2}{2q^2\mu_0}\frac{1}{\rho_0}\frac{\left(j_{0s}'^2 + k^2a^2\right)k^2}{j_{0s}'^2} \ , \tag{4.40}$$

$$\delta\hat{\omega}^{(m)} = \frac{\delta\omega^{(m)}}{\omega_0} = \frac{m_i}{q\sqrt{\mu_0}}\frac{1}{\sqrt{\rho_0}}\frac{k^2a}{(j_{ms}'^2 + k^2a^2)^{\frac{1}{2}}}\frac{m}{j_{ms}'^2 - m^2} \ . \tag{4.41}$$

Measuring this relative change in frequency means that the effects from the Hall term can be seen separately from the change in ideal-MHD frequency. $\delta\hat{\omega}^{(0)}$ and $\delta\hat{\omega}^{(m)}$ have the same positive or negative correlation with each of the six variables listed in Eq. (4.7), though they may differ in the strength of the correlation. For example, neither $\delta\hat{\omega}^{(0)}$ or $\delta\hat{\omega}^{(m)}$ has any term involving the magnetic field B_0. Both are negatively correlated with density, the correlations being $\delta\hat{\omega}^{(0)} \sim \rho_0^{-1}$ and $\delta\hat{\omega}^{(m)} \sim \rho_0^{-1/2}$.

Figs. 4.3-4.6 show dispersion relations in s and m for the normalised Hall corrections as output from Whales2, calculated by:

$$\delta\omega^{\pm}_{whales} = \begin{cases} \frac{\omega - |\omega_0|}{|\omega_0|} & \omega > 0 \\ \frac{\omega + |\omega_0|}{|\omega_0|} & \omega < 0 \end{cases} \tag{4.42}$$

Due to the relative precision required to get an accurate measurement of the Hall correction these eigenmodes were solved for individually using a Shift-and-Invert technique [64] with the corresponding ideal-MHD eigenvalue as the target. $\delta\omega^{\pm}_{pred}$ refers to the predicted Hall corrections in the limit of small h, calculated by Eqs. (4.40)-(4.41) for $\pm|\omega_0|$, where it should be noted that $\delta\omega^{+}_{pred} = \delta\omega^{-}_{pred}$ for $m \neq 0$. $\delta\omega^{+}\backslash\delta\omega^{-}$ are the output Hall corrections obtained via applying a bisection method solver directly to the dispersion relation Eq. (4.22) to solve for $\omega > 0$ and $\omega < 0$ respectively, then proceeding as in Eq. (4.42).

Figs. 4.3-4.4 show that the lower density equilibrium produces a larger normalised Hall correction, as expected. Lower density increases the eigenmode frequency but not the ion-cyclotron frequency, so h increases. Dispersion relations at each density and each m show a negative correlation between s and $\delta\hat{\omega}$. We expect that the Hall correction increases in magnitude with s, since $h \sim \omega \sim s$, but the overall frequency ω is increasing at a higher rate than $\delta\omega$.

The Hall correction predicted by Eq. (4.41) is equal for positive and negative frequency solutions, but Figs. 4.3-4.4 show consistently that $\delta\hat{\omega}^{+} > \delta\hat{\omega}_{pred} > \delta\hat{\omega}^{-} > 0$, for $m \neq 0$, meaning that the negative Hall-MHD solution is closer to the ideal-MHD eigenvalue than the positive solution. In the case of $m = 0$, $\delta\hat{\omega}^{+} = -\delta\hat{\omega}^{-}$ as

we expect.

Figs. 4.5-4.6 also show that a lower density equilibrium produces a larger normalised Hall correction, as expected. The case $m = 0$ is clearly a special case which can be seen by looking at the various dispersion relations - again here $\delta\hat{\omega}^+ = -\delta\hat{\omega}^-$ as we expect. For $m \neq 0$ then the $s = 1$ dispersion relations behave similarly to those in Figs. 4.3-4.4, with the growth in ω with increasing m outpacing that of $\delta\omega$. For $s = 2, 3$ the trends are less steep and seem to be peaked at either $m = 2$ or $m = 3$. We see that $\delta\hat{\omega}^+ > \delta\hat{\omega}_{pred} > \delta\hat{\omega}^- > 0$ for $\rho_0 = 10^{-4}$, but for $\rho_0 = 10^{-6}$ then $\delta\hat{\omega}^- < 0$ for $s = 2, 3$ and so $|\omega^-| > |\omega_0|$ contrary to the analysis done assuming $h \ll 1$.

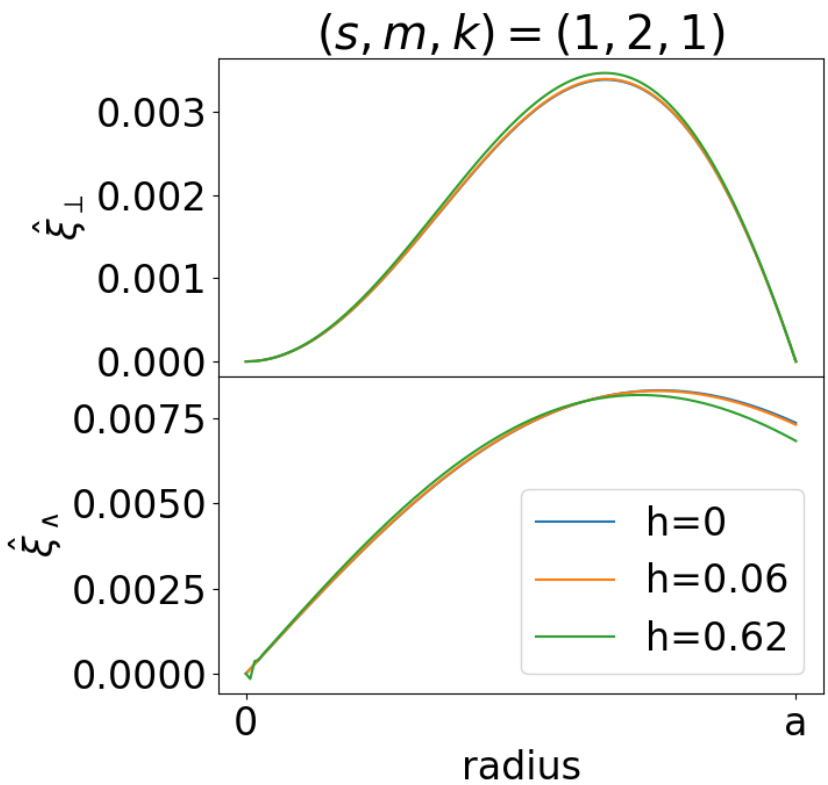

Figure 4.7: The displacement components for the CAE with mode numbers $(s, m, k) = (1, 2, 1)$ whilst varying the strength of the Hall term. The displacement components are almost identical in each case, even with $\omega \sim \omega_{ci}$. The displacement components are normalised so that $|\hat{\xi}_\perp| + |\hat{\xi}_\wedge| = 1$ when summed over the radius. The equilibrium for each mode used $N_\psi = 128$, $N_\theta = 512$, $a = 1$ m, $B_0 = 1$ T. The density for the $h = 0$ and $h = 0.62$ modes is $\rho_0 = 10^{-8}$ kgm^{-3} and for the $h = 0.06$ mode $\rho_0 = 10^{-6}$ kgm^{-3} was used.

We do not expect that the inclusion of the Hall term will affect the eigenfunctions of the CAEs much for frequencies $|\omega| \lesssim \omega_{ci}$, as the effect on the magnitude of the frequency is small as shown in Figs. 4.3-4.6. Fig. 4.7 shows a particular CAE

for different values of h. It is clear from inspecting Fig. 4.7 that the eigenmode structure is indeed only slightly affected by inclusion of Hall effects for moderate values of h.

4.2 Inhomogeneous θ-pinch

We introduce a radial density profile to make the cylinder inhomogeneous. This means that the Alfvén frequency now has a radial profile, so the infinitely degenerate shear Alfvén eigenmode becomes a continuum with each mode localised to a flux surface oscillating at the local Alfvén frequency. Coupling of the CAEs to the shear Alfvén continuum is possible in this regime.

The radial profiles of the CAEs can be affected by the density profile which means labelling each mode with the quantum numbers (s, m, k) is less straightforward than in the homogeneous cylinder. For the homogeneous cylinder the CAE structures were such that the number of anti-nodes in the $\tilde{\xi}_\perp$ component were equal to the quantum number s for that mode. However, the density profile may affect the number of nodes/anti-nodes for each perturbed quantity and so there is no simple mapping procedure between anti-nodes and harmonics. We propose that in order to label each mode that they are related back to their equivalent mode in the homogeneous cylinder through slow deformation of the density profile, as shown in Fig. 4.8. We introduce the following density profile:

$$\rho_0(r) = \rho_0(0)\left(1 - \alpha\frac{r^2}{a^2}\right) \ , \ \alpha \in (0,1) \ , \tag{4.43}$$

to be used throughout this section.

Ideal-MHD

To reach a particular inhomogeneous equilibrium from the homogeneous one we can alter the density profile (4.43) by varying α until reaching the desired profile. In Fig. 4.8 shows the infinitely degenerate shear Alfvén mode for $\alpha = 0$ transformed into a continuum as α is increased to $\alpha = 0.9$. The Alfvén speed increases outwards from the magnetic axis, where V_A is constant against any change in α. The shear Alfvén modes form a continuum from the maximum Alfvén frequency at $\omega_A^2(a)$ to an accumulation point at the minimum frequency $\omega_A^2(0)$. The accumulation point occurs at the radial point where $d\omega_A/dr = 0$. The CAEs display an increasing frequency as α increases due to the increased average Alfvén speed, and the dashed lines in Fig. 4.8 follow the evolution of each radial harmonic with increasing α.

Fig. 4.8 also shows the difference in radial structure of the displacement components for the $s = 1$ mode at $\alpha = 0$ and the equivalent mode at $\alpha = 0.9$.

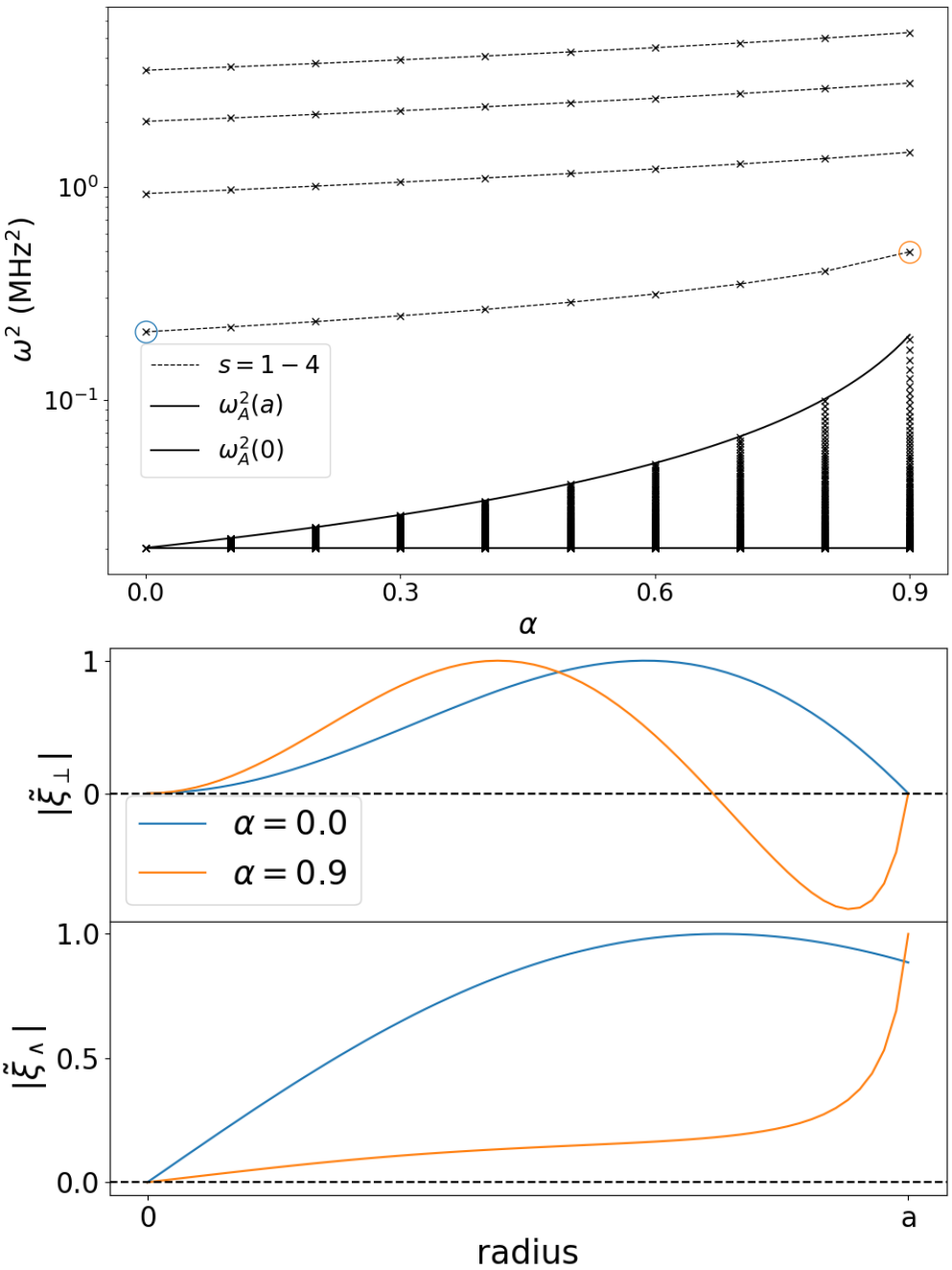

Figure 4.8: Dispersion relations for the first four CAE harmonics as well as the spectrum of Shear Alfvén modes are shown for an evolving density profile (4.43). The structure of the displacement components for the $(s, m, k) = (1, 2, 1)$ CAE at the extreme values of α are plotted below. The equilibrium values are $B_0 = 1$ T, $a = 1$ m, $\rho_0(0) = 10^{-6}$ kgm^{-3} with Whales2 parameters $N_\psi = 64$, $N_\vartheta = 512$, using a cubic-quadratic finite elements scheme.

CAEs may also develop a radially localised structure, depending on the particular density profile and the wavenumber of the eigenmode. Coppi et al [76] derived the following equation to describe the perturbed parallel magnetic field in a θ-pinch with a density profile. They assumed that the wave vector is dominated by the azimuthal component, i.e. $|\boldsymbol{k}| \approx m/r$. This is achieved for a sufficiently large value of the poloidal wave number m.

$$\frac{1}{r}\frac{\partial}{\partial r}\left(r\frac{\partial b_{\parallel}}{\partial r}\right) = W(r)b_{\parallel} \ , \tag{4.44}$$

with

$$W(r) = \left(\frac{m^2}{r^2} - \frac{\omega^2}{V_A^2(0)}\frac{\rho_0(r)}{\rho_0(0)}\right) \ , \tag{4.45}$$

for a parallel perturbed magnetic field of the form: $b_{\parallel}(\boldsymbol{r},t) = b_{\parallel}(r)e^{i(k_{\parallel}z+m\theta-\omega t)}$. Coppi then identified $W(r)$ on the RHS of Eq. (4.44) as an 'effective potential' acting on the parallel perturbed magnetic field. This term can also be identified with the radial wavelength as $W \sim -k_r^2$. Therefore, wave solutions that are oscillatory in the radial direction exist for $W < 0$, and for $W > 0$ the waves are evanescent. We substitute the density profile (4.43) into $W(r)$ to obtain:

$$W(r) = \frac{m^2}{r^2} - \frac{\omega^2}{V_A^2(0)}\left(1 - \alpha\frac{r^2}{a^2}\right) \ , \tag{4.46}$$

For a flat density profile, $\alpha = 0$, then $W(r)$ is a monotonically decreasing function (unless $m = 0$ in which case $V(r)$ is flat) and so the condition to satisfy $W(r) = 0$ within the plasma cylinder is:

$$r_0 = \frac{|m|V_A(0)}{|\omega|} < a \ . \tag{4.47}$$

As $|m|$ increases, the domain over which oscillatory solutions can exist moves away from the plasma centre, or the frequency of the mode increases in magnitude. When $\alpha \neq 0$ then $W(r)$ is no longer monotonic and so may have a local minimum within plasma cylinder, given by:

$$\left.\frac{\partial W}{\partial r}\right|_{r_{loc}} = 0 \quad \Rightarrow \quad r_{loc} = \left(\frac{m^2a^2V_A^2(0)}{\alpha\omega^2}\right)^{\frac{1}{2}} \ . \tag{4.48}$$

We substitute the approximation for the frequency given by [76]:

$$\omega^2 \simeq V_A^2(0)\frac{\rho_0(0)}{\rho_0(r_{loc})}\frac{m^2}{r_{loc}^2} \ , \tag{4.49}$$

into (4.48), which then coincides with the expression for the radius of localisation given by [76]:

$$r_{loc} = -2\left(\frac{\partial \ln\left(\rho_0(r)/\rho_0(0)\right)}{\partial r}\right)^{-1}_{r=r_{loc}} \ . \tag{4.50}$$

applied to the density profile (4.43). The predicted values for the frequency and localisation radius become:

$$r_C = \frac{a}{\sqrt{2\alpha}} \ , \tag{4.51}$$

$$\omega_C = V_A(0)\frac{m}{a}\sqrt{\alpha} \ . \tag{4.52}$$

In contrast, Mahajan and Ross [77] manipulated the zero plasma-β ideal-MHD wave equation in terms of a modified variable related to the perturbed radial electric field. They make the assumption $k_\perp = \frac{m}{r} \gg k_\parallel$ to identify a "Schrodinger-like" equation:

$$\frac{\partial^2\zeta}{\partial r^2} + \left[\frac{\omega^2}{V_A^2(0)}\frac{\rho_0(r)}{\rho_0(0)} - \frac{m^2}{r^2}\right]\zeta = \frac{\partial^2\zeta}{\partial r^2} + \left[\epsilon - V(r)\right]\zeta = 0 \tag{4.53}$$

with $\zeta = \frac{r^{\frac{3}{2}}}{m}\left(\frac{\omega^2}{V_A^2} - k_\parallel^2\right)^{\frac{1}{2}} E_r$ and associated energy and potential:

$$\epsilon = \frac{\omega^2}{V_A^2(0)} \ , \tag{4.54}$$

$$V(r) = \frac{m^2}{r^2} - \frac{\omega^2}{V_A^2(0)}\left(1 - \frac{\rho_0(r)}{\rho_0(0)}\right) \ . \tag{4.55}$$

The radial point of localisation is then given by:

$$r_{loc} = a\left(\frac{m^2}{a^2}\epsilon\right)^{\frac{1}{4}} \ . \tag{4.56}$$

To estimate the frequency Mahajan expands about the minimum potential and truncates the expansion to treat the equation as a simple harmonic oscillator, thereby producing an ODE that can be solved to give the eigenmode structure and the frequency. Applying this method for the density profile (4.43) gives the following

frequency and localisation radius [77]:

$$r_M = \frac{a}{\sqrt{2\alpha}}\left(\frac{m}{m+1+2s}\right)^{\frac{1}{2}} , \tag{4.57}$$

$$\omega_M = V_A(0)\frac{2(m+1+2s)}{a}\sqrt{\alpha} . \tag{4.58}$$

We compare the Coppi and Mahajan models, noting that $r_M \to r_C$ and $\omega_M \to 2\omega_C$ in the limit $m \to \infty$. A comparison between these two models and the output from Whales2 is shown in Fig. 4.9. We used a high m value ($m = 50$) against the low parallel wavenumber $k = 1$ to satisfy that assumption of the Coppi and Mahajan models. Fig. 4.9 shows the the Mahajan model has good agreement with

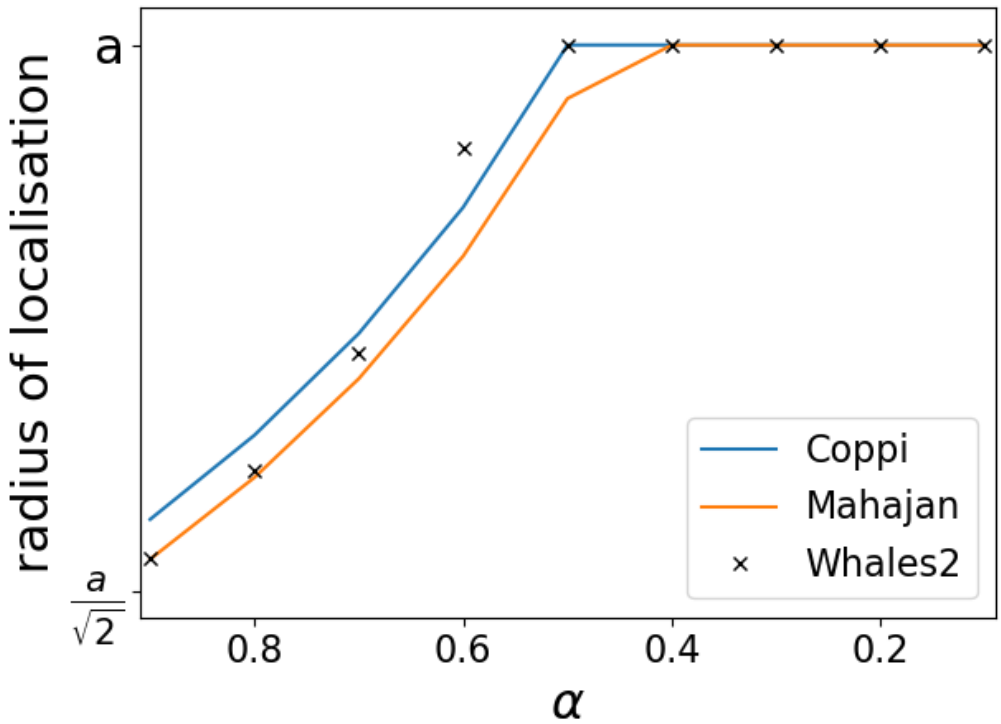

Figure 4.9: The radius of localisation for the density profile Eq. (4.43) is plotted against α. As α decreases towards $\alpha = 0$, the radius of localisation moves towards the outer wall. When either model predicts that the localisation radius exceeds the outer wall, which occurs in both models for $\alpha < 0.5$, we say that the outer wall is the radius of localisation. The radius of localisation is determined from the output of Whales2 by numerically calculating the point at which the global maximum occurs. The grid sizes are $N_\psi = 128$ and $N_\vartheta = 1024$, with physics parameters $\rho_0(0) = 1.0 \times 10^{-8}$ kgm^{-3}, $a = 1.0$ m, $B_0 = 1.0$ T, $(s, m, k) = (1, 50, 1)$ and using finite elements order Cubic-Quadratic.

Whales2 for large values of α whereas Coppi agrees better as the localisation moves towards the outer wall. Whales2 predicts a much faster movement of the radius of localisation towards the outer wall as α increases than either model, which is possibly due to the simplifying assumptions made in each model. Fig. 4.10 shows a typical mode with poloidal mode number $m = 50$ alongside a mode with $m = 2$. The radial localisation of the $m = 50$ can be clearly seen.

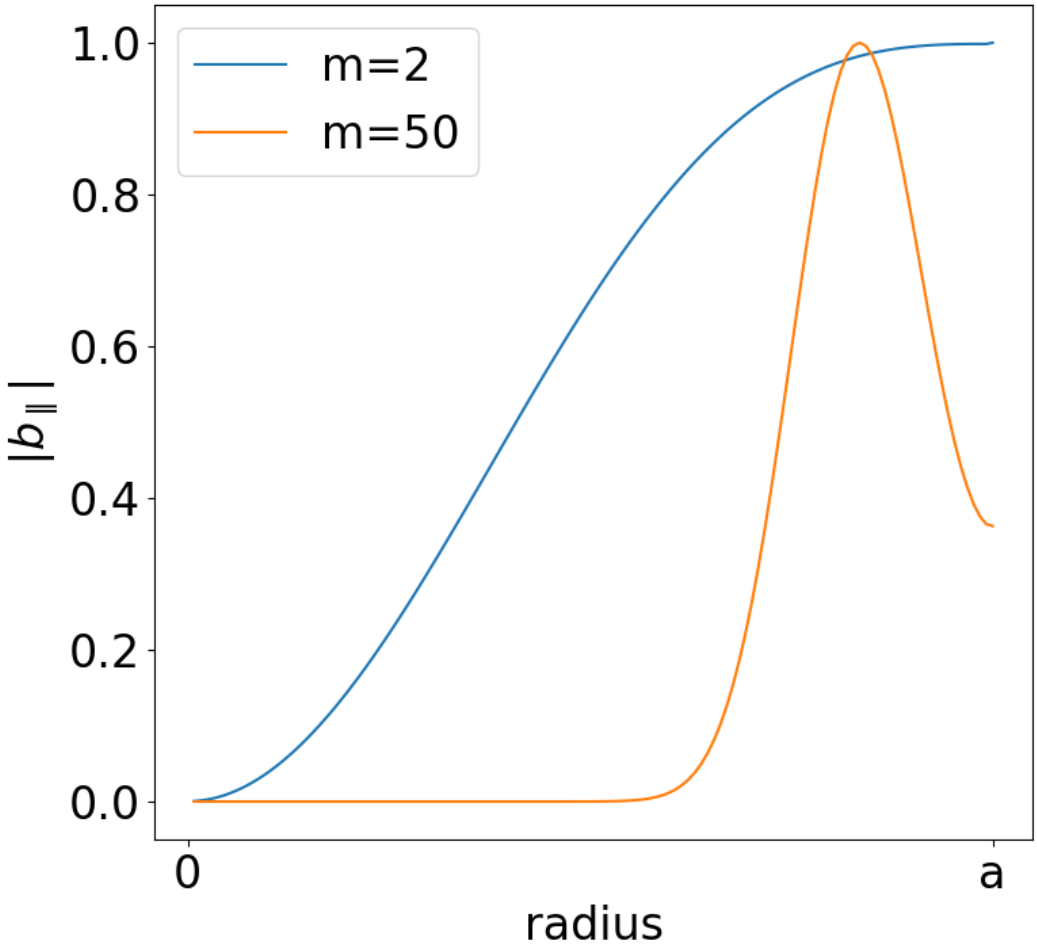

Figure 4.10: The radial structure for CAEs with poloidal mode numbers $m = 2$ and $m = 50$, for $\alpha = 0.7$. The parameters used are $N_\psi = 128$, $N_\vartheta = 1024$, $\rho_0(0) = 1.0 \times 10^{-8}$ kgm^{-3}, $a = 1.0$ m, $B_0 = 1.0$ T, $s = 1$, $k = 1$. The same equilibrium was used in the calculation of both modes.

Hall-MHD

The inclusion of the Hall terms in the linearised MHD equations gives an asymmetry in the solutions with respect to the sign of the poloidal mode number m, as discussed in the previous section. The following equation describes the linearised Hall-MHD equations acting on the parallel perturbed magnetic field, with the assumption $m \gg 1$ [78]:

$$\frac{\partial^2 b_\parallel}{\partial r^2} = \left(\frac{m^2}{r^2} - \frac{\omega^2}{V_A^2(r)} + \frac{m}{r}\frac{\omega}{\omega_{ci}}\frac{\rho'(r)}{\rho(r)} \right) b_\parallel \ . \tag{4.59}$$

We again denote the bracketed term as $W(r)$ and note that in the limit $h \to 0$ then $W(r)$ is the same as in the Coppi model for ideal-MHD. The additional Hall term in $W(r)$ contains an odd function of m, hence breaks the $\pm m$ symmetry. We can consider only $\omega > 0$ for $\pm m$ without loss of generality. For the density profile (4.43), $W(r)$ becomes:

$$W = \frac{m^2}{r^2} - \frac{\omega^2}{V_A^2(0)} + \alpha \frac{\omega^2}{V_A^2(0)}\frac{r^2}{a^2} - \frac{m}{a^2}\frac{\omega}{\omega_{ci}}\frac{2\alpha}{1-\alpha\frac{r^2}{a^2}} \ , \tag{4.60}$$

$$\frac{\partial W}{\partial r} = \frac{-2m}{r^3} + \alpha \frac{\omega^2}{V_A^2(0)}\frac{2r}{a^2} + \frac{mr}{a^4}\frac{\omega}{\omega_{ci}}\frac{4\alpha^2}{\left(1-\alpha\frac{r^2}{a^2}\right)^2} \ . \tag{4.61}$$

Eq. (4.60) shows that W has a lower value for $m > 0$ than $m < 0$ and so the threshold to have oscillatory solutions, $W < 0$, is lower for positive m than negative m, suggesting that when $m < 0$ the frequency of the CAEs will be higher than for the corresponding $m > 0$ modes. Fig. 4.11 shows the output from Whales2 for $s = 1, 2, 3$, $m = \pm 50$, $\alpha \in \{0.0, 0.1, \ldots, 0.9\}$. The dispersion relations show that clearly for all $\alpha > 0$, the frequency is indeed higher for the negative m modes. Looking at the structure of the parallel perturbed magnetic field, Fig. 4.11 also shows that for $\alpha = 0.9$ the $m = 50$ modes are localised further towards the outer wall than their $m = -50$ counterparts. It appears that in the case of high α the Hall term has a much more significant impact of the radial structure of the CAEs than for a flat density profile.

4.3 Twisted Magnetic Field

We now introduce a radial profile for the magnetic field $\boldsymbol{B}_0$. Previously we only required an axial magnetic field component but with the introduction of a radial profile we need either a non-zero pressure with a non-constant radial profile or a poloidal component of the magnetic field in order to satisfy the force balance,

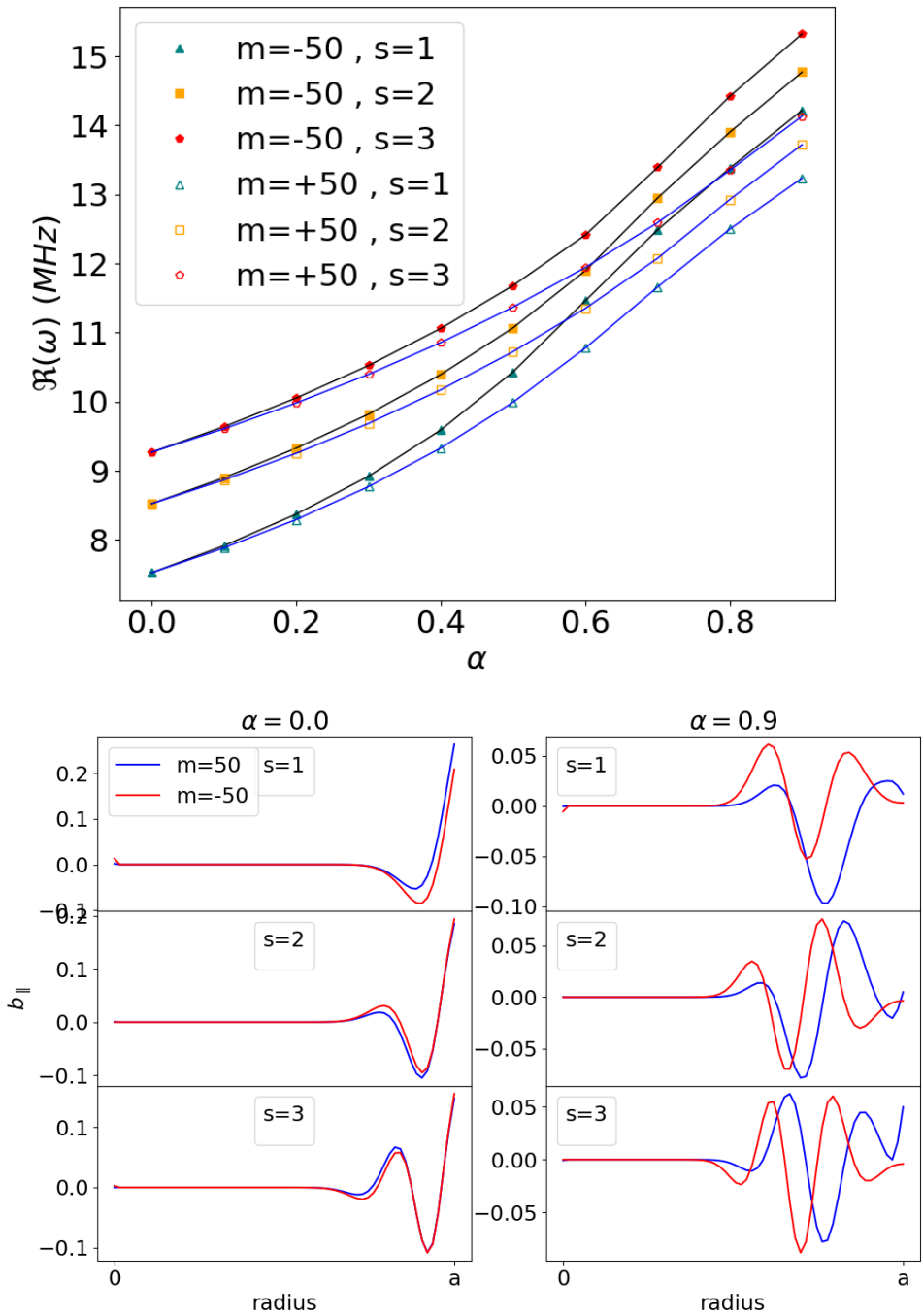

Figure 4.11: Dispersion relations for six CAEs, calculated by Whales2 in the Hall-MHD regime, are shown with frequency plotted against α as defined by Eq. (4.43). The structures of $b_\parallel$ for a subset of modes is shown below. These modes have equilibrium parameters $B_0 = 1$ T, $a = 1$ m, $\rho_0(0) = 10^{-6}$ kgm^{-3} and $k = 1$. The solver parameters are $N_\psi = 64$, $N_\vartheta = 1024$ with hybrid-quadratic finite elements order.

Eq. (4.1). We choose the plasma pressure force to remain negligible compared with the magnetic forces. In the limit of the plasma-$\beta \to 0$, the magnetic pressure force is balanced completely by the magnetic tension force arising from a twisted magnetic field.

In a twisted cylinder, the relevant directions become:

$$\boldsymbol{\nabla}\psi = B_\theta \hat{r} \ , \tag{4.62}$$

$$\boldsymbol{T} = \frac{B_z}{B_\theta}\hat{\theta} - \hat{z} \ , \tag{4.63}$$

$$\boldsymbol{B}_0 = B_\theta \hat{\theta} + B_z \hat{z} \ , \tag{4.64}$$

with ψ the poloidal flux function. The CAE wavenumbers in each of these directions are:

$$k_\perp = k_r \sim r \ , \tag{4.65}$$

$$k_\wedge = \frac{1}{iA|\boldsymbol{T}|}\left(\boldsymbol{T}\cdot\boldsymbol{\nabla}\right)A = \frac{B_z}{B_0}\frac{m}{r} - \frac{B_\theta}{B_0}k \ , \tag{4.66}$$

$$k_\parallel = \frac{1}{iAB_0}\left(\boldsymbol{B}_0\cdot\boldsymbol{\nabla}\right)A = \frac{B_\theta}{B_0}\frac{m}{r} + \frac{B_z}{B_0}k \ , \tag{4.67}$$

where A is any perturbed quantity. Note that $k_\wedge^2 + k_\parallel^2 = \frac{m^2}{r^2} + k^2$, as expected, and that these quantities are still independent of the radial mode number s. In analogy with the straight cylinder we expect that ideal-MHD in the twisted cylinder regime is unchanged under the transformation $k_\parallel \to -k_\parallel$ and that $k_\wedge \to -k_\wedge$ affects only the relative signs of $\tilde{\xi}_\perp$ and $\tilde{\xi}_\wedge$. Hall-MHD is expected to remain unchanged with respect to $k_\parallel \to -k_\parallel$, but under $k_\wedge \to -k_\wedge$ we expect that the mode frequency will change. We also expect that there will be a symmetry with respect to the substitution $(\omega, k_\wedge) \to (-\omega, -k_\wedge)$. We explore these properties using a particular form for the magnetic field that has constant magnetic field strength over the cylinder:

$$\boldsymbol{B}_0 = B_{\theta a}\frac{r}{a}\hat{\theta} + \left(B_{z0}^2 - B_{\theta a}^2\frac{r^2}{a^2}\right)^{\frac{1}{2}}\hat{z} \ , \tag{4.68}$$

which has strength $B_0 = B_{z0}$. In order to achieve $k_\wedge \to -k_\wedge$ whilst $k_\parallel$ remains constant we can either apply $(B_z, k) \to (-B_z, -k)$ or $(B_\theta, m) \to (-B_\theta, -m)$. To avoid $\psi < 0$ we choose the former. Similarly to achieve $k_\parallel \to -k_\parallel$ we substitute $(B_z, m) \to (-B_z, -m)$. Fig. 4.12 shows the dispersion relations of two CAEs against a changing poloidal magnetic field strength with these transforms applied. Under ideal-MHD all frequencies are the same despite the sign of the wavenumbers, as

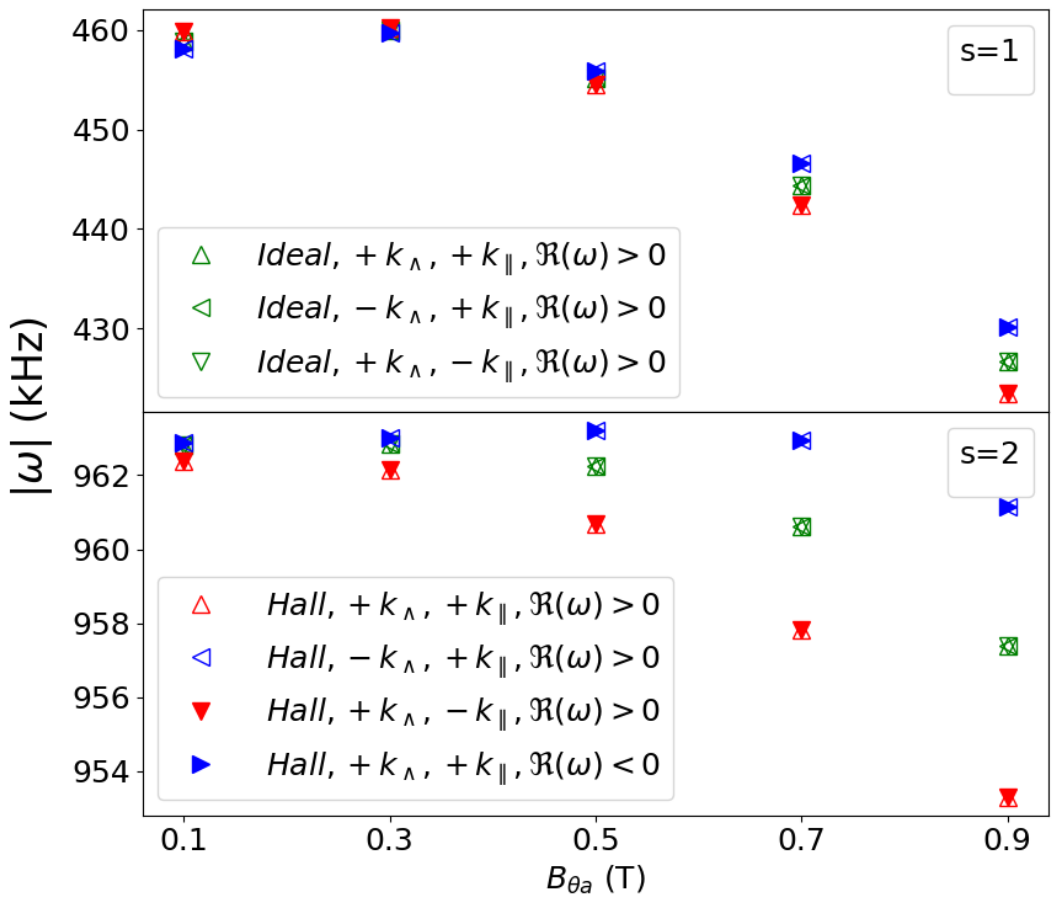

Figure 4.12: Shown are dispersion relations for the two lowest CAE harmonics against $B_{\theta a}$ using the magnetic field profile (4.68). We used parameters $|m| = 2$, $|k| = 1$, $B_{z0} = 1$ T, $a = 1$ m and $N_\psi = 64$, $N_\vartheta = 1024$ with a Cubic-Quadratic finite elements scheme for the ideal-MHD modes and Hybrid Quadratic scheme for the Hall-MHD modes.

expected. For Hall-MHD we see that $\omega(k_\wedge, k_\parallel) = \omega(k_\wedge, -k_\parallel)$ and that $\omega(-k_\wedge, k_\parallel) = -\omega(k_\wedge, k_\parallel)$, which is analogous to the Hall-MHD modes in a straight cylinder with wavenumbers m, k.

We introduce the *pitch* of the magnetic field, defined in the cylinder as [26]:

$$\mu(r) = \frac{B_\theta(r)}{rB_z(r)} \ , \tag{4.69}$$

and its inverse, the *safety factor*: $q(r) = \mu^{-1}(r)$. We define a magnetic field profile

that has constant pitch:

$$\boldsymbol{B}_0 = B_{z0}\frac{\mu r}{1+\mu^2 r^2}\hat{\theta} + \frac{B_{z0}}{1+\mu^2 r^2}\hat{z} \ , \tag{4.70}$$

$$|\boldsymbol{B}_0| = \frac{B_{z0}}{(1+\mu^2 r^2)^{\frac{1}{2}}} \ , \tag{4.71}$$

and satisfies Eq. (4.1) for a zero-pressure equilibrium. The magnetic field strength for this configuration is clearly non-constant and so both the Alfvén speed and the ion-cyclotron frequency have a radial profile, meaning that the parameter $h = \omega/\omega_{ci}$, which acts as a proxy for measuring the relative strength of the Hall effects, varies over the radial domain. For the particular magnetic field strength (4.71) the Hall parameter will have its minimum on the magnetic axis and maximum at the outer wall. Fig. 4.13 compares the ideal- and Hall-MHD solutions for a particular CAE using magnetic field profile (4.70) for two different pitches. The difference in structure for the displacement components $\tilde{\xi}_\perp$ and $\tilde{\xi}_\wedge$ between the ideal and Hall modes is not particularly pronounced in either case, but the parallel perturbed magnetic field $b_\parallel$ has significantly differences for ideal and Hall near to the magnetic axis for both pitches. These differences can be attributed to the changing relative strengths of $\tilde{\xi}_\perp$ and $\tilde{\xi}_\wedge$, which can be seen in Fig. 4.13. Fig. 4.13 uses the same normalisation as Fig. 4.7, i.e. $|\tilde{\xi}_\perp| + |\tilde{\xi}_\wedge| = 1$ when summed over the radius.

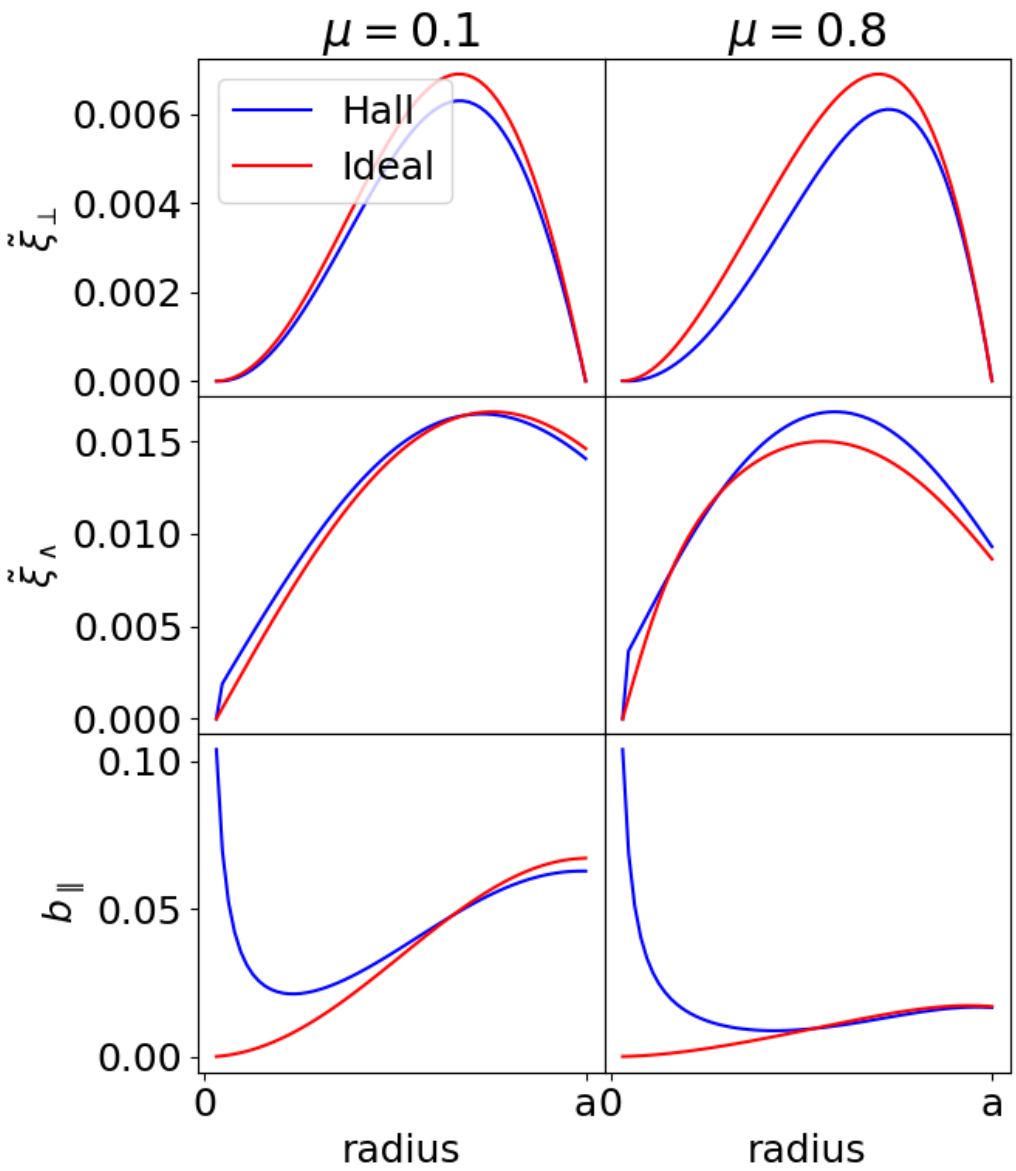

Figure 4.13: The radial structure of the $(s, m, k) = (1, 2, 1)$ CAE is shown for both ideal- and Hall-MHD. The different pitches give different ranges for the Hall strength parameter $h(r)$. The low pitch $\mu = 0.1$ implies $h \in [0.426, 0.428]$, and the high pitch $\mu = 0.8$ gives $h \in [0.389, 0.498]$. We used parameters $m = 2$, $k = 1$, $B_{z0} = 1$ T, $a = 1$ m, $\rho_0(0) = 2.0 \times 10^{-8}$ kgm^{-3} and $N_\psi = 64$, $N_\vartheta = 512$ with a Cubic-Quadratic finite elements scheme for the ideal-MHD modes and Hybrid Quadratic scheme for the Hall-MHD modes.

Chapter 5

Axisymmetric toroidal geometry

We use the following co-ordinate system to describe a plasma torus: $(\sqrt{\psi}, \phi, \vartheta)$. The radial variable, $\sqrt{\psi}$, and the poloidal variable, ϑ, are each orthogonal to the toroidal angle, ϕ, but not necessarily to each other. The co-ordinate system is linked to the magnetic flux surfaces as the direction $\boldsymbol{\nabla}\psi$ describes the outward normal to the flux surfaces. The poloidal direction is defined as the direction within each flux surface that is orthogonal to the toroidal direction.

The most significant change introduced to the linearised MHD equations by the toroidal geometry is the loss of poloidal symmetry. In a tokamak the magnetic field is inversely proportional to the major radius, i.e. $B_0 \sim 1/(R_0 + r\cos\theta)$. This poloidal dependence causes coupling in the linearised MHD equations, Eqs. (3.13)-(3.16), between the poloidal Fourier harmonics. Plasma shaping, such as triangularity and ellipticity, also causes poloidal coupling. Therefore, there is no longer a well-defined notion of the poloidal quantum number m which we have been using to describe modes. We now use the full expression (3.15) for the discretised displacement components, i.e.:

$$\tilde{\xi}^{NM}_{\perp/\wedge} = \sum_{l=m-M}^{m+M} \sum_{j=0}^{n_r} \hat{\xi}^{jl}_{\perp/\wedge} H^{j}_{\perp/\wedge}(s) e^{i(l\vartheta + n\phi - \omega t)} \ , \tag{5.1}$$

We note that for the continuous MHD wave equations then $l \in [-\infty, \infty]$, but this is truncated for the discretised equations. We propose using a classification convention as in [3], where each mode is related back to the equivalent mode in the large aspect ratio circular tokamak by a gradual decreasing of the shaping parameters and increasing of the aspect-ratio. The 'quantum number' m of the low aspect-ratio mode is given by the large aspect-ratio equivalent as it becomes well-defined in the cylindrical limit. The integer value of s is similarly designated by the equivalent

number in the limit of the homogeneous cylinder, as discussed in Section 4.2. The toroidal quantum number n is given by a single Fourier harmonic, so remains well-defined. The displacement components (5.1) are only suitable for studying the central Fourier harmonic with poloidal mode number m. Harmonics near the edge of the truncation, such as $m \pm M$, are not well represented as their potential poloidal couplings are asymmetric. One way to observe the change of a particular CAE through lowering aspect ratio and increased shaping is to look at the relative mode power of each poloidal Fourier harmonic:

$$|\hat{\xi}^l|^2 = \sum_{j=0}^{n_r} \left(|\hat{\xi}_\perp^{jl}|^2 + |\hat{\xi}_\wedge^{jl}|^2 \right) \ . \tag{5.2}$$

We expect that in the circular, large aspect-ratio case the power spectrum will be dominated by $\hat{\xi}^m_{\perp/\wedge}$, but mode couplings introduced through the plasma shape and equilibrium will redistribute some of the mode power to the wings of the spectrum. For example, toroidicity introduces an $l \pm 1$ coupling and so we expect that the power spectrum is peaked at $l = m$ whilst monotonically decreasing away from this point. Ellipticity introduces an $l \pm 2$ coupling and so we expect to see local peaks at $l = 0, \pm 2, \pm 4, \ldots$ that decrease in amplitude as the distance from m increases. Triangularity causes $l \pm 3$ coupling. Output from Whales2, presented in Fig. 5.1, demonstrates these couplings can be seen when introducing each shaping parameter independently. The same couplings are present in the Hall term corrections to the ideal-MHD equations, just scaled by $h = \omega/\omega_{ci}$ as all the Hall term corrections are. Therefore, the presence of the Hall terms in the MHD equations does little to modify the poloidal coupling strengths, as can be seen in Fig. 5.1.

Another consequence of the poloidal Fourier coupling is that we must consider an Alfvén continuum for each poloidal harmonic. We write:

$$\omega_A^{(l)} = V_A k_\parallel^{(l)} \ , \tag{5.3}$$

for $l \in [-\infty, \infty]$. As $l \to \infty$ then $|k_\parallel^{(l)}| \to \infty$. Therefore, in the continuous MHD equations the Alfvén continuum effectively extends to infinite frequency, though for the truncated Fourier series such that $l \in [m-M, m+M]$ there is a maximum Alfvén frequency. The possibility exists that a CAE with particular dominant poloidal wavenumber m_1 may be continuum damped by a shear Alfvén mode with a different dominant poloidal mode, m_2. This can be seen in Fig. 5.2 where the CAE has the characteristics of an $m = 1$ mode but there is coupling to a shear Alfvén mode that has dominant poloidal wavenumber $m = 2$. The continuum coupling can clearly

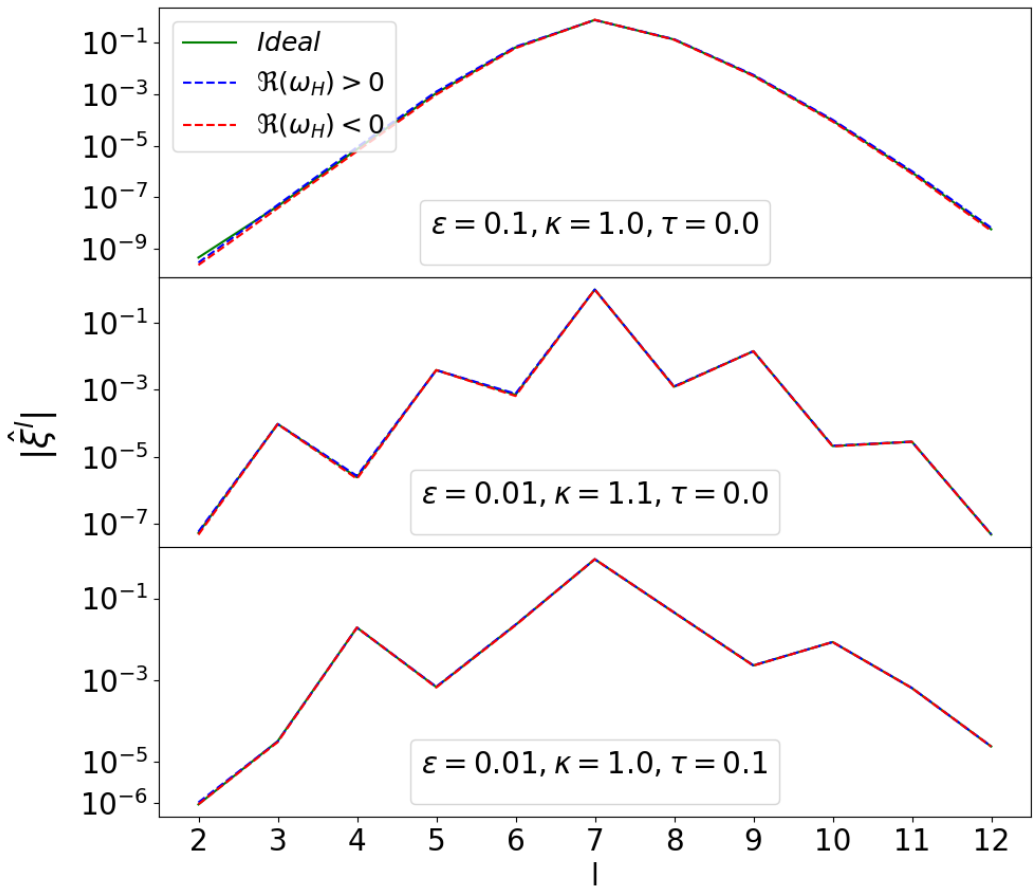

Figure 5.1: The poloidal Fourier harmonic couplings that arise from different plasma shaping effects in output from Whales2 with $m = 7$ and $M = 5$. The top, middle and bottom plots show the effects of toroidicity, ellipticity and triangularity. Each behaves as expected with local peaks at $l \in \{7\}$, $l \in \{3, 5, 7, 9, 11\}$ and $l \in \{4, 7, 10\}$ respectively. Comparison between the ideal-MHD output (solid) and the Hall-MHD output (dashed) for the equivalent mode indicates that the Hall terms do not significantly modify the poloidal coupling. The other Soloviev parameters used in each case are: $B_0(0) = 1$ T, $E = 1$, $F = 0$, $\rho_0 = 10^{-6}$ kgm^{-3}, $n = 10$. Also, $N_\psi = 64$, $N_\vartheta = 512$ and hybrid-quadratic finite elements are used.

be seen as a localised spike in the displacement in both the 2d cross-section plot and the radial plot of the poloidal harmonics in the case when the shear terms are included in the MHD equations. The localised spike is absent when the shear terms are neglected, confirming that it is a product of the CAE coupling to the shear Alfvén continuum. Though the coupling to the shear continuum is physical, it is clearly undesirable in the study of CAE spatial structure as they become dominated by the localised shear mode. Fig. 5.2 illustrates that the option to switch off the shear terms, though it slightly modifies the underlying CAE, is a useful tool to

study 'pure' CAEs in Hall-MHD without having to add dissipation to remove the continuum coupling.

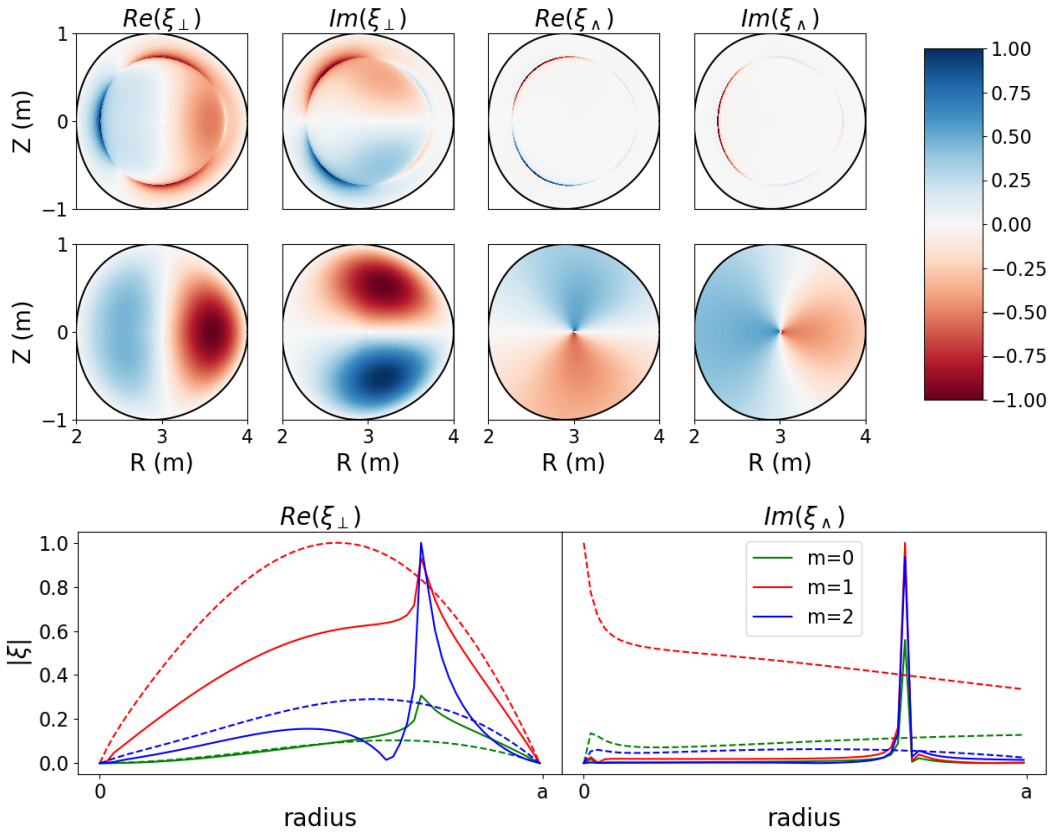

Figure 5.2: The 2d structure of the $\perp$ and $\wedge$ displacement components is shown for a mode calculated using Whales2, with shear terms included (top row) and neglected (bottom row). Also shown is the radial structure of the displacement components for each Fourier harmonic for both cases: *with shear* (solid lines) and *without shear* (dashed lines). The Soloviev parameters used are: $B_0(0) = 1.0$ T, $a = 1.0$ m, $R_0 = 3.0$ m, $\kappa = 1.0$, $\tau = 0.1$, $E = 1$, $F = 0$, $\rho_0 = 10^{-6}$ kgm^{-3}, $s = 1$, $m = 1$, $M = 1$, $n = 4$.

We re-examine the heuristic dispersion relation Eq. (4.16) which becomes, in a toroidal geometry:

$$\omega^2 \simeq \bar{V}_A^2 \left(\frac{s^2}{L_r^2} + \frac{m^2}{a^2} + \frac{n^2}{R_0^2} \right) , \tag{5.4}$$

where $\bar{V}_A$ is the average Alfvén speed. For the purposes of comparison with output from Whales2, we again determine the unknown quantity L_r by specifying that the predicted frequency of Eq. (5.4) matches the output from Whales2 for the fundamental harmonic $(s, m, n) = (1, 1, 1)$. Fig. 5.3 shows the comparison between

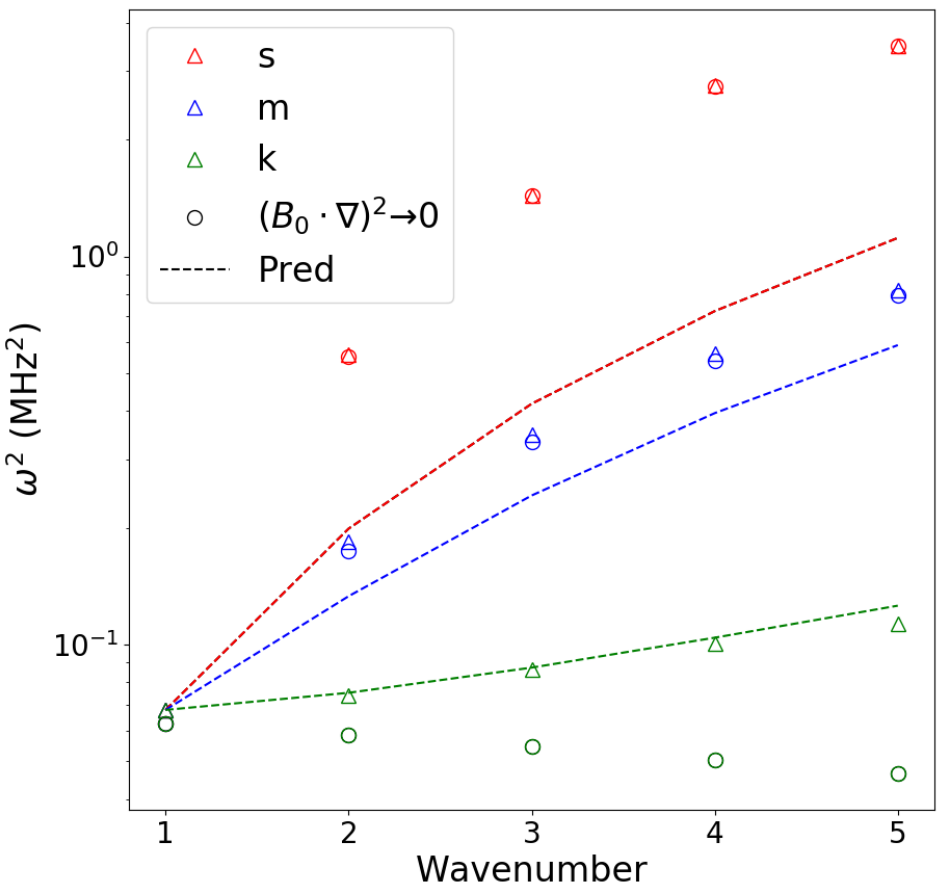

Figure 5.3: The dispersion relations for CAEs in a toroidal configuration, plotting squared frequency against the 'quantum numbers' s, m and n. The equilibrium parameters are $a = 1.0$ m, $R_0 = 10.0$ m, $B_0 = 1.0$ T, $\rho_0 = 10^{-6}$ kgm^{-3}, $E = 1$, $F = 0$ for a plasma with a circular cross-section. The heuristic dispersion relation Eq. (5.4) is also plotted (dashed lines) and the CAEs calculated in the absence of shear terms in the MHD equations (circles).

Eq. (5.4) and Whales2. The relations are well matched for the dispersion relation in increasing n but for m and s the gradients of the dispersion relations output from Whales2 are steeper than those predicted by (5.4) meaning that Eq. (5.4) should not be used to make accurate predictions of frequency beyond the lowest s and m numbers. Fig. 5.3 also shows the same dispersion relations output from Whales2 when we neglect the shear terms, i.e. $k_{\|}^2 \to 0$. This has the largest effect for high values of the integer wavenumber n as for this particular configuration high n implies a dominant parallel wavenumber, i.e. $k_{\|} > k_{\perp}$ and $k_{\|} > k_{\wedge}$. In the case of increasing s or m we enter a regime where $k_{\perp} \gg k_{\|}$ or $k_{\wedge} \gg k_{\|}$ respectively, and so the importance of the shear terms in the MHD wave equations are reduced in comparison with other spatial derivatives. For these particular CAEs when calculated

with the shear terms included, the underlying mode structure of the CAE was still obvious and so for simply calculating the frequency there is no need to neglect the shear terms. For cases of larger $k_{\|}$ this may not be true however, as the shear Alfvén mode will come to dominate the spatial structure, making it difficult to identify the particular CAE.

We use Whales2 to calculate a CAE throughout lowering of the aspect-ratio from that of a conventional tokamak to a spherical tokamak configuration, keeping a circular cross-section. In these studies it was necessary to lift the computational domain away from the magnetic axis in order to avoid numerical issues associated with unbounded functions at the geometric singularity. To achieve this we constrained the radial domain to $\left[0.1\sqrt{\psi(a)}, \sqrt{\psi(a)}\right]$.

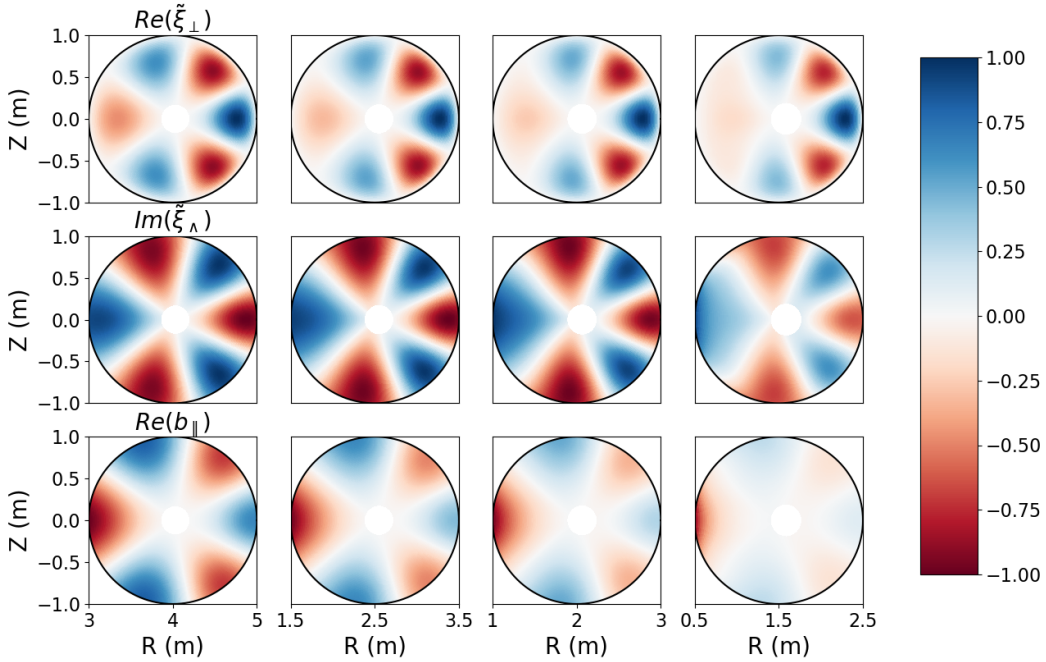

Figure 5.4: The perpendicular displacement component (top), wedge displacement component (middle) and parallel perturbed magnetic field (bottom) are shown for a particular CAE mode. The major radius of the geometry is reduced from left to right, but the plasma shaping is otherwise kept the same. The Soloviev parameters used are: $B_0(0) = 1.0$ T, $a = 1.0$ m, $\kappa = 1.0$, $\tau = 0.0$, $E = 1$, $F = 0$, $\rho_0 = 10^{-6}$ kgm^{-3}, $s = 1$, $m = 3$, $M = 2$, $n = 2$. Also, $N_\psi = 64$, $N_\vartheta = 512$ and cubic-quadratic finite elements are used.

Fig. 5.4 shows the evolution of the displacement components and the parallel component of the perturbed magnetic field for the mode $(s, m, n) = (1, 3, 2)$. The displacement component $\tilde{\xi}_{\perp}$ becomes outboard localised with reduced aspect-ratio whereas $\tilde{\xi}_{\wedge}$ and $b_{\|}$ become inboard localised. Extensions to the theories of radial

localisation for CAEs show that the inclusion of toroidal effects can lead to poloidal localisation of the CAE around either the inboard or the outboard mid-plane [79–81]. Therefore, our observations are in line with the theory. However, since the theories are usually derived with respect solely to a particular component, usually $b_{\|}$, it is unclear whether it is feasible to have different components of the same CAE localised around different poloidal locations. This would suggest that the potential-well has a different form for each component and so to refer to localised CAEs we must refer to which perturbed component is localised. This is also an interesting result as the parallel perturbed magnetic field component, $b_{\|}$, is localised on the inboard side of the tokamak. As noted in Section 1.7 the magnetic pickup coils on MAST are located on the outboard side. Therefore, there may be CAEs that are excited by fast-ions that are inboard localised and the strength of these modes is underestimated or they are missed entirely. Further investigation to see if inboard localised modes can exist in MAST-like geometries and equilibria is warranted.

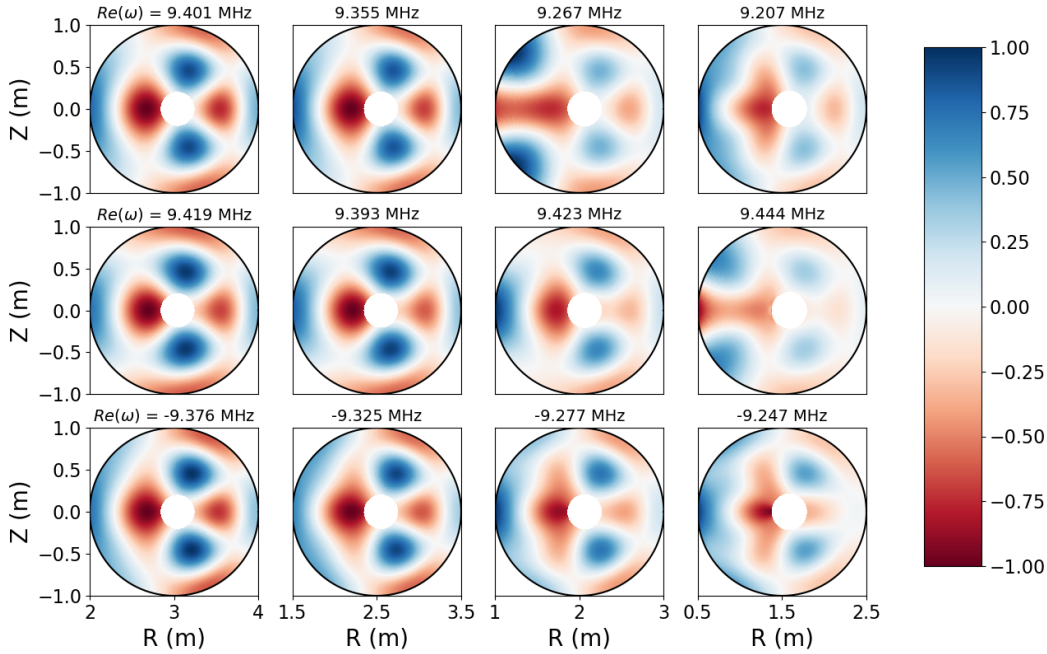

Figure 5.5: The perturbed magnetic field component $b_{\|}$ is shown for a decreasing aspect-ratio from left to right with ideal-MHD CAEs in the top row and Hall-MHD with positive and negative real frequency in the middle and bottom rows respectively. The plasma equilibrium has a circular cross-section and a flat density profile, with $B_0(\mathbf{0}) = 1.0$ T and $\rho_0 = 10^{-8}$ kgm^{-3}. The other equilibrium parameters are $E = 1$, $F = 0$, with mode numbers $m = -2$, $M = 2$, $n = 2$. The ratio of the CAE frequency to the ion-cyclotron frequency on the magnetic axis is approximately: $h_0 = \omega/\omega_{ci}(\mathbf{0}) \sim 2$

We compare the output from Whales2 when solving for the CAE with mode numbers $(s, m, n) = (2, -2, 2)$ in the ideal-MHD context and with the Hall term. Fig. 5.5 shows the structure of $b_{\|}$ for this mode in the ideal-MHD context and the Hall-MHD context, with both negative and positive real part of the frequency. The differences in the structure between these three cases are enhanced by the decreased aspect-ratio as the $1/R$ drop-off of the equilibrium magnetic field becomes steeper, meaning the variation of ω_{ci}, and therefore $h = \omega/\omega_{ci}$, increases over the plasma cross-section. It is interesting to note that for the positive frequency Hall-MHD CAE, the frequency is not monotonic as a function of the aspect-ratio. This is because the frequency difference due to the inclusion of the Hall term, which in this case increases the frequency, overtakes the drop in the frequency of the ideal-MHD mode caused by the reduced aspect-ratio.

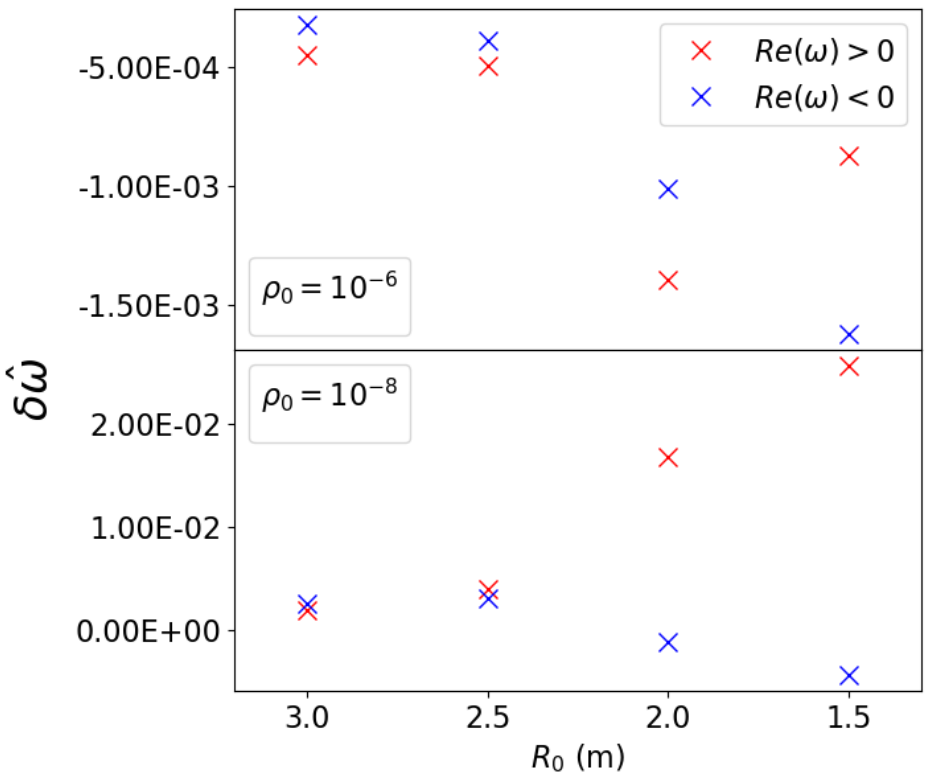

Figure 5.6: The Hall frequency correction, as defined by Eq. (4.42), output from Whales2 is shown for the $(s, m, n) = (2, -2, 2)$ CAE. The equilibrium is the same as in Fig. 5.5 for both cases, except for the magnitude of the density which becomes $\rho_0 = 10^{-6}$ kgm^{-3} in the high density case. The ratio of the CAE frequency to the ion-cyclotron frequency on the magnetic axis is approximately $h_0 \sim 2$ for the low density modes and $h_0 \sim 0.2$ for the high density modes.

We also calculate the Hall correction to the frequency for the same CAE with $(s, m, n) = (2, -2, 2)$. Fig. 5.6 shows the normalised frequency correction, cf. Eq. (4.42), for the positive and negative Hall solutions in two different density regimes. Generally it can be said that the Hall corrections increase in magnitude as the aspect ratio decreases, though the positive frequency solutions in the high density regime are non-monotonic. These results are interesting as, unlike the Hall corrections plotted against differing s or m in Figs. 4.3-4.6, the behaviour of the dispersion relations is strongly affected by the magnitude of the density. For high density modes both positive and negative Hall solutions produce a negative Hall correction - this behaviour was not seen in any of the cylindrical cases. The Hall correction is not large as a fraction of the overall frequency, but as the corrections grow in magnitude with decreasing aspect ratio then the frequency split between the positive and negative modes may be measurable in a tokamak experiment. Further investigation into the magnitude of the Hall correction frequency splitting in realistic tokamak geometries, particularly spherical tokamaks, may yield interesting results.

Chapter 6

Summary

In this thesis we have argued that the study of compressional Alfvén eigenmode spectra and spatial structure is necessary to understand the impact that CAEs have on the transport of energy and particles in fusion devices, and that Hall-MHD theory gives a sufficient description of CAEs to capture the relevant physics to this problem. We then described the design of Whales2, an MHD linear stability solver that can solve for CAEs using the linearised cold ideal Hall-MHD equations cast as wave-equations acting on normal modes of the plasma displacement. We have outlined how the physical coupling of CAEs to the slow-magnetoacoustic and shear Alfvén continua is supressed in Whales2 and shown it to be an effective tool for producing pure CAEs. Unphysical spectral pollution was shown to be mitigated through choice of numerical scheme. We have also demonstrated that Whales2 can be used to solve the linearised ideal-MHD equations and that the approximation to these equations in Whales2 is Hermitian. Whales2 also allows the user freedom to choose the particular finite elements scheme and eigenvalue solver used in each situation.

Chapters 4 & 5 of this thesis were concerned with demonstrating that the output from Whales2 is in agreement with CAE theory, as well as establishing the behaviour of the Hall term in simple MHD configurations. We have shown that Whales2 has good agreement with analytically known results in a homogeneous cylinder for both ideal- and Hall-MHD. Radial mode localisation was also measured in Whales2 and contrasted with the predictions of two models for ideal-MHD. The Mahajan model was shown to be closer to the output of Whales2 for steep density curves, whereas the Coppi model gave better agreement for flatter density profiles. Output from Whales2 applied to toroidal geometries also suggests the existence of inboard poloidally localised modes in the variable $b_{\|}$, which have been predicted in

theory but haven't been widely studied numerically.

We must also analyse the importance of the inclusion of the Hall-MHD terms in Whales2. The results from Whales2 applied to cylindrical geometries indicate that the Hall term can have a significant effect on the radius of localisation when the density profile has a steep gradient, as shown in Fig. 4.11. Fig. 4.13 shows that the Hall terms modify the eigenfunction noticeably in the presence of high pitch of the magnetic field. These results contrast what is shown in Fig. 4.7, for a homogeneous equilibrium, where the eigenfunctions for both the ideal-MHD and Hall-MHD output are not significantly different. From this we infer that the Hall terms have a non-negligible effect on the MHD equations in cylindrical geometries for non-homogeneous profiles. This conclusion is supported by evidence from measuring the difference in eigenfrequency values for ideal-MHD-degenerate modes whose degeneracy has been lifted by inclusion of Hall-MHD effects. The study of variable poloidal magnetic field at the outer wall, Fig. 4.12, shows that the modes are all of frequency ~ 1 MHz, and for the highest poloidal magnetic field the frequency gap between ideal-MHD-degenerate modes is ~ 10 kHz. The numbers are comparable to observed frequencies and splittings in MAST [2]. In toroidal geometries Whales2 shows that the Hall terms do little to modify the poloidal mode coupling present in ideal-MHD, at least for modest values of the shaping parameters ϵ, κ, and τ. The difference in eigenfrequency between ideal-MHD and Hall-MHD modes with the same mode numbers are shown to reach values on the order of 1% of the ideal-MHD frequency, with the splitting increasing as the aspect ratio of the tokamak decreases. Overall, these results suggest that impact of the Hall terms on CAEs in tokamaks is measurable and could be important in understanding such phenomena as the fine frequency splitting of observed CAEs.

6.1 Future Work

Future work with Whales2 has two obvious directions in which to proceed - improvements made to the code itself in order to access new physics, or using the code to further investigate new phenomena with its current capabilities. In terms of improvements to the code, a modest start will allow for a broad range of interesting investigations. In this thesis we made no comparison from Whales2 with experimentally observed CAEs. This was mostly due to time constraints, but it has also been noted that Solovev equilibria can produce poor representations of spherical tokamak equilibria, in which we are most interested [82]. Future work should aim to incorporate equilibria into Whales2 that better represent spherical tokamaks such as the

analytical equilibrium of Weening [82], or through integration of a numerical equilibrium solver such as HELENA [83]. Whales2 can then be used to model the CAE frequency differences measured in tokamak experiments. In particular, results from WHALES have suggested that fine splitting of CAEs may be due to several CAEs present with the same mode numbers [29]. A study to corroborate these results could be instigated using several spherical tokamak equilibria to observe whether the modes are also present in output from Whales2.

Another avenue of further work is the investigation of the CAE interaction with fast-ions through the ion cyclotron resonance. The drawback of Whales2 is that it is a linear code and so cannot self-consistently update after interacting with the fast-ions. However, Whales2 can be used to calculate CAE structures to high resolution and so is suitable for determining where the ion cyclotron resonance occurs for particular fast-ion distributions. This can be done by pushing a distribution of fast-ions in a particular plasma equilibrium with a particular CAE driven at an amplitude that is varied between runs. By comparing the positions for the fast-ion distribution, and the energy distribution of the particles in space, between the different runs points of high wave-particle interaction will be seen as significant deviations.

Bibliography

[1] J. P. Freidberg, *Plasma Physics and Fusion Energy.* Cambridge University Press, 2007.

[2] L. C. Appel, T. Fülöp, M. J. Hole, H. M. Smith, S. D. Pinches, R. G. L. Vann, and The MAST Team, "Compressional Alfvén eigenmodes on MAST," *Plasma Physics and Controlled Fusion*, vol. 50, p. 115011, Oct. 2008.

[3] H. M. Smith and E. Verwichte, "Compressional Alfvén eigenmode structure in spherical tokamaks," *Plasma Physics and Controlled Fusion*, vol. 51, p. 075001, May 2009.

[4] G. McCracken and P. Stott, *Fusion: The Energy of the Universe.* Elsevier, 2012.

[5] F. F. Chen, *Introduction to Plasma Physics and Controlled Fusion.* Springer US, 1984.

[6] R. Conn, J. Holdren, S. Sharafat, D. Steiner, D. Ehst, W. Hogan, R. Krakowski, R. Miller, F. Najmabadi, and K. Schultz, "Economic, safety and environmental prospects of fusion reactors," *Nuclear Fusion*, vol. 30, pp. 1919–1934, Sep. 1990.

[7] J. Ongena and G. V. Oost, "Energy for future centuries - prospects for fusion power as a future energy source," *Fusion Science and Technology*, vol. 53, pp. 3–15, Feb. 2008.

[8] J. D. Lawson, "Some criteria for a power producing thermonuclear reactor," *Proceedings of the Physical Society. Section B*, vol. 70, pp. 6–10, Jan. 1957.

[9] J. Wesson, *Tokamaks.* Oxford University Press, 2011.

[10] J. Phillips, "Magnetic fusion," *Los Alamos Science*, pp. 64–67, 1983.

[11] T. C. Luce, "An analytic functional form for characterization and generation of axisymmetric plasma boundaries," *Plasma Physics and Controlled Fusion*, vol. 55, p. 095009, July 2013.

[12] *Summary of the ITER Final Design Report.* No. 22 in ITER EDA Documentation Series, Vienna: INTERNATIONAL ATOMIC ENERGY AGENCY, 2001.

[13] M. Keilhacker, A. Gibson, C. Gormezano, P. Lomas, P. Thomas, M. Watkins, P. Andrew, B. Balet, D. Borba, C. Challis, I. Coffey, G. Cottrell, H. D. Esch, N. Deliyanakis, A. Fasoli, C. Gowers, H. Guo, G. Huysmans, T. Jones, W. Kerner, R. König, M. Loughlin, A. Maas, F. Marcus, M. Nave, F. Rimini, G. Sadler, S. Sharapov, G. Sips, P. Smeulders, F. Söldner, A. Taroni, B. Tubbing, M. von Hellermann, D. Ward, and JET Team, "High fusion performance from deuterium-tritium plasmas in JET," *Nuclear Fusion*, vol. 39, pp. 209–234, Feb. 1999.

[14] R. Aymar, P. Barabaschi, and Y. Shimomura, "The ITER design," *Plasma Physics and Controlled Fusion*, vol. 44, pp. 519–565, Apr. 2002.

[15] M. Ono and R. Kaita, "Recent progress on spherical torus research," *Physics of Plasmas*, vol. 22, p. 040501, Apr. 2015.

[16] J. A. Bittencourt, *Fundamentals of Plasma Physics.* Springer New York, 2004.

[17] P. L. Pritchett, "Particle-in-cell simulation of plasmas— a tutorial," in *Lecture Notes in Physics*, pp. 1–24, Springer Berlin Heidelberg.

[18] P. J. Catto, "Practical gyrokinetics," *Journal of Plasma Physics*, vol. 85, May 2019.

[19] J. P. Freidberg, *Ideal MHD.* Cambridge University Press, 2014.

[20] N. F. Cramer, *The Physics of Alfvén Waves.* Wiley, 2001.

[21] H. Grad and H. Rubin, "Hydromagnetic equilibria and force-free fields," *Proceedings of the 2nd United Nations International Conference on the Peaceful Uses of Atomic Energy*, vol. 31, pp. 190–197, 1959.

[22] L. S. Solov'ev, "The theory of hydromagnetic stability of toroidal plasma configurations," *J. Exp. Theor. Phys*, vol. 26, pp. 400–407, Feb. 1968.

[23] J. P. Goedbloed, R. Keppens, and S. Poedts, *Advanced Magnetohydrodynamics.* Cambridge University Press, 2009.

[24] A. J. Cerfon and J. P. Freidberg, ""One size fits all" analytic solutions to the Grad–Shafranov equation," *Physics of Plasmas*, vol. 17, p. 032502, Mar. 2010.

[25] J. P. Goedbloed, "Spectrum of ideal magnetohydrodynamics of axisymmetric toroidal systems," *Physics of Fluids*, vol. 18, no. 10, p. 1258, 1975.

[26] J. P. H. Goedbloed and S. Poedts, *Principles of Magnetohydrodynamics*. Cambridge University Press, Aug. 2004.

[27] W. W. Heidbrink, "Basic physics of Alfvén instabilities driven by energetic particles in toroidally confined plasmas," *Physics of Plasmas*, vol. 15, p. 055501, May 2008.

[28] N. Gorelenkov, C. Cheng, E. Fredrickson, E. Belova, D. Gates, S. Kaye, G. Kramer, R. Nazikian, and R. White, "Compressional Alfvén eigenmode instability in NSTX," *Nuclear Fusion*, vol. 42, pp. 977–985, Aug. 2002.

[29] S. E. Sharapov, M. K. Lilley, R. Akers, N. B. Ayed, M. Cecconello, J. W. S. Cook, G. Cunningham, E. Verwichte, and The MAST Team, "Bi-directional Alfvén cyclotron instabilities in the mega-amp spherical tokamak," *Physics of Plasmas*, vol. 21, p. 082501, Aug. 2014.

[30] R. O. Dendy, C. N. Lashmore-Davies, K. G. McClements, and G. A. Cottrell, "The excitation of obliquely propagating fast Alfvén waves at fusion ion cyclotron harmonics," *Physics of Plasmas*, vol. 1, pp. 1918–1928, June 1994.

[31] G. Cottrell, V. Bhatnagar, O. D. Costa, R. Dendy, J. Jacquinot, K. McClements, D. McCune, M. Nave, P. Smeulders, and D. Start, "Ion cyclotron emission measurements during JET deuterium-tritium experiments," *Nuclear Fusion*, vol. 33, pp. 1365–1387, Sept. 1993.

[32] M. Ichimura, H. Higaki, S. Kakimoto, Y. Yamaguchi, K. Nemoto, M. Katano, M. Ishikawa, S. Moriyama, and T. Suzuki, "Observation of spontaneously excited waves in the ion cyclotron frequency range on JT-60u," *Nuclear Fusion*, vol. 48, p. 035012, Feb. 2008.

[33] K. McClements, R. D'Inca, R. Dendy, L. Carbajal, S. Chapman, J. Cook, R. Harvey, W. Heidbrink, and S. Pinches, "Fast particle-driven ion cyclotron emission (ICE) in tokamak plasmas and the case for an ICE diagnostic in ITER," *Nuclear Fusion*, vol. 55, p. 043013, Mar. 2015.

[34] M. J. Hole, L. C. Appel, and R. Martin, "A high resolution mirnov array for the mega ampere spherical tokamak," *Review of Scientific Instruments*, vol. 80, p. 123507, Dec. 2009.

[35] H. Duong, W. Heidbrink, E. Strait, T. Petrie, R. Lee, R. Moyer, and J. Watkins, "Loss of energetic beam ions during TAE instabilities," *Nuclear Fusion*, vol. 33, pp. 749–765, May 1993.

[36] N. J. Fisch, "The alpha channeling effect," No. 1689, p. 020001, EURATOM, 2015.

[37] R. Koch, "Wave–particle interactions in plasmas," *Plasma Physics and Controlled Fusion*, vol. 48, pp. B329–B345, Nov 2006.

[38] T. Stix, *Waves in Plasmas.* American Institute of Physics, 1992.

[39] C. Cheng, "Kinetic extensions of magnetohydrodynamics for axisymmetric toroidal plasmas," *Physics Reports*, vol. 211, pp. 1–51, Feb. 1992.

[40] E. Jaeger, D. Batchelor, and D. Stallings, "Influence of various physics phenomena on fast wave current drive in tokamaks," *Nuclear Fusion*, vol. 33, pp. 179–195, Feb. 1993.

[41] J. C. Wright, *Fast Wave Current Drive Modeling in Tokamaks.* Princeton University, 1998.

[42] J. D. Callen, "Structure of magnetic fields," in *Fundamentals of Plasma Physics*, Jun 2006.

[43] N. N. Gorelenkov, "Energetic particle-driven compressional Alfvén eigenmodes and prospects for ion cyclotron emission studies in fusion plasmas," *New Journal of Physics*, vol. 18, p. 105010, Oct. 2016.

[44] M. Chance, R. Dewar, A. Glasser, J. Greene, R. Grimm, S. Jardin, J. Johnson, B. Rosen, G. Sheffield, and K. Weimer, "Study of magnetohydrodynamic modes in tokamak configurations with noncircular cross-sections," *Plasma Physics and Controlled Nuclear Fusion Research 1974*, vol. 1, p. 463, 1974.

[45] R. B. White, *The Theory of Toroidally Confined Plasmas.* Imperial College Press, Apr. 2006.

[46] J. M. Finn, "Tilt and shift mode stability in spheromaks with line tying," *Physics of Fluids*, vol. 25, no. 1, p. 116, 1982.

[47] A. J. Davies, *The Finite Element Method: A First Approach.* Oxford University Press, 1980.

[48] W. F. Ames, *Numerical Methods for Partial Differential Equations.* Elsevier, 1992.

[49] R. Gruber and J. Rappaz, *Finite Element Methods in Linear Ideal Magnetohydrodynamics.* Springer Berlin Heidelberg, 1985.

[50] X. Llobet, K. Appert, A. Bondeson, and J. Vaclavik, "On spectral pollution," *Computer Physics Communications*, vol. 59, pp. 199–216, June 1990.

[51] S. Ohsaki and S. M. Mahajan, "Hall current and Alfvén wave," *Physics of Plasmas*, vol. 11, pp. 898–902, Mar. 2004.

[52] K. Appert, D. Berger, R. Gruber, and J. Rappaz, "A new finite element approach to the normal mode analysis in magnetohydrodynamics," *Journal of Computational Physics*, vol. 18, pp. 284–299, July 1975.

[53] R. Gruber, "Finite elements in magnetohydrodynamics: Ideal linear stability problem," *Computer Physics Reports*, vol. 6, pp. 299–333, Aug. 1987.

[54] D. Berger, R. Gruber, and F. Troyon, "A finite element approach to the computation of the MHD spectrum of straight noncircular plasma equilibria," *Computer Physics Communications*, vol. 11, no. 3, pp. 313–323, 1976.

[55] R. Gruber, "Finite hybrid elements to compute the ideal magnetohydrodynamic spectrum of an axisymmetric plasma," *Journal of Computational Physics*, vol. 26, pp. 379–389, Mar. 1978.

[56] S. W. Smith, *Digital Signal Processing.* Elsevier, 2003.

[57] M. Frigo and S. Johnson, "The design and implementation of FFTW3," *Proceedings of the IEEE*, vol. 93, pp. 216–231, Feb. 2005.

[58] J. Stoer and R. Bulirsch, *Introduction to Numerical Analysis.* Springer New York, 2002.

[59] M. Abramowitz and I. A. Stegun, *Handbook of Mathematical Functions with Formulas, Graphs, and Mathematical Tables.* New York: Dover, 1964.

[60] K. Petras, "Principles of verified numerical integration," *Journal of Computational and Applied Mathematics*, vol. 199, pp. 317–328, Feb. 2007.

[61] M. Carley, "Numerical quadratures for singular and hypersingular integrals in boundary element methods," *SIAM Journal on Scientific Computing*, vol. 29, pp. 1207–1216, Jan. 2007.

[62] P. Kolm and V. Rokhlin, "Numerical quadratures for singular and hypersingular integrals," *Computers & Mathematics with Applications*, vol. 41, pp. 327–352, Feb. 2001.

[63] V. Hernandez, J. E. Roman, and V. Vidal, "SLEPc: A scalable and flexible toolkit for the solution of eigenvalue problems," *ACM Trans. Math. Software*, vol. 31, no. 3, pp. 351–362, 2005.

[64] J. E. Roman, C. Campos, E. Romero, and A. Tomas, "SLEPc users manual," Tech. Rep. DSIC-II/24/02 - Revision 3.14, D. Sistemes Informàtics i Computació, Universitat Politècnica de València, 2020.

[65] I. B. Bernstein, E. A. Frieman, M. D. Kruskal, and R. M. Kulsrud, "An energy principle for hydromagnetic stability problems," *Proceedings of the Royal Society of London. Series A. Mathematical and Physical Sciences*, vol. 244, pp. 17–40, Feb. 1958.

[66] G. Strang, G. J. Fix, and D. S. Griffin, "An analysis of the finite-element method," *Journal of Applied Mechanics*, vol. 41, pp. 62–62, Mar. 1974.

[67] O. C. Zienkiewicz, R. L. Taylor, and J. Zhu. Elsevier, 2013.

[68] D. Liu and A. Bondeson, "Improved poloidal convergence of the MARS code for MHD stability analysis," *Computer Physics Communications*, vol. 116, pp. 55–64, Jan. 1999.

[69] Y. Q. Liu, A. Bondeson, C. M. Fransson, B. Lennartson, and C. Breitholtz, "Feedback stabilization of nonaxisymmetric resistive wall modes in tokamaks. i. electromagnetic model," *Physics of Plasmas*, vol. 7, pp. 3681–3690, Sept. 2000.

[70] W. Kerner, J. Goedbloed, G. Huysmans, S. Poedts, and E. Schwarz, "CASTOR: Normal-mode analysis of resistive MHD plasmas," *Journal of Computational Physics*, vol. 142, pp. 271–303, May 1998.

[71] D. Borba and W. Kerner, "CASTOR-K: Stability analysis of Alfvén eigenmodes in the presence of energetic ions in tokamaks," *Journal of Computational Physics*, vol. 153, no. 1, pp. 101–138, 1999.

[72] E. Strumberger and S. Günter, "CASTOR3D: linear stability studies for 2D and 3D tokamak equilibria," *Nuclear Fusion*, vol. 57, p. 016032, Nov 2016.

[73] C. Cheng and M. Chance, "NOVA: A nonvariational code for solving the MHD stability of axisymmetric toroidal plasmas," *Journal of Computational Physics*, vol. 71, no. 1, pp. 124–146, 1987.

[74] H. M. Smith and E. D. Fredrickson, "Compressional alfvén eigenmodes in rotating spherical tokamak plasmas," *Plasma Physics and Controlled Fusion*, vol. 59, p. 035007, Feb. 2017.

[75] N. Gorelenkov, E. Fredrickson, W. Heidbrink, N. Crocker, S. Kubota, and W. Peebles, "Discrete compressional Alfvén eigenmode spectrum in tokamaks," *Nuclear Fusion*, vol. 46, pp. S933–S941, Sept. 2006.

[76] B. Coppi, S. Cowley, R. Kulsrud, P. Detragiache, and F. Pegoraro, "High-energy components and collective modes in thermonuclear plasmas," *Physics of Fluids*, vol. 29, no. 12, p. 4060, 1986.

[77] S. M. Mahajan and D. W. Ross, "Spectrum of compressional Alfvén waves," *Physics of Fluids*, vol. 26, no. 9, p. 2561, 1983.

[78] Y. Kolesnichenko, T. Fülöp, M. Lisak, and D. Anderson, "Localized fast magnetoacoustic eigenmodes in tokamak plasmas," *Nuclear Fusion*, vol. 38, pp. 1871–1879, Dec. 1998.

[79] T. Fülöp, M. Lisak, Y. I. Kolesnichenko, and D. Anderson, "The radial and poloidal localization of fast magnetoacoustic eigenmodes in tokamaks," *Physics of Plasmas*, vol. 7, pp. 1479–1486, May 2000.

[80] N. Gorelenkov and C. Cheng, "Alfven cyclotron instability and ion cyclotron emission," *Nuclear Fusion*, vol. 35, pp. 1743–1752, Dec. 1995.

[81] H. Smith, T. Fülöp, M. Lisak, and D. Anderson, "Localization of compressional alfvén eigenmodes in spherical tori," *Physics of Plasmas*, vol. 10, pp. 1437–1442, May 2003.

[82] R. H. Weening, "Analytic spherical torus plasma equilibrium model," *Physics of Plasmas*, vol. 7, pp. 3654–3662, Sept. 2000.

[83] G. Huysmans, J. Goedbloed, and W. Kerner *Proceedings of the CP90 Conference on Computer Physics*, p. 371, 1991.